Automated Prostate Cancer Localisation Using Multiparametric MRI

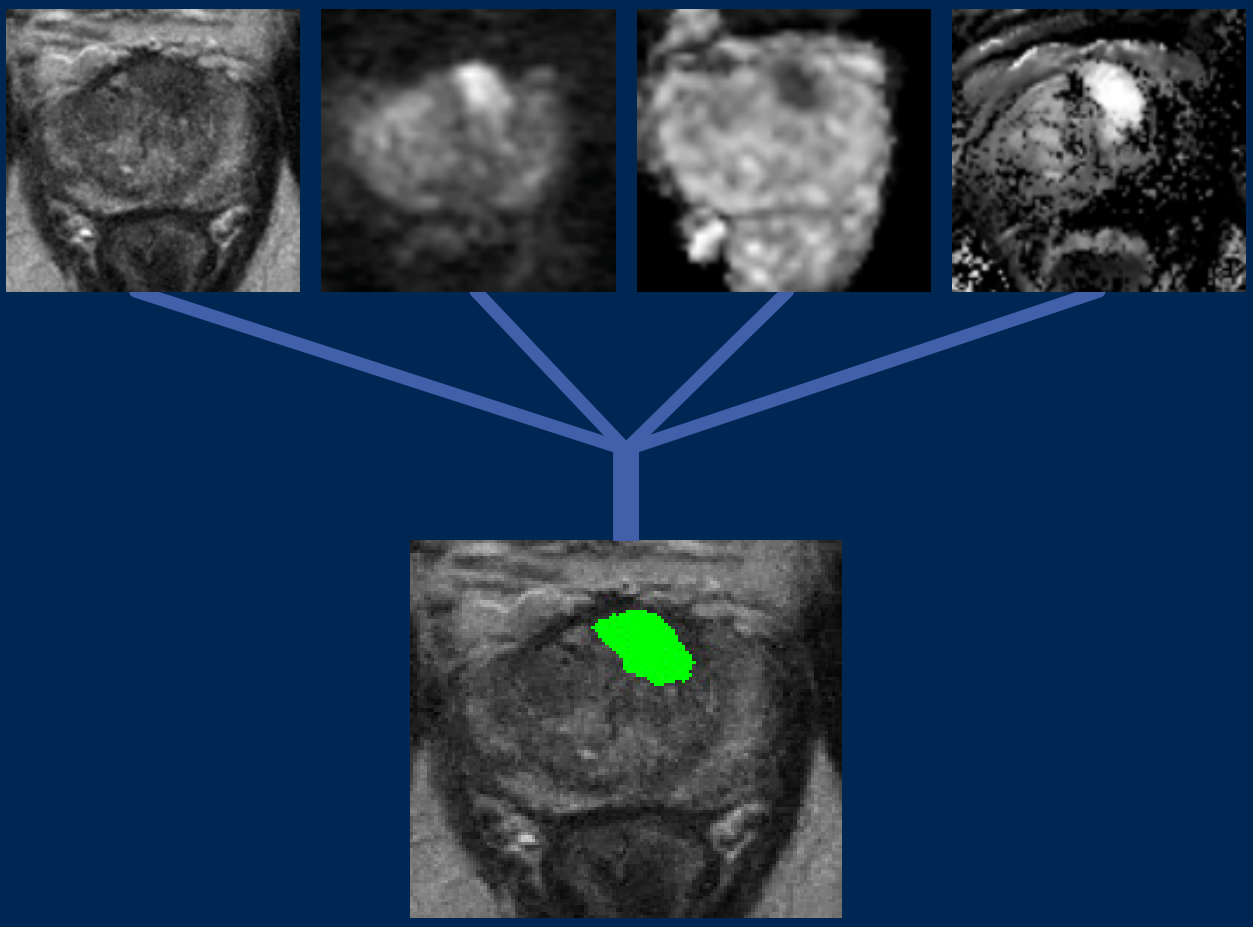

Master's Thesis

Astrid Husballe Munk
Søren Sohrt-Petersen

Group 1070
Spring 2014

Biomedical Engineering and Informatics

AALBORG UNIVERSITY
STUDENT REPORT

AALBORG UNIVERSITY
STUDENT REPORT

Automated Prostate Cancer Localisation Using Multiparametric MRI

Master's Thesis, Biomedical Engineering and Informatics
Group 14gr1070
Contact: {amunk09,ssohrt09}@student.aau.dk

Authors

Astrid Husballe Munk
Stud.cand.polyt.
Aalborg University

Søren Sohrt-Petersen
Stud.cand.polyt.
Aalborg University

Supervisors

Lasse Riis Østergaard
Associate Professor, M.Sc., Ph.D.
Aalborg University

Anne Sofie Korsager
Research Assistant, M.Sc.
Aalborg University

Page Numbers: 112 pages

Department of Health Science and Technology
Aalborg University
Fredrik Bajers Vej 7D2
DK-9220 Aalborg
Denmark

June 3, 2014

Dansk Resumé

Prostatakræft, der er kræft i blærehalskirtlen, er den hyppigste kræftform blandt mænd. I dag diagnosticeres prostatakræft på baggrund af mistanke for kræft fra resultater fra blodprøve og rektal eksploration. Før en endelig diagnose kan stilles, skal mistanken bekræftes ved fund af ondartede celler i vævsprøver. Disse tages fra områder i prostata via endetarmen, enten på vilkårlig vis eller med visuel vejledning fra transrektale ultralydsbilleder. Det er dog uhensigtsmæssigt, at nålen, som vævsprøverne tages med, nemt kan undlade at ramme en kræftknude, og ligeledes uhensigtsmæssigt, at kræftknuder kan være svære at identificere på ultralydsbilleder. Dette foranlediger et højt antal af falske negative diagnoser, hvilket betyder, at mange kræftsyge mænd forbliver udiagnosticerede. Et noninvasivt diagnosticeringsgrundlag med større detektionsrate og færre falske negative er derfor ønskeligt.

Magnetic resonance imaging (MRI) har vist lovende egenskaber i diskrimination af sygt prostatavæv fra raskt prostatavæv, og flere studier foreslår brug af multiparametrisk MRI data som basis for diskriminationen for at inkludere mest mulig viden om forskellige væv. Multiparametrisk MRI data består af både anatomiske og fysiologiske MR billeder, der hver især afbilleder og fremhæver forskellige egenskaber ved samme væv. Disse billeder fortolkes ofte kvalitativt ved manuel visuel identification af anormale egenskaber, eksempelvis forskelle i billedintensiteter eller strukturelle irregulariteter. Det kan dog være en stor arbejdsbyrde at skulle fortolke så store datasæt, og derfor er udvikling af kvantitative og reproducerbare metoder til analyse af multiparametrisk MRI data meget attraktiv.

Dette projekt opstiller en procedure for automatiseret lokalisering af prostatakræft på basis af multiparametrisk MRI data bestående af T2-vægtede, diffusions-vægtede og T1-vægtede dynamisk kontrast-forstærkede billeder.

Den opstillede procedure for automatiseret lokalisering af prostatakræft består af tre processeringstrin: Som det første segmenteres prostata i billederne. Dernæst klassificeres hver prostatavoxel til at være enten en kræftkandidat voxel eller en voxel, der repræsenterer normalt prostatavæv. Denne voxelklassificering baseres på den enkelte voxels fremtoning med hensyn til billedintensitet og tekstur i de multiparametriske MRI data. I det tredje processeringstrin inddeles alle kræftkandidat voxels i regioner ved hjælp af enten LoG kantdetektion eller watershed transformation, og hver region klassificeres efterfølgende til at være enten en kræftregion eller en region bestående af normalt prostatavæv. Et billedområde, som identificeres som kræftregion i flere forskellige MR billedtyper, betragtes som en lokaliseret kræftknude.

Gennem validering mod reference data fastslået ud fra ekspert påvisninger af sande kræftknudelokationer vurderes det at den indledende voxelklassifikation virker som tilsigtet. Antallet af mulige kræftvoxels indsnævres uden at sande kræftvoxels udelades. Valideringen viser ydermere, at den bedste kræftknudelokalisering opnås ved at bruge dels LoG kantdetektion til inddeling af kræftkandidat voxels fra voxelklassifikationen i regioner, og dels ved at basere den opstillede procedure på sammenstilling af resultater fra flere af de forskellige slags MR billeder til rådighed.

Den opstillede procedure for automatiseret lokalisering af prostatakræft baseret på multiparametrisk MRI er et lovende værktøj for hele processen for håndtering af prostatakræft. Den kan hjælpe til tidlig og præcis diagnosticering ved at målrette biopsiproceduren, på sigt kan den potentielt fungere som et screeningsværktøj, og endeligt kan den hjælpe i planlægning og opfølgning af strålebehandling.

Summary

Prostate cancer is the second most frequently diagnosed cancer worldwide. Suspicion of prostate cancer is usually based on results from a prostate-specific antigen blood test and a digital rectal examination. However, a definite prostate cancer diagnosis can only be stated from cancer positive results from needle biopsy. This diagnostic procedure carries a risk of serious complications for the patient and has been proved to have poor sensitivity, i.e. the needle may easily miss a tumour. At present, visual guidance using transrectal ultrasound most often aids in targeting the needle positions, however, still many prostate cancer cases remain undiagnosed after the first biopsy.

Magnetic resonance imaging (MRI) has shown promising results in the differentiation of healthy and cancerous prostate tissue. To integrate as much information as possible, more studies support the use of multiparametric MRI, i.e. a set comprising both anatomical and physiological MR images of the same prostate tissue but corresponding to different acquisition conditions, thereby reflecting different tissue properties. However, the interpretation of these images is typically performed in a qualitative manner by manual visual detection and classification of abnormal features such as intensity differences and structural irregularities. A more quantitative and reproducible approach for analysis of the multiparametric MRI is desired.

This project proposes a framework for automated localisation of prostate cancer using multiparametric MRI data comprised of images from T2-weighted, diffusion-weighted, and T1-weighted dynamic contrast-enhanced MRI.

The proposed framework consists of three processing steps: In a first step, the prostate is segmented. Each voxel within the prostate is then in a second step classified either as a cancer candidate voxel or a voxel representing normal tissue, based on a set of voxel features of intensity and texture extracted from the set of multiparametric MRI data. In a third step, the set of found cancer candidate voxels is segmented into regions by means of one of two segmentation methods, LoG edge detection and watershed transform. Based on a subsequently extracted region feature, each region is classified as a cancer region or a region most probably representing normal prostate tissue. A cancer region identified at equivalent image location within more types of MR images is considered a localised tumour.

Validation of the tumour localisation results against ground truth established by statements from an expert of true tumour locations shows promising results. The best localisation performance in terms of correct localisation of true tumours with minimum of falsely localised tumours was achieved applying LoG edge detection for the region segmentation in the step of identification of cancer regions, with 9 of 11 true tumours correctly localised and a mean number of 2.67 false positive tumours. On the other hand, use of watershed transform for the region segmentation in the step of identification of cancer regions produced correct localisation for 8 of 11 true tumours and a mean number of only 1.33 falsely localised tumours.

The proposed framework for automated prostate cancer localisation using multiparametric MRI is a promising tool in the management of prostate cancer. As a diagnostic tool it could readily aid in targeting biopsy procedures. In the long term, after a few refinements and more research, automated prostate cancer localisation using multiparametric MRI may, on its own, serve as a screening tool and totally replace the need for biopsy.

Contents

List of Tables

List of Figures

Preface

This report describes the work of a framework for automated prostate cancer localisation using multiparametric magnetic resonance imaging (MRI). The motivation for this project is briefly outlined in Chapter 1, while theoretical background information on prostate cancer and MRI is given in Chapters 2 and 3. The project aim is presented in Chapter 4, before the proposed framework for automated prostate cancer localisation using multiparametric MRI is presented and elaborated in Chapters 5-9. The validation of the proposed framework, including test protocol and results are presented in Chapters 10-11. Finally, the validation results are discussed and suggestions for improvement and future work are presented in Chapter 12.

References are listed with the *IEEE*-style, e.g. [1] refers to the first reference in the bibliography provided in the end of the report. Figures, tables, and formulas have been numbered according to the chapter in which they are presented, e.g. first figure in chapter 1 is Figure 1.1.

Acknowledgements

We are particularly grateful for the technical assistance and supervision given by Jesper Carl Hansen, Head of Medical Physics, M.Sc., Ph.D., Aalborg University Hospital, during the duration of the project. We would also like to thank Lars Boesen, physician at Department of Urology, Herlev Hospital, for provision of data.

Aalborg University, June 3, 2014

Astrid Munk
Stud.cand.polyt.
amunk09@student.aau.dk

Søren Sohrt-Petersen
Stud.cand.polyt.
ssohrt09@student.aau.dk

Chapter 1

Introduction

Cancer is a disease which untreated leads to death while when treated, some patients have the possibility of surviving their cancer disease. The chance of survival increases, if the cancer is diagnosed at an early stage as the treatment is often simpler and more likely to be effective [1]. At a later stage, the cancer is more complex and has possibly spread to multiple organs. So detecting the cancer at an early stage increases the chances for successful treatment and thus the chance of survival. However, one third of all cancer patients experience inferring quality deviations in the diagnostic phase, general practitioners report in a Danish cohort study involving 6.000 cancer patients and 1.446 general practitioners [2]. Among all quality deviations, 49.2% were related to the clinical investigations and decisions. The most frequent reported quality deviation was that of "*retrospectively, one or more of my clinical decisions were less optimal*" (23.5%). False negative clinical examinations and laboratory tests counted for 12.9% and 12.8% of all quality deviations, respectively. Quality deviations in the diagnosis of cancer cause unnecessary delays (average +41 days) in the detection of the cancer, which may worsen the prognosis and require more intensive treatment.

Regarding prostate cancer, 26% of all cases were associated with some type of quality deviation in the diagnostic phase [2]. Transrectal ultrasound (TRUS)-guided systemic biopsy using 6-12 cores is the recommended diagnostic approach in most cases with suspicion of prostate cancer [3, 4]. However, low cancer detection rates of TRUS-guided biopsy have been found in more studies, and a British newspaper reports that biopsies miss one in two tumours [5]. Consequently, patients are subjected to repeat biopsies and ultimately, a saturated biopsy (>20 cores) as the last resort. It has been estimated that in order to prevent one death from prostate cancer, 1410 men need to be screened and 48 cases of prostate cancer need to be treated [6]. Coupled with the fact that the biopsy procedure poses a risk of numerous unfortunate side effects for the patient, a diagnostic tool with increased cancer detection rate is of utmost importance.

Magnetic resonance imaging (MRI) of the prostate can aid in many aspects of the prostate cancer management, from initial detection to treatment planning, and follow-up [7, 8, 9, 10]. Prior to biopsy, MRI can aid in the decision whether or not to perform a biopsy, and where and how the biopsy should be performed. From MRI the aggressiveness of the tumour can be determined as well, providing decisive information in the treatment planning. The aggressiveness of prostate cancer is a significant prognostic factor, and the real challenge in prostate cancer management is to detect and stage the cancer into being either aggressive and refer the patient to treatment, or into being indolent and refer the patient to active surveillance, which basically is a continuous monitoring and staging of the cancer. An accurate staging of the cancer can prevent the patient from unnecessary treatment and potentially deliberating unwanted side effects. Traditional treatment of prostate cancer treats the prostate as a whole, regardless of the size of the tumour in the gland. For effective treatment damage to healthy tissue is almost inevitable causing side effects such as impotence and incontinence amongst others.

Given these points, MRI provides the ability to closely monitor the activity of the tumour and thus produces useful information in diagnosis, treatment planning, and monitoring treatment response of prostate cancer. At present, MRI is either based on manual readings of the MR images or simply not a part of the clinical routine of prostate cancer management [11]. The visual localisation of prostate cancer is challenged, as cancerous tissue manifests in an intensity range similar to that of normal tissue in some parts of the prostate. Beside being time consuming, visual detection of prostate cancer also suffers from inter- and intraobserver variability.

This project investigates the possibility of computer aided detection of prostate cancer based on MRI. Automating the detection and localisation of prostate cancer will increase the objectivity and reliability and possibly enable an early diagnosis. In order to develop computer aided detection of prostate cancer based on MRI, basic knowledge of the prostate, prostate cancer, and MRI are fundamentals. These topics are unfolded to more detail in the following chapters.

Chapter 2

Prostate and Prostate Cancer

Prostate cancer is the most frequently diagnosed non-cutaneous neoplasm among men in developed countries [12]. Due to the high heterogeneity of different prostate cancers, it is hard to standardise and generalise its diagnosis and choice of treatment once a diagnosis is made [13]. This chapter presents a brief description of the prostate in Section 2.1, and describes prostate cancer in Section 2.2, including the detection and diagnosis of prostate cancer in Section 2.3.

2.1 The Prostate

The prostate is an exocrine gland, located at the base of the bladder, in front of the rectum, surrounding the beginning of the urethra, as seen in Figure 2.1. In younger men, the prostate is the size of a walnut, but it enlarges slowly with advancing age. More thoroughly, the prostate is formed as a tetrahedron with rounded corners forming apex and basis prostatae. Apex prostatae is turned downwards, rests on the urogenital diaphragm, and lies 1.5-2 cm from the lower edge of the symphysis. Basis prostatae is turned slightly upwards and lies contiguously against cervix vesicae. The prostate is attached to the symphysis by lig. puboprostaticum. The backside of the prostate is turned downwards and backwards, and downwards it connects to the rectum, only separated by septum rectovesicale or Denonvilliers fascie.

The prostate is surrounded by fat, connective tissue, and plexus prostaticus, which is a collection of nerves [14]. The prostate composes a part of the male reproductive system and consists of 40-50 glands, which surround and restrain the urethra. The glands are divided in an inner periurethral group and an outer periurethral group, which are separated by fibrous connective tissue. The prostate glands produce seminal fluid which protects and enriches the sperm. The seminal fluid is kept liquid by the function of the glycoprotein prostate-specific antigen (PSA) produced by the epithelial cells in the prostate. In the event of prostate cancer, prostate hypertrophy, or bacterial prostatitis, the PSA leaks into the bloodstream.

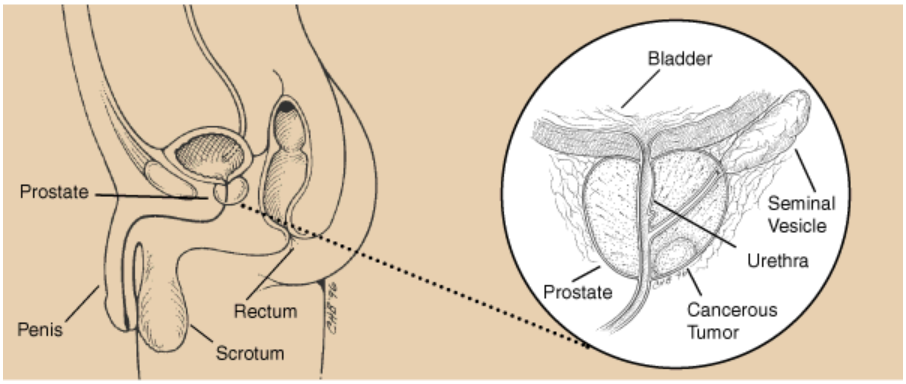

Figure 2.1: Sagittal view of the male reproductive system with the prostate located at the base of the bladder. Illustration from [15].

Anatomically, the prostate is described by three prostate zones, each of which originates from the urethra and has specific architectural features [16]. These anatomical zones are labelled the peripheral zone (PZ), the central zone (CZ), and the transitional zone (TZ) as seen in Figure 2.2. In some matters, the TZ and CZ are jointly termed the central gland.

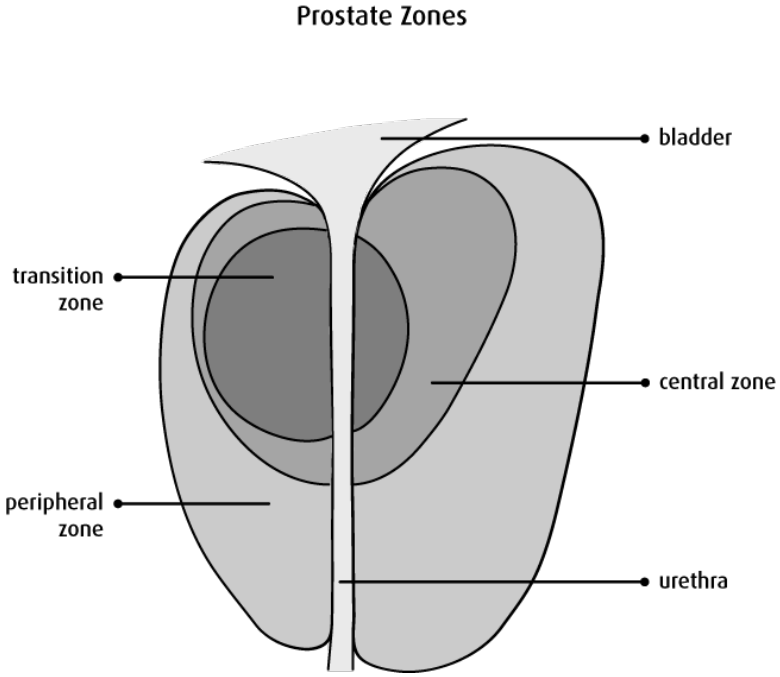

Figure 2.2: Coronal view of the prostate divided into three prostate zones. Illustration from [17].

PZ is the zone closest to the rectum, it is mainly glandular tissue and consists of 70% of the prostate gland [18, 16, 19]. TZ is the midmost part of the prostate and is mainly fascicles of smooth muscle. It surrounds the urethra, and for younger men, TZ composes 5-10% of the prostate gland. However, as men age, the TZ enlarges and slowly becomes the largest zone of the prostate. This is termed benign prostatic hyperplasia (BPH). Finally, CZ is wedge-shaped and located in front of the TZ and thus is the zone of prostate farthest from the rectum. CZ consists of up to 25% of the prostate gland and its tissues are mainly dense stroma and complex glands. While the PZ is the most common site of inflammation and cancer, the CZ is almost resistant to diseases, and the TZ is mainly involved in BPH.

2.2 Prostate Cancer

According to the Association of the Nordic Cancer Registries (NORDCAN), the incidence of prostate cancer in Denmark was 4.362 in 2011 (23.9% of all cancer cases), and it has been estimated that 1.152 men (14.6% of all cancer deaths) died from prostate cancer the same year [12]. The prevalence of prostate cancer in 2011 has been estimated to a total of 26.617 in Denmark. The incidence rate has been increasing during the last decades, and this increase has been associated with the similarly increasing frequency of testing for prostate cancer [20]. As seen in Figure 2.3, the number of prostate cancer victims has, however, been reasonably stable during the last decades, thus causing an increase in the prevalence.

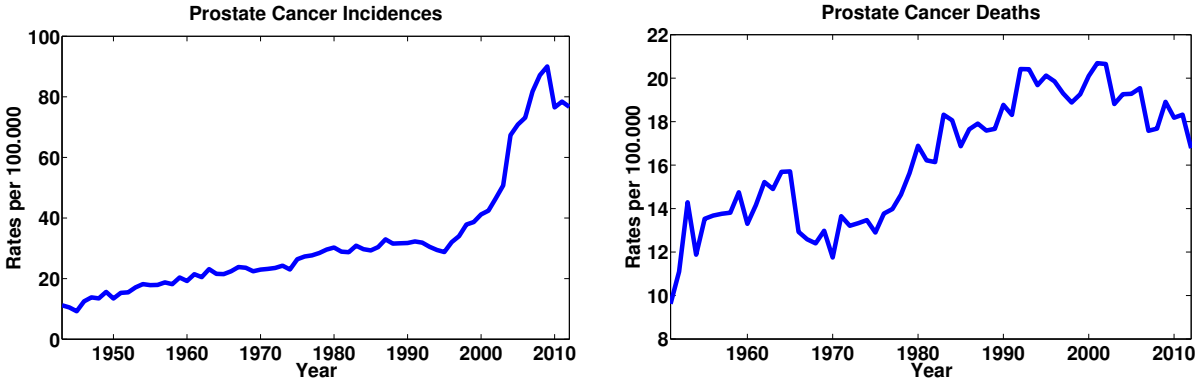

Figure 2.3: Left: Numbers per year per 100.000 persons, age-standardised rate of incidences of prostate cancer. **Right:** Numbers per year per 100.000 persons, age-standardised rate of prostate cancer deaths. Numbers from [12].

Old age, inheritance, and diet are all risk factors of prostate cancer. Among these, old age is the most notable risk factor, which is seen in Figure 2.4. The graph to the left shows the proportion of age and new cancer cases. It is seen that the majority of the incidences occur in men age 60 and older. The graph to the right shows that mainly men at old age die from prostate cancer.

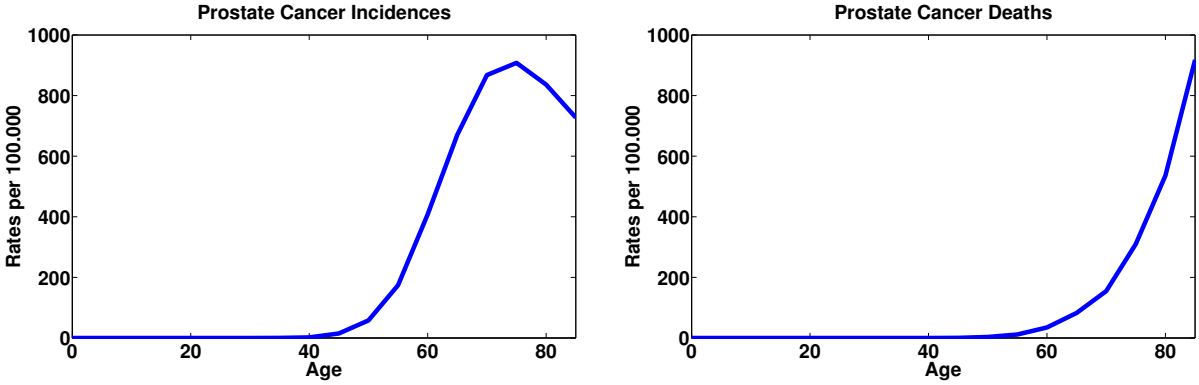

Figure 2.4: Left: Numbers per year per 100.000 persons of a certain age, incidences of prostate cancer. **Right:** Numbers per year per 100.000 persons of a certain age, prostate cancer deaths. Numbers from [12].

In addition to old age, men with a family history of prostate cancer are at a higher risk of developing prostate cancer. A Scandinavian study [21] has proven statistically significant effects of heritable factors for prostate cancer, and in other words, men whose brother or father and also uncle or grandfather diagnosed with prostate cancer, have eight times the risk of getting prostate cancer. Finally, diet may cause a risk, as prostate cancer is more endemic in western countries where meat and high-fat dairy are common. Such diet boosts the male hormone levels, causing cancerous prostate cells to grow faster and more aggressively.

The manifestation of prostate cancer is highly heterogeneous when it comes to aggressiveness, as it ranges from indolent to highly aggressive. An old man may be diagnosed with prostate cancer, and it could be unlikely that the disease would affect his quality or length of life. On the other hand, a younger man may be presented with an aggressive cancer, severely advanced, and die within a few years. An early diagnosis of aggressive cancers may cause a reduction in the prostate cancer-specific deaths [22]. Being able to distinguish between indolent and aggressive cancer remains a high priority for continued research.

Tumour aggressiveness is an important predictor of patient outcome and prognosis. In the early stages of the disease, men may have no symptoms. However, as the disease progresses, the symptoms of prostate cancer can be difficulty in initiating and/or stopping urination, weak urine stream, frequent urination, and pain on urination or ejaculation. Advanced cancer may cause deep pain in the hips, upper thighs, or lower back as an indication of the cancer has metastasised to the bones.

2.3 Detection and Diagnosis of Prostate Cancer

In Denmark the Danish Health and Medicines Authority has recommended guidelines in the detection and treatment of prostate cancer [20]. Suspicion of prostate cancer is based on perineal pains and oedema in the lymphs corresponding to the genitials and lower extremities. This suspicion is investigated by means of two tests, a digital rectal examination (DRE) and a PSA test.

2.3.1 Detection of Prostate Cancer

During the DRE, the physician checks whether the prostate is unusually hard, irregular, or asymmetric, which all are symptoms of prostate cancer. The frequency of prostate cancer across the anatomical zones of the prostate is not evenly spread. Around 70% of the cancer originates in the PZ, around 25% in the TZ, and only 5% in the CZ [18, 19]. In spite of the DRE being the first step in the diagnosis of prostate cancer, the physician will only be able to evaluate prostate cancers in the PZ due to the anatomy of the abdomen. The PSA test is a simple blood test, and the results are usually reported as nanograms of PSA per milliliter (ng/mL) of blood.

2.3.2 Diagnosis of Prostate Cancer

If the DRE reveals any abnormality and/or if the PSA test indicates a risk of prostate cancer, a core biopsy of the prostate is done in order to diagnose for prostate cancer. Important to realise is that neither the results from the DRE or PSA test can diagnose prostate cancer. It is only on the basis of a tissue sample positive for cancer cells that prostate cancer can be definitely diagnosed.

In order to determine the direction of treatment and the prognosis of the prostate cancer, two measures need to be evaluated:

- Microscopic examination of the tissue sample.
- Clinical staging of the index tumour and its potential metastases.

The tissue sample from the biopsy is used in a microscopic examination to assign a grading score. The most widespread method for histological grading of prostate is the Gleason grading system [23]. The Gleason histological grading diagram is shown in Figure 2.5. It shows five basic tissue patterns associated with five grades, and as such the Gleason grades are based on the disparity between the healthy and malignant cells. In Gleason grades 1 and 2 the cancer cells closely resemble normal prostate cells, whereas the cancer cells in the higher grades differ severely from normal prostate cells. The greater the disparity, the higher the Gleason grade, and the more likely the tumour is aggressive and will metastasize.

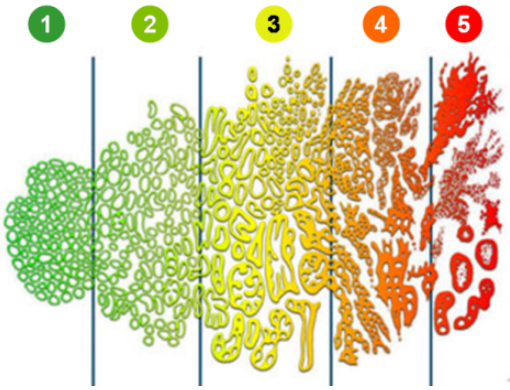

Figure 2.5: Gleason Histological Grading Diagram. Grade 1 appears on the far left and is used to stage cancer cells resembling normal prostate cells. Grade 5 on the far right is used to stage cancers having a poor prognosis. The disparity between the healthy and malignant cells reflects the aggressiveness of the tumour. Illustration from [23].

A pathologist microscopically examines the biopsy samples and assigns a Gleason grade to the observed patterns of the sample's histology. If the sample suggests a tumour, two grades are assigned to the tumour. First a primary grade describing the dominant pattern of the tumour is assigned to the tumour, and next a secondary grade describing the next most-frequent pattern is as well assigned to the tumour. The two Gleason grades are summed to a Gleason score.

The clinical stage of the prostate is denoted by T1-T4 and is determined based on whether the tumour(s) have spread outside the prostate or not [24]. Clinical T1 and T2 cancers are located only within the prostate, while the stages T3 and T4 have spread outside the prostate. To

further classify the clinical stage, each T classification is divided into three subcategories; a, b and c, depending on tumour size and localisation.

Finally, having the Gleason score and clinical staging at hand, the aggressiveness of the prostate cancer can further be stratified into three groups, in order to specify the treatment. This grouping is based on results from the DRE, PSA test, Gleason score, and clinical stage [25]:

Low Risk: PSA $<$ 10 ng/mL and Gleason score $\leq$ 6 and clinical stage T1-T2a
Intermediate Risk: PSA = 10-20 ng/mL or Gleason score 7 or clinical stage T2b or T2c
High Risk: PSA $>$ 20 ng/mL or Gleason score 8-10 or clinical stage $>$ T2c

Indolent or **low risk** prostate cancers may not require treatment such as radical prostatectomy or radiation therapy, in order not to put patients at risk of otherwise unnecessary side effects. Instead active surveillance or waitful watching are used with the purpose to monitor the prostate cancer for progressive signs. Components of active surveillance are PSA testing, DRE, and repeat biopsies administered periodically. On the other hand, the treatment of **intermediate** and **high risk** prostate cancers often involve either radical prostatectomy or radiation therapy.

The following sections provides a description of the PSA test and the prostate biopsy, and the side effects involved in these diagnostic techniques.

Prostate Specific Antigen-test

As stated in Section 2.1, the prostate produces PSA, the level of which in the blood is correlated with a higher risk of prostate cancer. Thus measuring the level of PSA or dynamic changes in the PSA level in the blood has served as a widely used screening technique for prostate cancer. However, as an increased PSA blood level can be caused by numerous factors besides cancer, an increase in the PSA blood level can only serve as a marker of possible prostate cancer and not as a marker of definite prostate cancer. The PSA test is reported to have a low specificity (36%), meaning that approximately only one out of three men with increased PSA level actually has cancer in the prostate, and conversely, the PSA test can happen to falsely exclude a presence of cancer [25]. The benefits of PSA testing are few, and especially compared to the potential substantial psychological harms it may cause. In Denmark no general screening strategy using the PSA test is recommended, only men with family prostate cancer aged 50 are recommended a PSA test on a yearly basis. The problem lies in the difficulty in the distinction between the many indolent cases of prostate cancer which do not necessarily need treatment and the few aggressive cases of prostate cancer, in which the patient could benefit from treatment. To illustrate this complication, it has been estimated that for each man, who benefits from treatment, 49 men are unnecessarily being treated. Based on the risk of numerous side effects of the treatment such as erectile dysfunctions or trouble in urination, and furthermore the decreased quality of life that often follows a course of treatment with numerous check-ups and hospital visits, regular screening for prostate cancer is not offered in Denmark.

Before conducting a PSA test, the pros and cons of using the test is discussed thoroughly with the patient. The advantage of testing is that the test can bring reassurance if normal, or the patient could be the one benefiting from treatment. On the other hand, the test could turn out as false positive, and the patient would be one of the 49 not benefiting from treatment, and in addition be one out of two who experience substantial side effects. So, PSA testing can be helpful, but it is crucial that no prostate cancer diagnosis is based solely upon an increased

level of PSA in the blood.

If both the DRE and PSA test produce results suspicious of cancer, a definitive diagnosis is based on histological tissue analysis obtained by means of needle biopsy. By viewing the microscopic images of biopsy specimens, a pathologist can determine the histological Gleason grades. Even though the prostate tissue samples are collected in a random manner, most often it is guided by transrectal ultrasound (TRUS).

Transrectal Ultrasound-guided Prostate Biopsy

The standard method for detection and localisation of prostate cancer is pathological analysis of tissue samples acquired through TRUS-guided prostate biopsy. An ultrasound probe is inserted rectally together with a biopsy needle and is used in guidance to ensure that biopsies are taken from predetermined sites in the outer gland. The standard practice for prostate biopsy has been the sextant biopsy scheme, where cores are taken parasagittally in a lateral direction from six regions of the prostate, in order to get most samples from the PZ. One of the major shortcomings is that the cancer cells easily can be missed, since only a limited amount of tissue is sampled during the biopsy. To overcome this, several studies suggest using biopsy scheme with 10 or more cores, improving higher detection rate than the traditional sextant scheme [4, 26, 27]. Such a scheme is illustrated in Figure 2.6. However, a false negative rate of more than 30% have been reported using a 12 core biopsy [27].

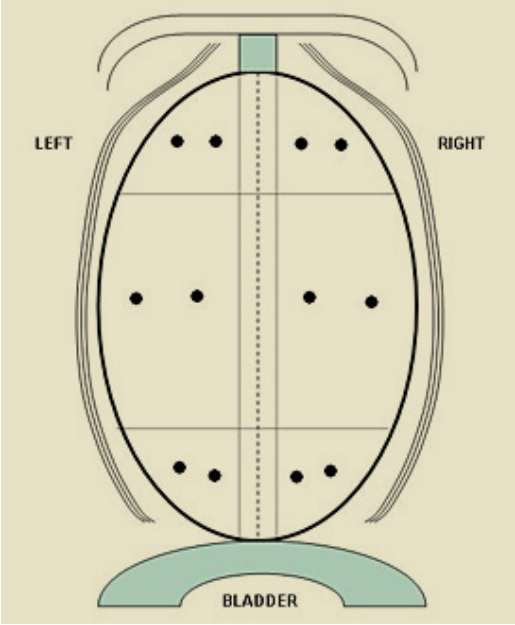

Figure 2.6: A standard 12 core biopsy scheme. A total of 12 cores are taken, 6 from each side of the prostate. Normally each tissue core measures 1mm x 10mm in size. Illustration from [28].

Since a biopsy is an invasive procedure, there is a risk for complications, ranging from minor complications, such as hematuria and hemospermia, to major complications, such as acute urinary retention, infections, bleeding, and fever [29, 30, 31]. A study by Nam et al. [29] has shown that in a period of 10 years, the hospital admission for patients undergoing a biopsy and subsequently not diagnosed with prostate cancer increased from 1 - 4.1%. Among all com-

plications related to the biopsy, the majority of the admissions were due to infection (71.6%). In addition, the study found that the hospital admission rate was higher for patients not diagnosed with cancer compared to the patients actually diagnosed with cancer. The tendency of infections was also found in a study by Özden et al. [30], in which 2.1% of the patients undergoing biopsy were diagnosed with acute bacterial prostatitis, when looking at both first and repeat biopsies. They also found that the risk of acute prostatitis increased for repeat biopsies. If the PSA blood level of a patient increases continually, despite negative results from both the first and second biopsy procedures, a prostate saturation biopsy is performed. The patient then gets general anesthesia and 40-80 core samples are taken from the prostate [32].

Despite the risk of complications, biopsy guided by TRUS has its advantages as it makes it possible to distinguish the PZ from the rest of the prostate during the procedure. Due to the homogeneous texture of the PZ tissue compared to the otherwise heterogeneous texture of the prostate, the PZ is more echogenic and will appear as a bright region in ultrasound images. This difference in intensities provides a good guidance with regard to the gland size and its boundaries, however, only little information on the internal glandular tissue, and no detail on focal lesions [33]. Thus, cancers are visible in the PZ, as they are hypoechoic and then appear as dark lesions in the otherwise bright PZ. For this reason, the target for TRUS-guided biopsies are dark lesions in the PZ. An example of this is shown in Figure 2.7, where the boundary of the prostate is visible and relatively distinguishable. Nonetheless, benign lesions such as prostatitis will also cause hypoechoic lesions in ultrasound [7, 34]. Thus, an insignificant low contrast between healthy tissue and tumour tissue is produced using ultrasound [35, 36]. This fact, as well as the inability to detect TZ in TRUS-guidance, limits the specificity of the procedure. On the other hand, the sensitivity is limited by the high number of benign hypoechoic lesions [37]. Studies have found a prostate cancer detection rate of 11-35% in TRUS images [33]. Due to the limited delineation of malign tissue in ultrasound images, systematic repeat biopsy is preferred compared to techniques concentrating on ultrasound findings [34].

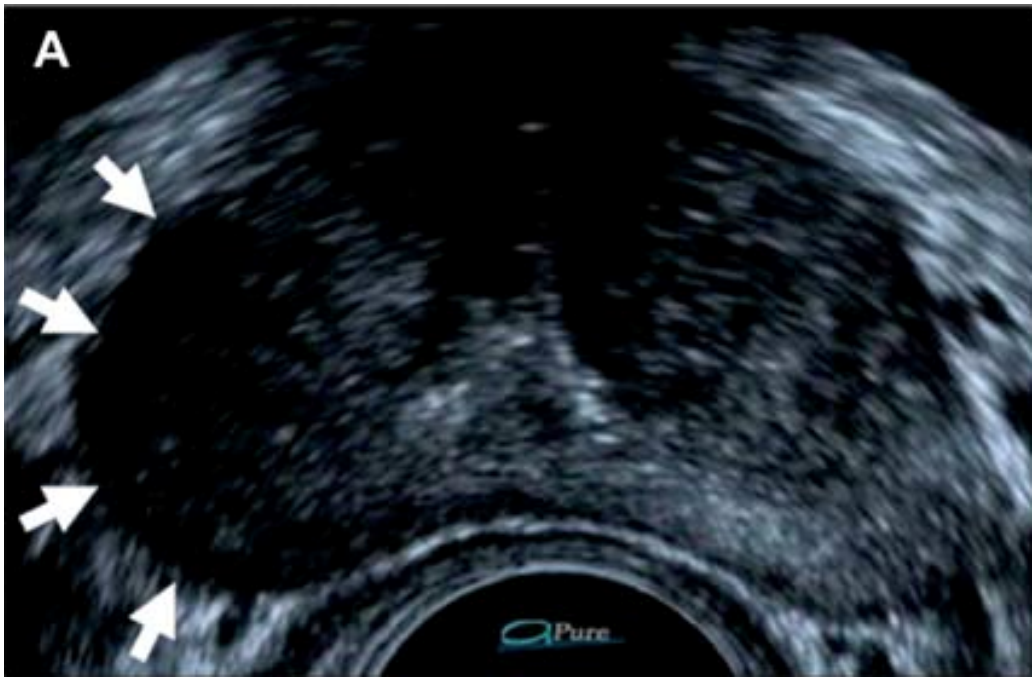

Figure 2.7: TRUS image of the prostate of a patient aged 65. The arrows point out a hypoechoic lesion in the PZ, a region suspicious for cancer. Image from [7].

2.3.3 Potentials of Magnetic Resonance in Prostate Cancer Diagnosis

To decrease the rate of false negatives of prostate biopsies, and thereby increase the detection rate and the specificity, the use of MRI has proved feasible. More studies have investigated the use of MRI in the detection of prostate cancer with promising results [38].

One application of MRI in the diagnosis of prostate cancer is improvement of the biopsy procedure, which has led to an increased interest in the fusion of MRI and TRUS for improved guidance of targeted prostate biopsy. In a study by Sonn et al. [39], information from prostate MRI was included in the biopsy procedure, and this combined approach of MRI-guided biopsies produced a cancer diagnosis rate of 37% among men who otherwise had a history of only negative biopsy results. In the literature mainly ywo methods of fusing MRI and TRUS can be found; cognitive fusion [40] and co-registration [36, 37]. In cognitive fusion, MRI is conducted prior to biopsy to detect lesions in the MR images. Afterwards TRUS is used during the biopsy to guide the needle towards the regions of the prostate, which demonstrated suspicious lesions in the MR images. The use of cognitive fusion has proved significantly improved detection rates compared to the traditional solely TRUS-guided biopsy [40]. On the other hand, in co-registration the MR images are merged with real-time TRUS images. This is possible as the ultrasound probe is being tracked during the biopsy, enabling visualisation of the lesions from MR on the ultrasound images. The co-registration of the MR images to the real-time TRUS has also proved improved detection rates.

Another application of MRI in the diagnosis of prostate cancer is as a screening tool. Because MRI have a relatively high specificity in comparison with the PSA test, this could prevent unnecessary biopsy procedures, as only subjects with abnormal MR images would undergo a biopsy procedure [6, 8]. The screening would then be a completely noninvasive procedure, however at present, no standardised MR image-based screening protocol for early detection of prostate cancer exists.

The use of MRI as an accurate technique to detect and localise prostate cancer and detect significant tumours is gaining a widespread acceptance [37]. Localisation of prostate cancer using MRI has been shown to be significantly more accurate than DRE and systematic random biopsies [8]. In the following chapters, it will be described how MRI can be used to detect and localise prostate cancer.

Chapter 3

Magnetic Resonance Imaging of the Prostate and Prostate Cancer

This chapter describes the acquisition techniques of different magnetic resonance (MR) images in Section 3.1, introduces the concept of multiparametric MRI in Section 3.2, and finally presents the clinical application of MRI to prostate cancer in Section 3.3.

3.1 Magnetic Resonance Imaging

A magnetic resonance scanner utilises strong magnetic fields and radiowaves to produce images of the human body [41, 42]. The human body consists of 75-80% of water (H_2O). Normally the protons (H^+) spin or precess and this movement of the electric charge produces a magnetic field. This is illustrated for a single proton in Figure 3.1.

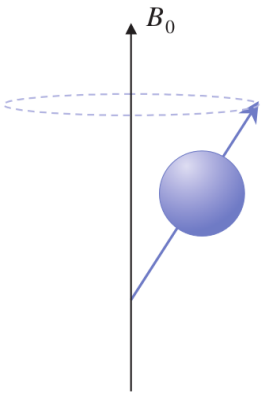

Figure 3.1: Proton precessing around the direction of a strong external magnetic field B_O. The spin produces a net magnetisation in the direction of the magnetic field. Illustration from [43].

The precessing protons of the body can be illustrated as small magnets, and normally the direction of these magnets is randomly distributed, as illustrated in Figure 3.2 to the left. However, when the human body is placed inside a strong magnetic field B_0, the protons will align to that field either parallel or antiparallel, as illustrated in Figure 3.2 to the right, and precess around the direction of this strong field.

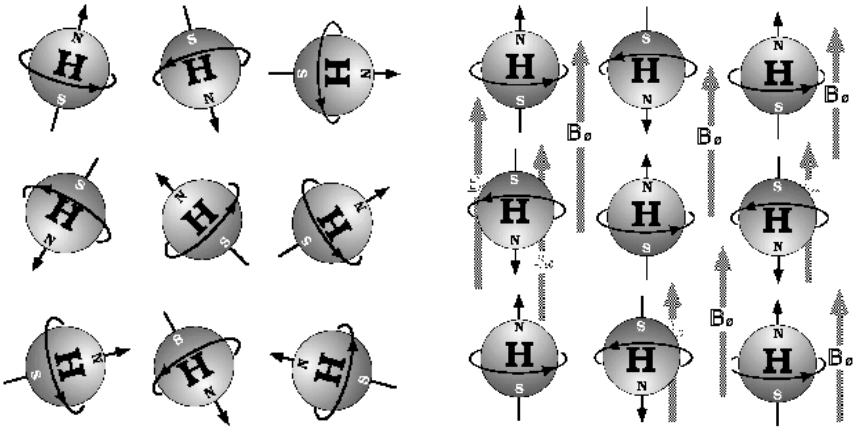

Figure 3.2: Normally, the directions of the protons are randomly distributed, while in an external magnetic field, the protons align parallel or antiparallel to that field. Illustration from [43].

A majority of the protons, the net magnetisation of the protons M_0, will align in parallel with the external field B_0, and they will be in a low energy state, while the protons being antiparallel to the external field B_0 will be in a high energy state. Each proton oscillates between these energy states, but there will always be a slight excess of protons in the low energy state. Each proton spins at a frequency ω_0 proportional to the magnetic field B_0 as in Equation 3.1.

$$\omega_0 = \gamma \cdot B_0 \tag{3.1}$$

γ is the gyromagnetic ratio and is unique for each atom. The $\gamma = 42.56$ MHz/T for protons. Trying to measure the magnetic field of the human body, while at equilibrium in the external magnetic field B_0 is almost impossible, as the induced magnetic field strength of the body is small (around 1 μT) compared to the strong external magnetic field (often 1.5 or 3 T). If energy is supplied to the system in form of electromagnetic radio frequency (RF) pulse at the frequency ω_0, the protons absorb this energy and move to the high energy state. This causes the net magnetisation M_0 to become antiparallel to the external magnetic field B_0, i.e. to flip away from the direction of B_0, and thus the net magnetisation is isolated from the external magnetic field and can be measured. In a representation using the coordinate system in Figure 3.3, at first the net magnetisation M_0 is in the z-direction, however, after the application of the RF pulse, M_0 aligns with the xy-plane instead. The degree to which the net magnetisation M_0 flips from the z-direction, i.e. the direction of the external magnetic field B_0, depends on the amount of RF energy supplied. If the supplied energy causes a equilibrium between the protons in the high and low energy states then the net magnetisation will align with the xy-plane.

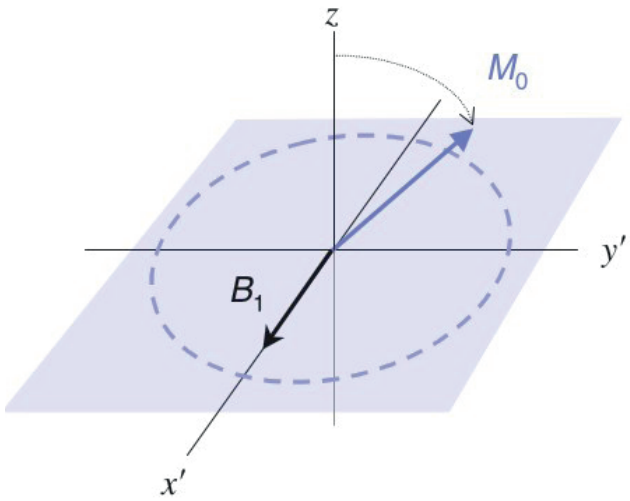

Figure 3.3: Applying energy to the system will change the direction of the net magnetisation M_0 from being aligned with the z-axis to being aligned with the xy-plane. Illustration from [44].

After the RF pulse has been applied, three phenomena occur simultaneously. First, when the net magnetisation M_0 moves away from the z-direction, it will still precess around the external magnetic field B_0, and this rotating magnetic field produces electromagnetic radiation emitted as RF waves. This is the MR signal. Second, the net magnetisation M_0 will return to the z-direction (spin-lattice), and third, the excited protons will dephase (spin-spin). These three phenomena contribute to the production of image contrast in the MR images and will be described in the following section.

3.1.1 MR Image Contrast

Image contrast is the relative difference of signal intensities in the image and may be weighted to demonstrate different anatomical structures or pathologies. By means of different time settings in the scanner, MRI can image anatomical properties of the body as well as functional properties. The time settings control first the application of the RF pulse sequence, i.e. the supply of energy to the system, and second the time for the measurement of emitted MR signal.

Anatomical MRI

After the application of a RF pulse, the protons will return to their equilibrium, and different tissues can be differentiated based on the time taken for this return. In particular, two time measures can be useful for this differentiation, the T1 and the T2.

T1 Weighted Imaging

T1 or spin-lattice refers to the time course whereby the net magnetisation M_0 realigns with the external magnetic field B_0. This is called the longitudinal relaxation time. T1 is unique to every tissue and can, for example, be affected by how much of the energy is used to heat up the

surrounding (lattice) tissue and is mathematically described by an exponential function. An example of a T1 recovery curve is illustrated in Figure 3.4. More specific, T1 is the time taken for 63.2% of the magnetisation to recover its alignment with the external magnetic field B_0.

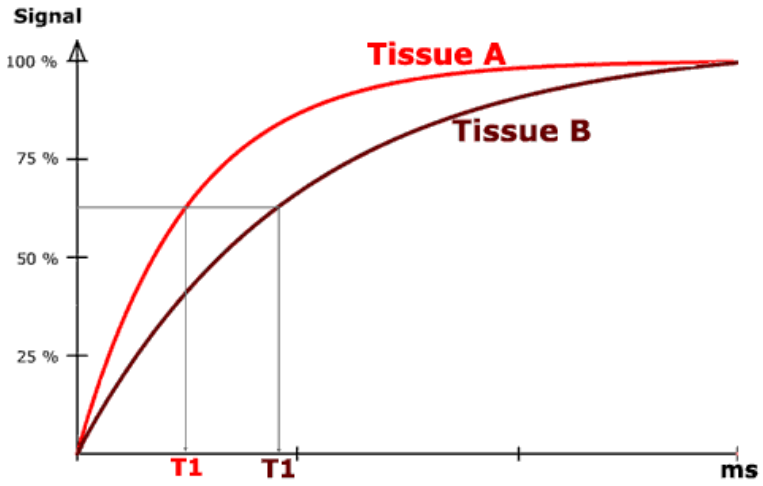

Figure 3.4: T1 recovery curve. Tissue A and tissue B are differentiable using T1 as the contrast-providing parameter. Illustration from [45].

An image is said to be T1-weighted (T1W), if most of the contrast between tissues is due to differences in the T1 times, and is typically created by using short TE and TR times [44].

T2 Weighted Imaging

Where T1 refers the longitudinal relaxation time of the protons, T2 or spin-spin refers to the transverse relaxation time [44, 46]. Right when the RF pulse is applied, the net magnetisation tilts to the xy-plane, the transverse plane, and at that exact moment they will be in phase. However, soon they will start to dephase due to spin-spin relaxation of the protons and inhomogeneity of the external magnetic field B_0: If protons are evenly distributed in a volume, they all precess at the Larmor frequency and remain in phase. However, if two protons come close together, they experience a change (δB) in the magnetic field (B_0), which instantaneously will affect their precessional frequencies, as they will align to the new magnetic field ($B_0 + \delta B$). This is illustrated in Figure 3.5a. Following this change, each proton will dephase with respect to the Larmor frequency, and when two protons move apart, they both precess at the Larmor frequency, however, they have acquired new phase angles. Over time, after many interactions with other protons, the phase angles increase until all protons are out of phase with each other. T2 is the time taken for the transverse magnetisation to drop to 37% of its initial size. The signal detected by the MR receiver is the vector sum of these magnetic moments and will decay to zero as illustrated in Figure 3.5b.

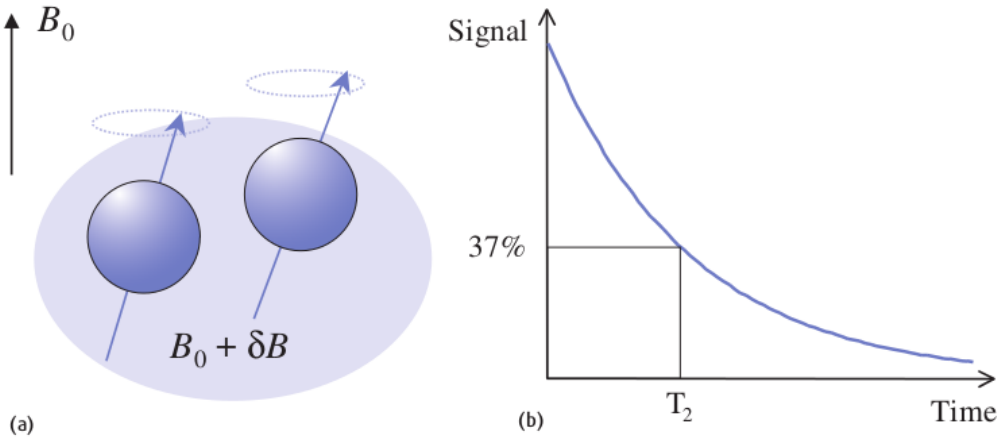

Figure 3.5: a) As two protons come close together, they experience a change in the magnetic field (δB) which changes their precessional frequency and energy is emitted. **b)** The resultant transverse magnetisation decays to zero, because the interactions are random in the end of the RF pulse. Illustration from [44].

T2-weighted (T2W) images have image contrast between tissues due to differences in the T2 times. They can be achieved by selecting a short time between the successive applications of RF energy, most preferably shorter than the T1 for the tissue of interest, and by measuring the emitted MR signal sooner than the T2 for the tissue of interest. The longitudinal realigning (T1) of M_0 to its equilibrium normally takes seconds, while the dephasing of the transverse magnetisation (T2) normally takes some hundred milliseconds, and thus T1 is much larger than T2. This is illustrated in Figure 3.6. Different tissues have different relaxation times and different saturations, and can thus be differentiated based on T1 or T2, for instance. In the table in Figure 3.6, typically selected values of T1 and T2 for different tissues at 3 T are shown.

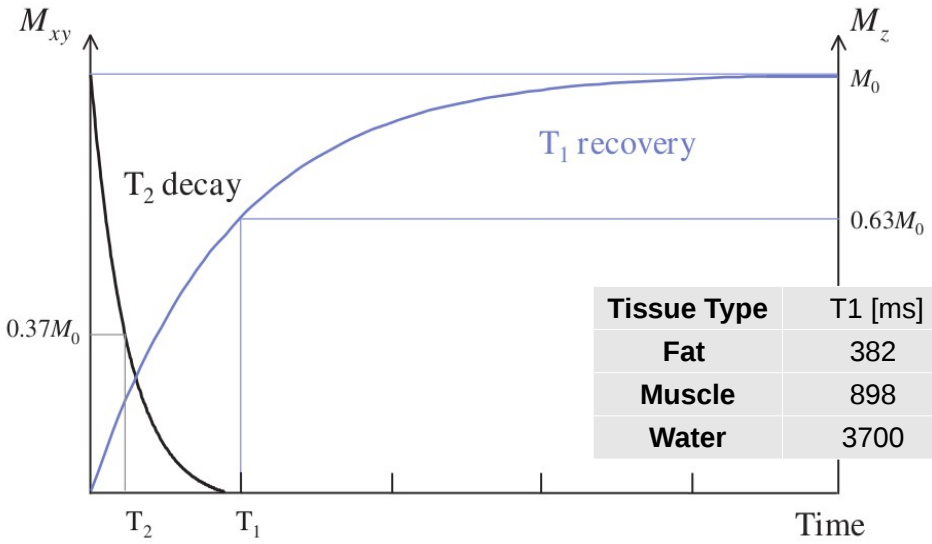

Tissue Type	T1 [ms]	T2 [ms]
Fat	382	68
Muscle	898	29
Water	3700	3700

Figure 3.6: Plot of T1 and T2 relaxation times. They occur simultaneously, but T2 is much shorter than T1 as can be seen from the listed T1 and T2 times for different types of tissue at 3 T. Illustrations freely adapted from [44] and [47].

Physiological MRI

Among the techniques for acquisition of physiological MRI are diffusion weighted (DW) MRI which can provide information on the diffusion of water molecules in tissues, and dynamic contrast-enhanced (DCE) MRI which can provide information on the microvascularity of the tissues [8].

Diffusion Weighted Imaging

In diffusion weighted imaging (DWI), the signal intensity of a volume element (voxel) is an estimate of the rate of water diffusion at that location. This estimate is basically a mean path length L that protons travel in the extracellular fluid within a specific observation time [48]. From Figure 3.7 it can be seen that for a highly cellular tissue, the mean path length L will be smaller than that of less dense tissue.

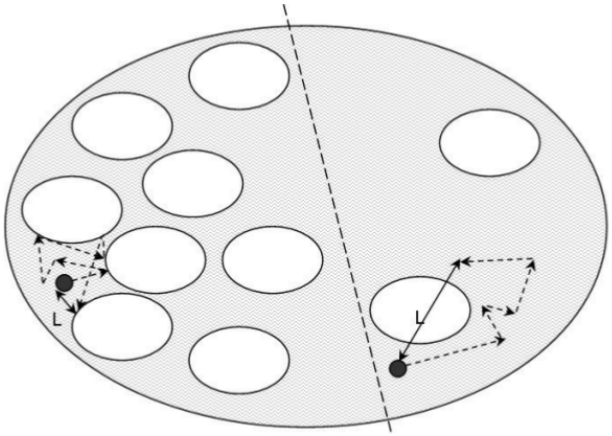

Figure 3.7: The mean path length L travelled by protons is larger in regions of low cellularity compared to tissues with higher cellularity. Illustration from [48].

To obtain DW images, a pair of strong gradient pulses are applied, the first gradient pulse dephases the spins of the protons, and the second gradient pulse rephases the spins of the protons if no movement of water occurs. If water movement occurs, the signal intensities in DWI are attenuated depending on the cellular environment in which the water molecules diffuse and on the specific diffusion weighting (b-value) among other factors [49]. The b-value can be adjusted by changing the time for which the gradient pulse is applied, the time between the two gradient pulses, and the amplitudes of the gradient pulses. The sensitivity to diffusion in the resulting images is correlated with the b-value. DWI using a b-value of zero produces a pure T2W image, while DWI using a higher b-value increases the sensitivity to diffusion. At low b-values ($b < 100 - 150\text{s/mm}^2$), molecules with a large path length due to e.g. blood flow and perfusion shows signal attenuation, while at high b-values ($b > 1000texts/\text{mm}^2$) molecules with a small path length shows signal attenuation, and as the b-value is increased, larger path lengths will be attenuated as well [50].

Tissues having a long T2 relaxation time and/or a high signal intensity can 'shine through' in the DW images, which can cause a misreading of the images [51, 52]. This T2-shine through effect is more pronounced in DW images with low b-values compared to DW images with high b-values. Due to the T2-shine trough effect, DW images should only be assessed qualitatively.

Fortunately, ways to accommodate for the T2-shine through effect exist and the important physiological information that DW images bring can be exploited.

By measuring an apparent diffusion coefficient (ADC), a quantitative measure of the diffusion is obtainable [49]. From two or more sets of DW images with different b-values, the associated ADC value for each voxel can be computed using Equation 3.2 and mapped into a parametric image, the so-called ADC map.

$$\mathrm{ADC} = \frac{-\ln(\frac{S_0}{S_1})}{b_0 - b_1} \tag{3.2}$$

In this S_0 and S_1 are the signal intensities obtained with the b-values of b_0 and b_1. As expected from Equation 3.2, plotting this linear relationship between the diffusion MRI signal attenuation $\ln(\frac{S_0}{S_1})$ and the difference in b-value, results in a straight line, the slope of which is the ADC value, as seen in Figure 3.8. The T2-shine through effect can be seen in this plot as water (blue line) with its long T2 relaxation time and thus high signal intensity will 'shine' more than the remaining tissues (red and black). However, as the b-value increases, the effect of T2-shine through diminishes.

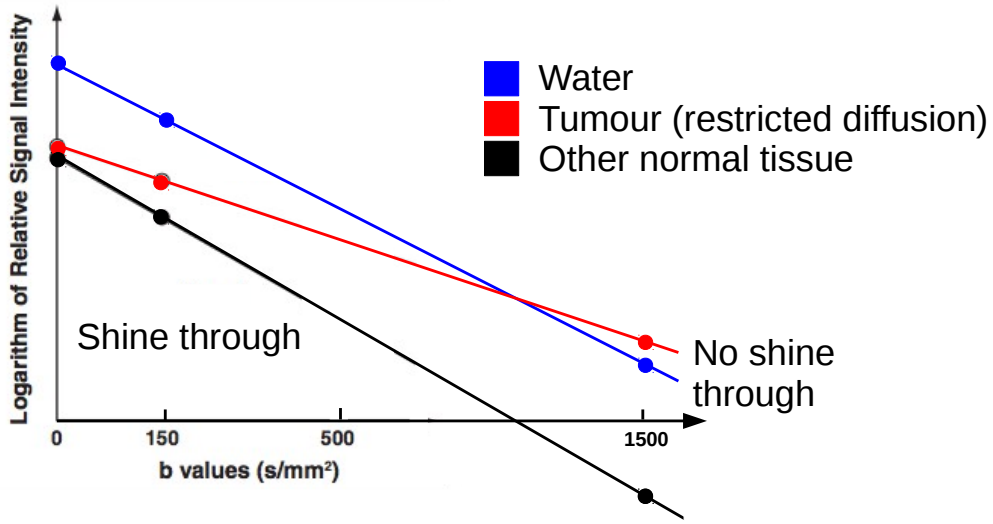

Figure 3.8: The diffusion MR imaging signal attenuation $\ln(\frac{S_0}{S_1})$ against the b-value. The ADC value for the voxel is the slope of the line acquired using multiple b-values. T2-shine through effect is seen for low b-values as the T2 signal intensity is larger than the signal intensities due to diffusion of water molecules. Illustration freely adapted from [50].

Different types of tissues with different ADC values will produce different lines in the plot in Figure 3.8, and thus the different types of tissues become differentiable. Since the ADC values origin from a set of DW images acquired with different b-values and also different time stamps, some extent of motion blur in the ADC map will typically be seen.

Dynamic Contrast-Enhanced Imaging

The perfusion or microvascularity of tissues can be studied using dynamic-contrast enhanced MRI (DCE-MRI) [22, 53]. The image acquisition procedure is composed of fast MRI sequences

obtained before, during, and after an intravenous administration of a contrast agent. Tissues containing MRI contrast agents will have altered the relaxation times of its atoms. The most commonly used contrast agent for the enhancement of tissue microvasculature is the element gadolinium (Gd). Magnetic susceptibility is the extent to which a material becomes magnetised when placed within a magnetic field. Most body tissues have diamagnetic susceptibility, which means that they have no intrinsic magnetic moment, but when placed in a magnetic field they weakly repel the field, resulting in a small negative magnetic susceptibility [54]. This is illustrated in Figure 3.9 to the left. On the other hand, Gd has paramagnetic susceptibility because it has many unpaired electrons. This results in a positive magnetic susceptibility [55] and is illustrated in Figure 3.9 to the right. Paramagnetic materials do not retain the magnetic properties when the external field is removed.

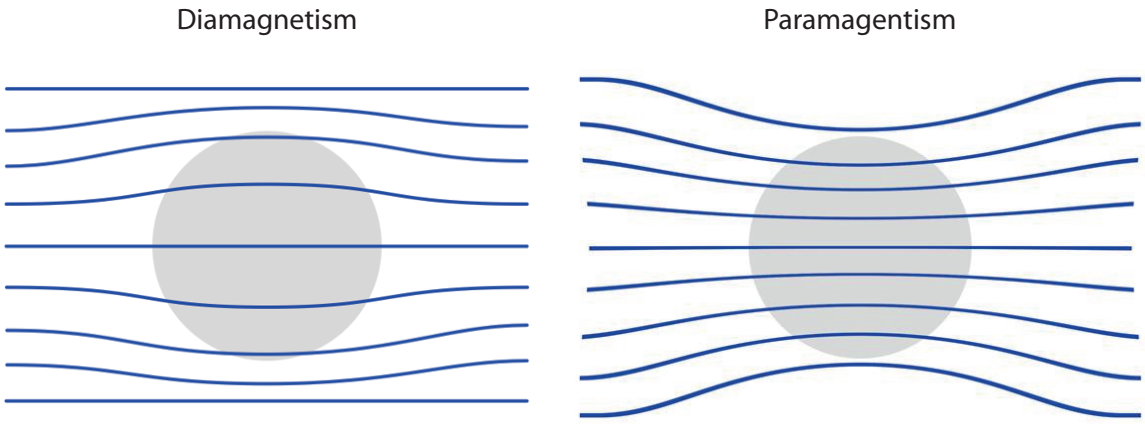

Figure 3.9: The effects of a diamagnetic material (**left**) and a paramagnetic material (**right**) on an external magnetic field. Illustrations from [54, 55].

MRI imaging relies upon the signal generated from the protons in an external magnetic field B_0 after the application of a RF pulse. The relaxation of the protons is affected by surrounding tissues and, when a paramagnetic contrast agent such as Gd has been absorbed in the tissue, the T1 of the protons will decrease. Letting $\mathrm{T1}_0$ denote the T1 time prior to the injection of Gd, T1 denote the T1 time after injection of the Gd, r_1 denote the *in vitro* relaxivity, and C denote the concentration of Gd, then the decrease in T1 time is given by Equation 3.3.

$$\frac{1}{\mathrm{T1}} = \frac{1}{\mathrm{T1}_0} + r_1 C \tag{3.3}$$

However, as seen from Equation 3.3, this MR signal is not directly proportional to the Gd concentration C, which is a necessary condition if quantitative analysis is to be made. Therefore, $\mathrm{T1}_0$ is determined before the scan and afterwards the MR images are corrected for in order to produce images in which the signal intensity is proportional to the Gd concentration.

A transfer constant K_{trans} characterises the flow of Gd across the endothelium into the extravascular extracellular space (EES). The value of K_{trans} is influenced by the structure and surface area of the vessels, and the increased permeability related to conditions with disordered structure and large surface area of vessels will cause large K_{trans} values. K_{trans} can be estimated using pharmacokinetic modelling and the Tofts standard model, which considers the intravascular space (blood plasma) and the EES as two separate compartments [56]. This model is illustrated in Figure 3.10.

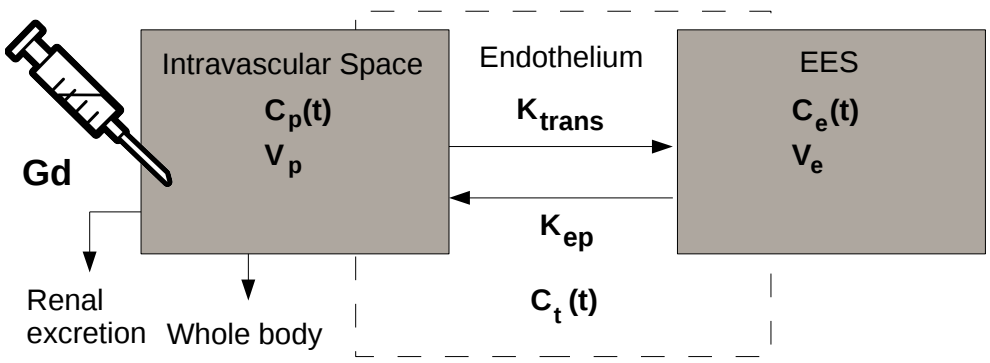

Figure 3.10: Tofts standard model. Illustration freely adapted from [56].

C_p, C_t, and C_e are the arterial concentration, the tissue concentration, and the EES concentration of Gd, the contrast agent, K_{trans} is the volume transfer constant from the blood plasma into the EES, K_{ep} is the volume transfer constant from the EES back to the blood plasma, V_p is the blood volume per unit of tissue, V_e is the total EES volume. Using this model, the contrast agent uptake within a given region can be approximated as in Equation 3.4 [56].

$$V_e \frac{\delta C_e(t)}{\delta t} = K_{trans}(C_p(t) - C_e(t)) \tag{3.4}$$

The arterial plasma concentration Cp(t) can be computed from the blood signal in the images. The solution to Equation 3.4 is the contrast enhancement curve given by Equation 3.5.

$$C_t(t) = V_p C_p(t) + K_{trans} \int_0^t C_p(\tau) \mathrm{e}^{-K_{ep}(t-\tau)}\, d\tau \tag{3.5}$$

K_{trans} and K_{ep} are related by Equation 3.6.

$$V_e = \frac{K_{trans}}{K_{ep}} \tag{3.6}$$

The differences in the contrast enhancement curve shape and time of peak enhancement are important parameters for the differentiation of tissues with different K_{trans} values. The initial slope of the contrast enhancement curve depends on the value of K_{trans}. Figure 3.11 shows an example of three contrast enhancement curve, each with a different value of K_{trans}.

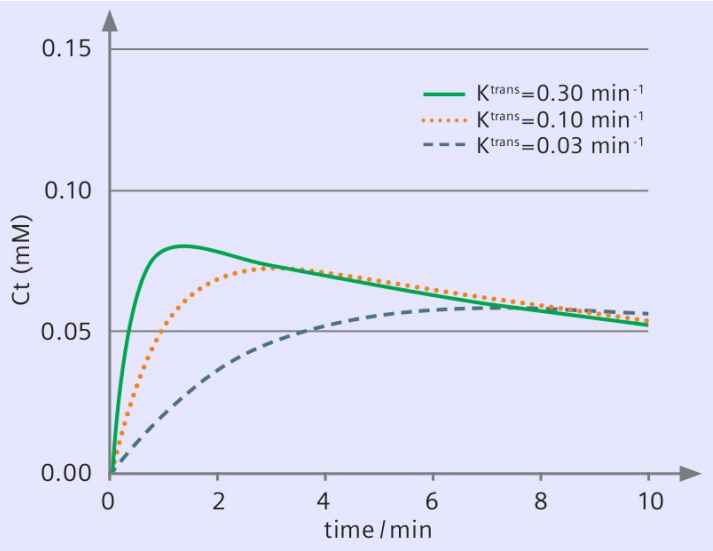

Figure 3.11: Three contrast enhancement curves, each is differentiable from the others due to their different values of K_{trans}. Figure from [57].

Computing K_{trans} values voxel per voxel produces a parametric map, the K_{trans} map, which allows for the study of K_{trans} across an organ.

Other advanced MRI techniques exist, such as proton MR spectroscopic imaging [8, 58, 59], however these are beyond the scope of this project.

3.1.2 MR Scanner

An MR scanner is made up of four components: a magnet, gradient coils, RF transmitter and receiver, and a computer. These components are illustrated in Figure 3.12 to the left. The magnet is a superconducting magnet able to create magnetic fields of the strength of typically 1.5-3 T. The appropriate spatial localisation within the subject is obtained by means of three sets of gradient coils in the MR scanner, one for each of the x, y, and z directions in the image space. Each set of gradient coils is required to produce a linear variation in field along one direction, and in order to minimise the current requirements and heat deposition, they need to have high efficiency, low inductance, and low resistance. RF coils serve as both the transmitter and the receiver of the MR signals. An example of a RF coil used for pelvic MRI is illustrated in Figure 3.12 to the right. Preferably these coils are placed as close to the body part under examination, and that is why they are shaped for their purpose. Finally, a computer handles the control of the MR scanner in terms of shapes of gradients and RF pulses.

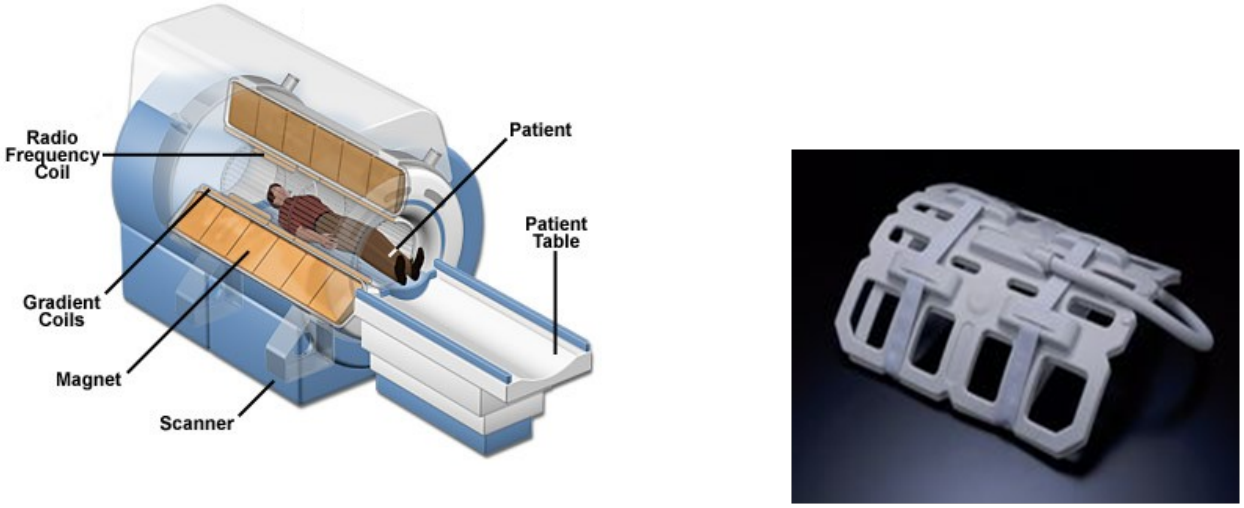

Figure 3.12: Left: A typical MR scanner with three of its main components; the magnet, gradient coils, RF transmitter and receiver. Image from [60]. **Right:** A RF coil used for MRI of the pelvic region. Image from [61].

3.1.3 MR Image Acquisition

To get an idea of the acquisition of an MR image, a one-dimensional case is considered. The frequency of the precession of the protons gives information on the magnetic field they experience. So by letting the magnetic field B_0 vary slightly from point to point, each spatial position will have its own resonant frequency. By applying a known perturbation of the spatial variation of the field, the frequency information of the protons becomes spatial information. Slice selection is a technique to isolate a single plane in the object being imaged, and is achieved by applying a one-dimensional linear magnetic field gradient during the period that the RF pulse is applied. In this way, only the protons whose Larmor frequency, which now is dictated by their position, is the same as the frequency of the applied RF pulse will be excited.

Figure 3.13 provides an example, where the magnetic field varies from 1.4 T at the feet of the subject to 1.6 T at the head of the subject [46]. By applying a RF pulse of a certain frequency range to the patient, signals corresponding to a slice of the subject at the level of the magnetic field corresponding to that frequency will be emitted. The bandwidth of the applied frequency range determines the slice thickness of the MR images.

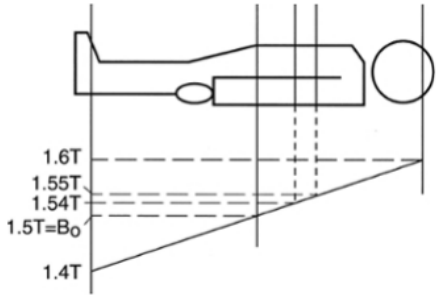

Figure 3.13: An example of slice selection. The magnetic field is varied by means of gradient coils, and the emitted MR signals now has an associated spatial location useful for the imaging. Illustration from [46].

The imaging in the remaining dimensions is technically achieved by means of phase encoding, a technique which can be studied in [44].

3.2 Multiparametric MRI

Multiparametric MRI is defined as the integration of information from different anatomical and physiological MRI datasets [62], i.e. a combination of images from multiple types of MRI techniques. In multiparametric MRI, the individual MRI techniques reinforce or complement each other, and multiparametric MRI has the potential of enhancing the diagnostic value of MRI in prostate cancer. Multiparametric MRI provides a noninvasive approach of characterizing the anatomy (T2WI), angiogenesis (DCE-MRI), and cell density (DWI) of prostate cancer [25]. Prostate cancer localisation is the most important clinical indication for multiparametric MRI of the prostate [8]. The parameters derived from different MRI techniques have been demonstrated to alter in cancer tissue compared to normal prostate tissue.

MRI data using more MRI techniques can be combined in several ways. More studies have proven an increased performance in terms of sensitivity and specificity in prostate cancer localisation when utilising both the anatomical information of T2WI and the physiological information of DWI and/or DCE-MRI, compared to the use of a single MRI technique [63, 64, 65, 66, 67, 68, 69, 70, 71]. In most of these studies, the performances of single and combined MRI techniques have been validated against a whole-mount histopathological examination as the reference standard.

3.3 Clinical Application of Magnetic Resonance Imaging of the Prostate

To be able to differentiate prostate cancer tissue from healthy prostate tissue from multiparametric MRI, the appearance of prostate cancer in T2W images, DW images, ADC maps, and K_{trans} maps is described in the following sections.

3.3.1 T2 Weighted Images

In T2W images, the normal healthy prostate can be divided into the three anatomical regions cf. Section 2.1, the PZ, CZ, and TZ. The PZ is identifiable based on its high intensities, whereas the CZ and TZ appear in a lower range of intensities [8, 72]. On the other hand, prostate cancer typically manifests as a round or ill-defined, hypointense region with homogeneous texture, which makes it easy to distinguish from the hyperintense PZ, but it becomes a more challenging task in the hypointense TZ and CZ [8]. It has been reported that aggressive cancers tend to have a lower signal intensity than indolent cancers [25].

There are some limitations in using T2W images in the detection of prostate cancer. In the PZ, benign abnormalities such as prostatitis, haemorrhage, or atrophy appear in the same intensity range as cancer [8, 22]. In the TZ which often suffers from benign prostate hyperplasia (BHP), it can be hard to differentiate this benign condition from prostate cancer as well based solely on intensities. However, BPH is reported to be more well-defined and inhomogenous compared to cancer tissue [8].

Figure 3.14 shows a T2W image of a prostate. The arrows indicate hypointense regions, which could be suspicious of cancer. A differentiation of prostate cancer from healthy prostate tissue based solely upon T2WI has been reported to have a sensitivity ranging from 53-91% and a specificity ranging from 60-80.5% [63, 64, 67].

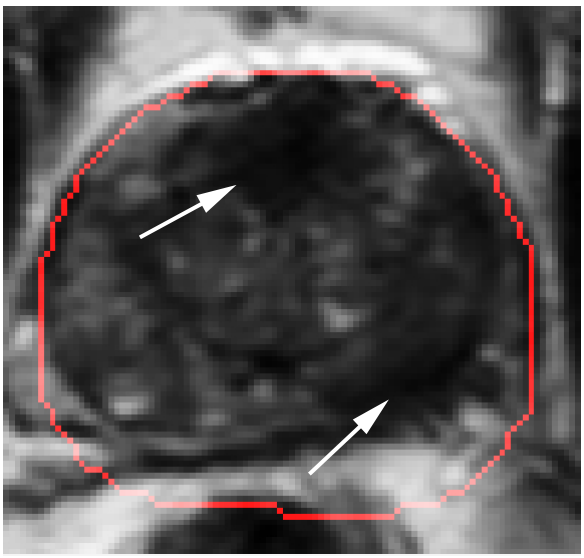

Figure 3.14: Axial T2W image of the prostate from a 72-year-old male diagnosed with prostate cancer. The boundary of the prostate is shown in red. The arrows indicate hypointense areas suspicious of cancer.

3.3.2 Diffusion Weighted Images

In DW images, normal prostate tissue appears in a range of low intensities, due to its tubular structure which allows for extensive diffusion of water molecules [8, 52, 71]. On the other hand, the normal glandular structures have been destroyed in prostate cancer tissue. This tissue thus has a higher cellular density than normal prostate tissue, which results in restricted diffusion

and an appearance of high signal intensities in DW images. The accuracy of detecting prostate cancer within DW images has been improved by using high b-values of 1000-2000 s/mm^2, as benign conditions then becomes differentiable from cancer [8]. However, cancer localisation based solely upon DW images has a major drawback due to the T2-shine through effect, even though this has been reported to be minimal in DW images with a high b-value [52].

In the ADC maps, the ADC values are high for normal prostate tissue and lower for prostate cancer tissue [8]. However, some benign diseases such as prostatitis of the PZ and BPH in the TZ may also cause a low ADC value [52]. Noteworthy, an overlap of the ADC values of normal and prostate cancer tissue, both within and between subjects, has been reported [8, 52]. Moreover, the ADC value is correlated with age, producing a lower contrast between cancer and normal tissue for younger patients compared to the contrast seen for older patients [52]. Additionally, it has been reported that the more advanced or aggressive the tumour is, the larger the contrast between normal prostate tissue and cancer tissue will appear [52]. Studies have found a correlation between the ADC values and the Gleason scores for prostate tumours [73, 74].

Compared to T2WI, the contrast resolution of DWI is high, however, the spatial resolution of DWI is decreased, thus the anatomical location and tumour spread may be difficult to evaluate [52]. To overcome this, DW images with a high b-value and ADC maps should both be evaluated with corresponding anatomical images such as T2W images [8, 52].

Figure 3.15 shows a DW image and its associated ADC map of a prostate. The arrows indicate regions suspicious for cancer. The use of DWI in addition with T2WI has been reported to have a sensitivity ranging from 71-93% and a specificity ranging from 61-77% [63, 64].

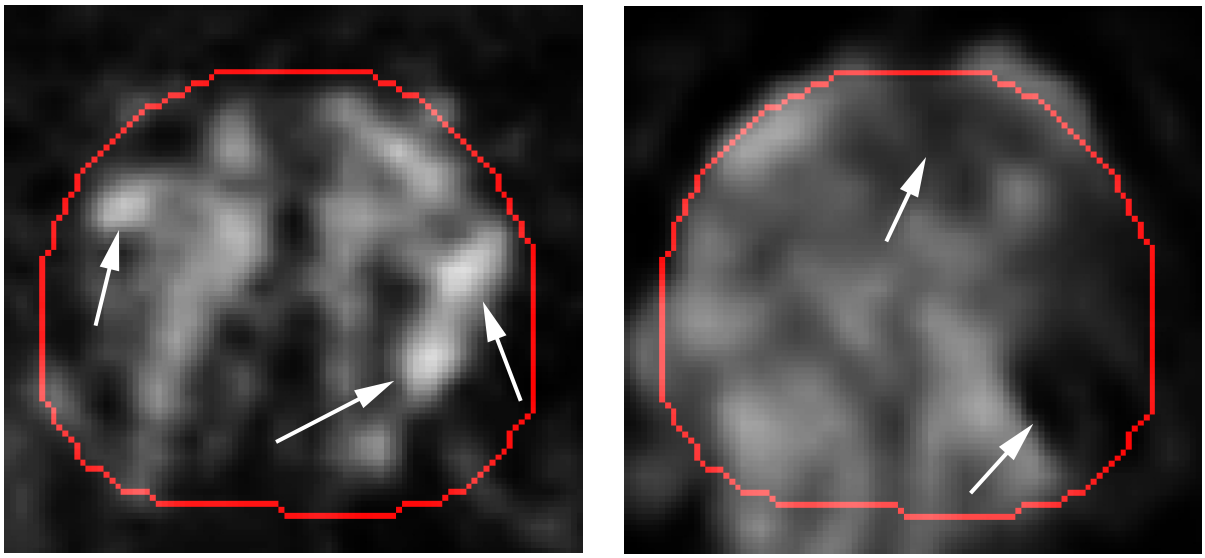

Figure 3.15: Axial DW image of prostate from a 72-years-old male diagnosed with prostate cancer. The boundary of the prostate is shown in red. **Left:** DW image acquired with $b = 2000$ s/mm^2. **Right:** ADC map from same slice. The red circle surrounds the prostate. The arrows indicate areas suspicious for cancer.

3.3.3 Dynamic Contrast-Enhanced Images

As tumours develop and grow, their demands for nutrition increase which causes secretion of vascular growth factors and as a consequence, new vessels form. This is termed angiogenesis and changes the vascular characteristics of the tissue, as seen in Figure 3.16, where substantial differences of both organisation and surface area of the vessels are seen between healthy and cancerous tissue. The vascularity including disorganisation and surface area of the vessels increase, and as a consequence vessel permeability increases compared to the vascular characteristics of normal prostate tissue [8, 22]. The increased permeability of the vessels associated with tissue angiogenesis causes large values of K_{trans}. In K_{trans} maps, regions suspicious for prostate cancer can thus be identified as hyperintense regions, while normal prostate tissue has low K_{trans} values, resulting in hypointense regions.

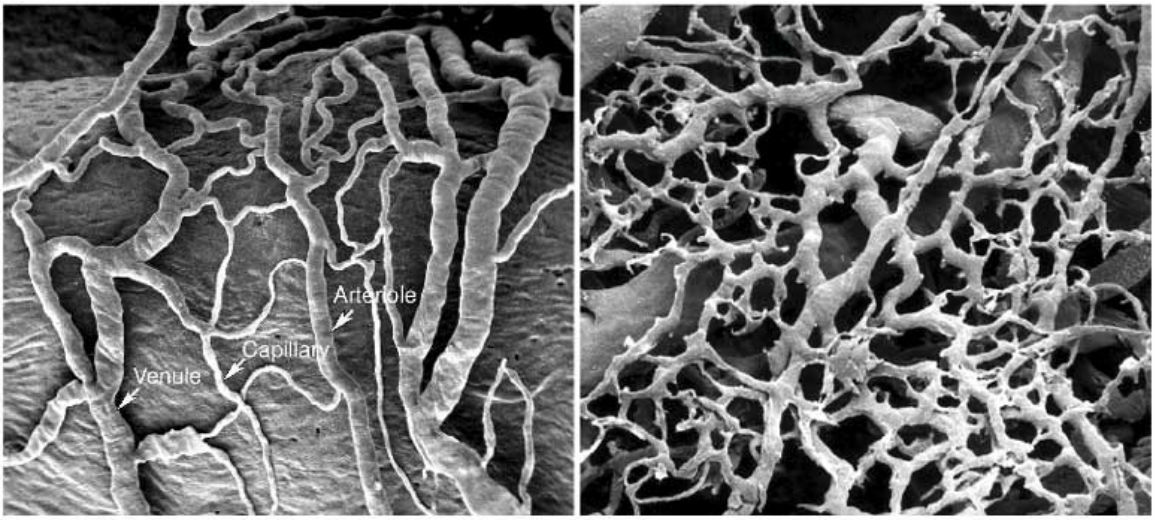

Figure 3.16: Example of angiogenesis. **Left:** Microvasculature of normal tissue with simple, organised arrangement of vessels. **Right:** Microvasculature of cancerous tissue with disorganised vessels. Notice the substantial differences in both organisation and surface area of the vessels. Illustration from [75].

A shortcoming of DCE-MRI is the lack of discrimination of prostate cancer tissue from benign diseases such as prostatitis in the PZ and BPH in the TZ [8]. Figure 3.17 shows a K_{trans} map of a prostate. The arrows indicate hyperintense regions which could be suspicious for cancer.

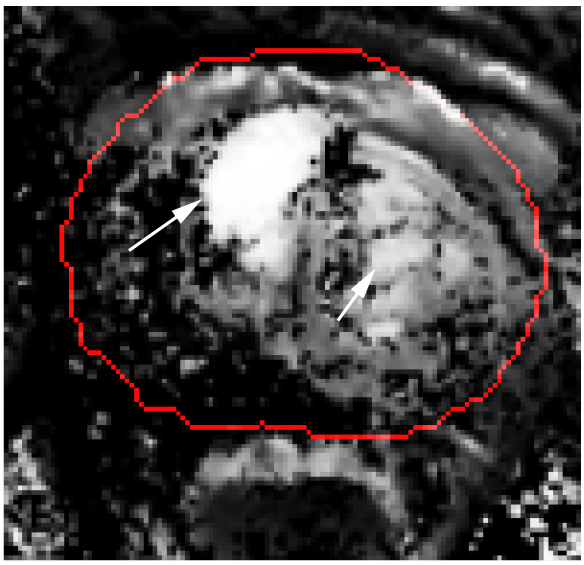

Figure 3.17: Axial K_{trans} map of the prostate from a 69-years-old male diagnosed with prostate cancer. The boundary of the prostate is shown in red. The arrows indicate the regions suspicious for cancer due to their high K_{trans} values.

The use of DCE-MRI in combination with T2WI has shown an increase in sensitivity from 57.5%-73.5% and in specificity from 80.5%-81% when compared to the use of T2WI alone [67]. Similar results have been found by Kim et al. [68] and Ogura et al. [69] using endorectal MRI, though. Furthermore, Delongchamps et al. [70] have proved that the combined use of T2WI, DWI, and DCE-MRI improves of the sensitivity of prostate cancer detection in the PZ from 63%-81%, while maintaining a stable specificity. On the contrary, for the prostate cancer detection in the TZ, they did not find any improvements. However, an increased accuracy in the detection of prostate cancers in the TZ using multiparametric MRI has been found by Yoshizako et al. [71].

Chapter 4

Project Aim

At present, diagnosis of prostate cancer is based on the TRUS-guided biopsy results often described using the Gleason score. However as mentioned earlier, discomfort for the patient and several unfortunate side effects are associated with this procedure, and additionally the poor sensitivity often requests second biopsies. For these reasons, it would be useful to acquire information noninvasively from imaging modalities about tumour presence and more specifically about their localisation [64]. An accurate definition of the prostate cancer localisation could improve the cancer detection in targeted biopsies, enable an accurate staging of the tumour, and help improve and support for focused intensity-modulated therapy planning of the dominant prostate tumour [8].

To integrate as much information as possible about the tissue characteristics and physiology in the distinction of healthy and cancerous prostate tissue, both anatomical and physiological information can be utilised. The MRI modality offers a wide range of different image techniques suited for capturing different tissue characteristica. For instance, T2W images provide the best representation of the anatomy of the prostate. However, diagnosis and staging of prostate cancer based on T2WI alone is not recommended due to its inadequate specificity. Especially the detection of tumours in the TZ is challenged in T2W images, as cancerous tissue manifests in an intensity range similar to that of normal tissue. Coupling the information from T2WI with information from techniques capturing physiological information, such as DWI and DCE-MRI, the specificity has been proved to increase. DWI provides information about the diffusion of water molecules in the tissues, which is known to be decreased for cancerous tissue. The combination of T2WI and DWI improves specificity in prostate cancer detection compared to readings from T2WI alone [63, 64, 65, 66]. Furthermore, the associated ADC values correlate well with the Gleason score. Last but not least, parameters from DCE-MRI, such as K_{trans}, provides information on the microvascularity of the tissues and can aid in the distinction of healthy and cancerous tissue as tumour growth is associated with increased angiogenesis [53]. The combination of all these different MRI techniques is called multiparametric imaging and is becoming the standard for tumour detection in the prostate [9]. Provided the tissue characteristics of cancer from both T2WI, DWI, ADC and K_{trans} maps, the discrimination performance increases so that the presence of prostate cancer can be assessed and well localised for improved diagnosis and treatment planning.

Each MRI technique adds complementary information valuable in cancer diagnostics, however, the manual reading of these multiple data sets requires substantial expertise. Despite different proposals of standardising the manual visual detection and staging of prostate cancer [25], the risks of inter- and intra-observer variability are pronounced. To reduce these shortcomings and increase the diagnostic value of MRI, clinical guidelines for multiparametric MRI of the prostate should be set forth and automatised. Given these points, it is interesting and needed to ask, how can one take advantage of the complementary information from T2WI, DWI, ADC maps, and K_{trans} maps in the diagnosis of prostate cancer?

Based on the above, the following project aim is stated:

Aim
The aim is to present a framework for automated prostate cancer localisation. The framework will take advantage of multiparametric prostate MRI consisting of T2W images, DW images, ADC maps, and K_{trans} maps. The performance of the proposed framework will be validated against a ground truth. The proposed framework should localise true tumours correctly without introducing false positive tumours.

Objectives

1. Investigation of methods for automated prostate cancer segmentation using T2W images, DW images, ADC maps, and K_{trans} maps.
2. Investigation of image features feasible for the distinction of healthy and cancerous tissue in the above types of images.
3. Proposal of framework able to automatically localise prostate tumours using multiparametric MRI.
4. Validation of the proposed framework for automated prostate localisation using multiparametric MRI.

Perspectives
Automated prostate cancer localisation using multiparametric MRI could help reduce the disadvantages of manual readings of the multiparametric MRI data and open the door to prostate cancer screening using MRI. Automated MRI-based prostate cancer localisation could reduce the patient related complications, as in the long term, MRI-based diagnosis could possibly replace the diagnosis based on TRUS-guided biopsies. Furthermore, automated prostate cancer localisation could increase the objectivity in the diagnosis and possibly enable earlier diagnosis and assessment of tumour aggressiveness, and as a consequence, less unnecessary treatments will be performed and thus the extent of unfortunate side effects will reduce, all in all leading to an increase in quality of life for the patient.

Chapter 5

Data and Preprocessing

This chapter describes the data used in the data analysis and evaluation of the proposed framework for automated prostate cancer localisation presented in this project. The data description is divided into descriptions of image data in Section 5.1 and of clinical data in Section 5.2. Section 5.3 outlines the preprocessing of the image data, and lastly, considerations of registration of the image data are outlined in Section 5.4.

The data analysis has been conducted unsupervised with no specifications or annotations of true prostate cancer locations present in the data. However, for the evaluation of the proposed framework of automated prostate cancer localisation expert annotations in the images and biopsy results from all subjects were available.

5.1 Image Data

Data have been acquired from Herlev Hospital (Herlev, Denmark), where they have been acquired using a Philips Healthcare Ingenia 3.0 T MR system. The data have been used in another study on multiparametric MRI for detection of prostate cancer by Lars Boesen [76]. A total of 10 data sets from 10 biopsy-confirmed prostate cancer patients were available, with each data set consisting of T2W images, DW images, ADC maps, DCE images, and K_{trans} maps, all in axial plane. All of the images from each subject origin from the same scan, meaning the subject underwent one complete scan in which all the mentioned MRI techniques were applied sequentially.

Table 5.1 sums up the MRI parameters for the acquisition of the T2W images.

MRI Parameters for T2W Images	
Manufacturer	Philips Medical System
Acquisition Plane	Axial
Field Strength	3.0 T
Flip Angle	90 degree
TE	110 ms
TR	4235 ± 273 ms
X dimension	432 pixels
Y dimension	432 pixels
Z dimension	31 pixels
Pixel Spacing X	0.42 mm
Pixel Spacing Y	0.42 mm
Spacing Between Slices	3.5 mm
Slice Thickness	3 mm
Weighting	T2

Table 5.1: MRI Parameters for the acquisition of the T2W images.

The DW images were acquired with four different diffusion weightings having b equal to 0, 100, 800, and 1400 s/mm^2. To reduce artifacts from potential T2-shine through effect, only DW images with b-value of 1400 s/mm^2 are used in the work here presented. However, the ADC maps were calculated on the basis of all four different DW images with different b-values for each subject. Table 5.2 sums up the MRI parameters for the acquisition of the DW images.

MRI Parameters for DW Images	
Manufacturer	Philips Medical System
Acquisition Plane	Axial
Field Strength	3.0 T
Flip Angle	90 degree
TE	79.3 ms
TR	5210.8 ± 473.9 ms
X dimension	144 pixels
Y dimension	144 pixels
Z dimension	25 pixels
Pixel Spacing X	1.25 mm
Pixel Spacing Y	1.25 mm
Spacing Between Slices	4 mm
Slice Thickness	4 mm
b-values	0, 100, 800, and 1400 s/mm^2
Weighting	T2

Table 5.2: MRI Parameters for the acquisition of the DW images.

A total of 18 T1W DCE image volumes were acquired for each subject with an interval of 16 s between each volume. The K_{trans} maps were calculated based on Tofts standard model using the 18 DCE images from each data set. Table 5.3 sums up the MRI parameters for the

acquisition of the DCE images. Only the K_{trans} maps are used in the work here presented.

MRI Parameters for DCE Images	
Manufacturer	Philips Medical System
Acquisition Plane	Axial
Field Strength	3.0 T
Flip Angle	12°
TE	5.037 ± 0.005 ms
TR	10.239 ± 0.043 ms
X dimension	256 pixels
Y dimension	256 pixels
Z dimension	18 pixels
Pixel Spacing X	0.703125 mm
Pixel Spacing Y	0.703125 mm
Spacing Between Slices	4 mm
Slice Thickness	8 mm
Weighting	T1

Table 5.3: MRI Parameters for the acquisition of the DCE images.

5.2 Clinical Data

Table 5.4 provides an overview of the clinical data of the subjects. The Gleason score is stated as the sum of the Gleason grades, which, to recap, describes the two most prominent histological patterns of the biopsy specimen cf. Section 2.3. As seen in the table most subjects only have a single tumour, while subject 3, subject 4, and subject 10 each has two tumours. The mean age of the subjects is 66.4 years, and the mean Gleason score of the true tumours is 6.77. 46% of the true tumours are located in the PZ, while 54% in the TZ of the prostate.

Subject	Age [years]	Gleason Score First Tumour	Location First Tumour	Gleason Score Second Tumour	Location Second Tumour
1	69	6 (3+3)	TZ	∼	∼
2	65	6 (3+3)	PZ (Apex)	∼	∼
3	71	6 (3+3)	TZ	6 (3+3)	PZ
4	67	7 (4+3)	TZ	6 (3+3)	TZ
5	66	7 (4+3)	PZ	∼	∼
6	62	7 (4+3)	TZ	∼	∼
7	62	7 (4+3)	PZ and TZ	∼	∼
8	67	8 (4+4)	PZ	∼	∼
9	78	9 (5+4)	TZ	∼	∼
10	58	7 (4+3)	PZ	6 (3+3)	TZ

Table 5.4: Clinical data of the subjects.

Data from subject 10 were excluded as the images showed evident signs of a water cyst. Thus the remaining nine subjects have a total of 11 tumours.

5.3 Preprocessing

All images were converted to the MINC file format using the MINC Toolkit [77]. Next, all images from each data set, i.e. T2W images, DW images, ADC maps, and K_{trans} maps for each subject, were manually cropped to enclose just the prostate and then resampled to have isotropic voxel sizes of 0.5 x 0.5 x 0.5 mm.

5.4 Registration of Data

A total multiparametric MRI scan sequence using a body coil including both T2WI, DWI, and DCE-MRI of the subject normally takes around 30 min. During this time, the subject is asked to keep calm and remain still in order to minimise motion blur in the images. Despite the effort to keep the external anatomy of the subject still, internal organs including the prostate can actually move. The prostate can move mainly because of the passage of air, or because adjacent organs such as the bladder and the rectum fill and empty. During a normal MR scan, the prostate can move up to 3 mm, and the movement typically occurs forwardly towards the pubic bone. What is important to notice is that even though the prostate moves, it does not deform, because of its glandular tissue type, unless an endorectal coil is used in the MRI acquisition [78]. In other words, the prostate maintains its shape but its spatial position may change during a MR scan. To take advantage of the complementary information that the different MRI techniques bring, a correct alignment of the sets of MR images is of high importance.

5.4.1 Image Registration

Image registration is the process of aligning two or more images in order to capture and define their similarities or differences. Images can be registered to each other by means of a predetermined geometric transformation which aligns one image to fit another. But determination of such geometric transformation is in many cases the challenge of the image registration itself, and only lies clear once the image registration has been done. The registration of images from different modalities or different techniques within one modality is complicated on account of their highly different image characteristics and contrast. Spatial correlations of images acquired from different modalities or from different techniques may be performed by visually identifying and labelling corresponding regions in the images of interest or by using a semi-automated or fully automated image registration procedure.

In this project, the different images for each subject origin from the same scan sequence. However, even though the subject has remained still during the scan, whether the prostate itself has moved should be checked. For all included subjects, this was manually assessed by highlighting salient points, e.g. selected specific points on the prostate boundary, in one image

and read the position of the corresponding point in another image. This is outlined in Figure 5.1 for one example of pair of images.

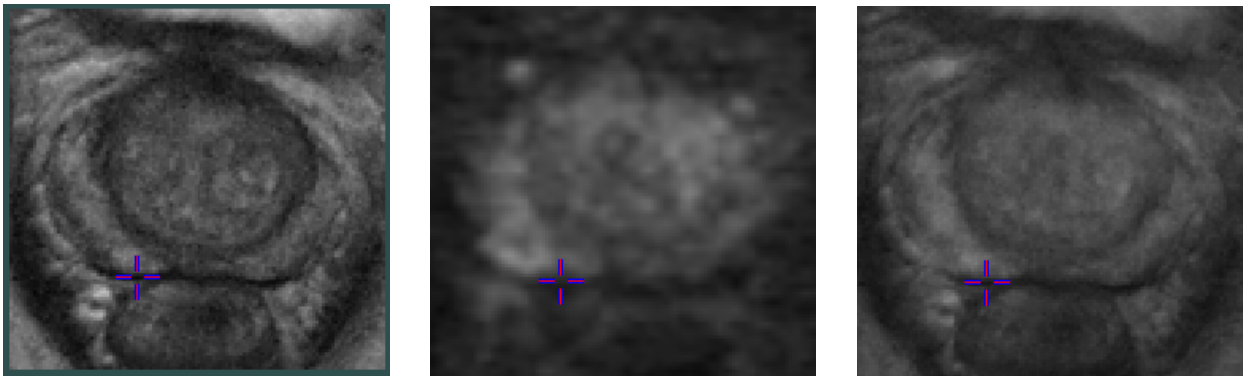

Figure 5.1: Manual inspection of the registration of the available data. **Left:** T2W image with a marker at a selected salient point. **Middle:** DW image with marker at corresponding point. **Right:** Superimposition of one image on the other. The two marker positions coincide.

The approach of marking different positions in one image and assessing the corresponding positions in the other images was repeated, and in all of the data sets fine agreement of the marker positions was seen and hence the images are sufficiently aligned without the application of any geometric transformation.

Chapter 6

Automated Prostate Cancer Localisation

The need for noninvasive, reproducible, and accurate localisation of prostate cancer has resulted in an emerging interest in multiparametric MRI as an alternative to TRUS-guided biopsies for prostate cancer diagnosis [79, 80]. The challenges when localising prostate cancers from MRI are numerous; the overlapping image intensity regions of malign, benign, and healthy tissues, the heterogeneity of the prostate anatomy, etc. [80]. The majority of the studies investigating the use of multiparametric MRI in prostate cancer localisation are based on manual readings and interpretations of the MRI data. As an example, all the studies mentioned in Section 3.2 regarding the advantages of multiparametric MRI in comparison to single MRI techniques are all based on manual readings. However, much work has been done in the field of automated prostate cancer localisation using multiparametric MRI.

This chapter presents previous studies on automated prostate cancer localisation in Section 6.1, and sums up the image analytic challenges in Section 6.2 before outlining the proposed framework here presented in Section 6.3.

6.1 Previous Studies on Automated Prostate Cancer Localisation

Both supervised and unsupervised learning methods for automated prostate cancer localisation using multiparametric MRI have been studied, and a majority of these methods focus on the localisation in the peripheral zone (PZ), as 70-80% of prostate cancers are located in this zone [65, 80, 81, 82, 83]. As a consequence, many methods require a manual segmentation of the PZ. As always, manual interactions have their limitations, and to conquer these, more studies attempt to incorporate spatial information along with the intensity information of the multiparametric MRI in a support vector machine (SVM) [79, 84]. Most supervised methods have been based on such SVMs or variations of these [6, 80, 85, 86, 87].

For an example, Huisman et al. [6] segment the prostate by introducing a parametric multi-object probabilistic anatomy model. Basically, they construct a pelvic model which describes the anatomy and modality appearance of this region, while constraining the model parameters by means of a population model. The population model constrains characteristics, e.g. physical properties, of the individual anatomical objects of the pelvic model to be within certain range, and also retains their contextual relationships. As an example, one of these constraints restricts the diameter of the prostate to range between 2-6 cm and what is modelled as the rectum should be located below the prostate (in axial images). An initial cancer detection is performed by a voxel classifier, and to reduce the number of false positives, in a second step a lesion is characterized and classified using a lesion based classifier. The voxel classifier detects lesions by evaluating among others the volume, principle components, mean values, and quartiles of

quantitative features e.g. the ADC values. All these features are fed into a SVM, and then the lesion classifier takes into account other features such as the third quartile of K_{trans} from DCE images. This two-stage SVM classification has shown good results.

Another approach has been taken by Langer et al. [65], who propose a logistic regression analysis for the detection of prostate cancer in prospective multiparametric MRI data sets. The model is able to compute the probability of malignancy for a given voxel based on its T2W image intensity, ADC and K_{trans} values with an area under the ROC curve (AUC) of 0.706. This area is an estimate of the accuracy of the method to detect prostate cancers, and ranges between 0 and 1 with 1 indicating a perfect detection. The AUC computed from the multiparametric MRI data is significantly larger than the corresponding area computed from either T2WI or DCE MRI alone, however not significantly larger than the area computed from DWI alone.

Niaf et al. [82] propose a computer-aided detection system based on multiparametric MRI able to assist the radiologist in the discrimination of prostate cancer from normal tissue by providing a likelihood measure of prostate cancer presence. From a set of 140 image features, a set of highly discriminative features is selected and the performance of four different supervised classifiers are compared. Ground truth is established by a whole-mount section of prostatectomy specimens. The best segmentation performance is obtained using a SVM (AUC = 0.89) and it is superior to the performance of two radiologists (AUC = 0.80 and 0.86). However, the results are limited to predefined regions of interests and only regions in the PZ are considered.

Yet another approach has been taken by Artan et al. [83] who present a semi-supervised and semi-automated segmentation algorithm. Basically, they extend a graph based semi-supervised random walker algorithm to work in multiparametric MRI. The random walker algorithm is a graph based seeded segmentation algorithm. At first a human rater prelabels a few voxels. Then each unlabelled voxel is assigned a so-called *first arrival probability* for each of the prelabelled voxels. The *first arrival probability* describes the probability that a random walker starting from this specific unlabelled voxel will at first reach that specific prelabelled voxel, before reaching any other prelabelled voxels. The segmentation then proceeds by assigning to each unlabelled voxel the label of the prelabelled voxel for which the largest *first arrival probability* was calculated. Artan et al. obtain segmentation results comparable to other fully automated methods.

The project presented in this report proposes unsupervised methods of automated prostate cancer localisation in multiparametric MRI.

6.2 Image Analytic Challenges in Localisation of Prostate Cancer Using Multiparametric MRI

In the work on automated localisation of prostate cancer using multiparametric MRI, it is important to understand the image analytic challenges that arise. The knowledge of the appearance of prostate cancer in the different types of MR images and parametric maps should be implemented. Table 6.1 provides a summary of the appearance of cancer in the different MRI techniques cf. Section 3.3.

Image Type	Appearance of Cancerous Tissue
T2W Image	Hypointense and homogeneous texture
DW Image	Hyperintense
ADC Map	Hypointense
K_{trans} Map	Hyperintense

Table 6.1: Common assumptions about the appearance of cancerous tissue in T2W images, DW images, ADC maps, and K_{trans} maps.

However, important to remember is the fact that not only cancer tissue has the intensity characteristics as mentioned in Table 6.1. An overlap may occur in the intensity ranges for healthy, benign, and malign tissues, hence making it hard to differentiate between the different tissues. The distinction between benign and malign tissues is especially challenged, if the differentiation is solely based on image intensity information. However, the texture information in the T2W images may provide information enabling a distinction of benign tissue and prostate cancer tissue, since cancerous tissue appears more homogeneously compared to benign tissue. Taking advance of texture information as well, the rate of erroneous cancer localisations may be reduced. Even though there is an overlap in the intensities for healthy, benign, and malign tissue in the different MR images, uniting the intensity information from all images could increase the probability and certainty of localising the true cancer regions in the images.

Given these points, the image analytic challenge is to facilitate localisation of the image regions that best comply with the assumptions of the appearance of cancer, both in terms of intensity range and homogeneity. An obvious first step is segmentation of the prostate in order to limit the further image processing to only concern prostate tissue.

6.3 Proposed Solution for Automated Prostate Cancer Localisation

The framework of automated prostate cancer localisation using multiparametric MRI in the work here proposed consists of three major processing steps, as illustrated in Figure 6.1.

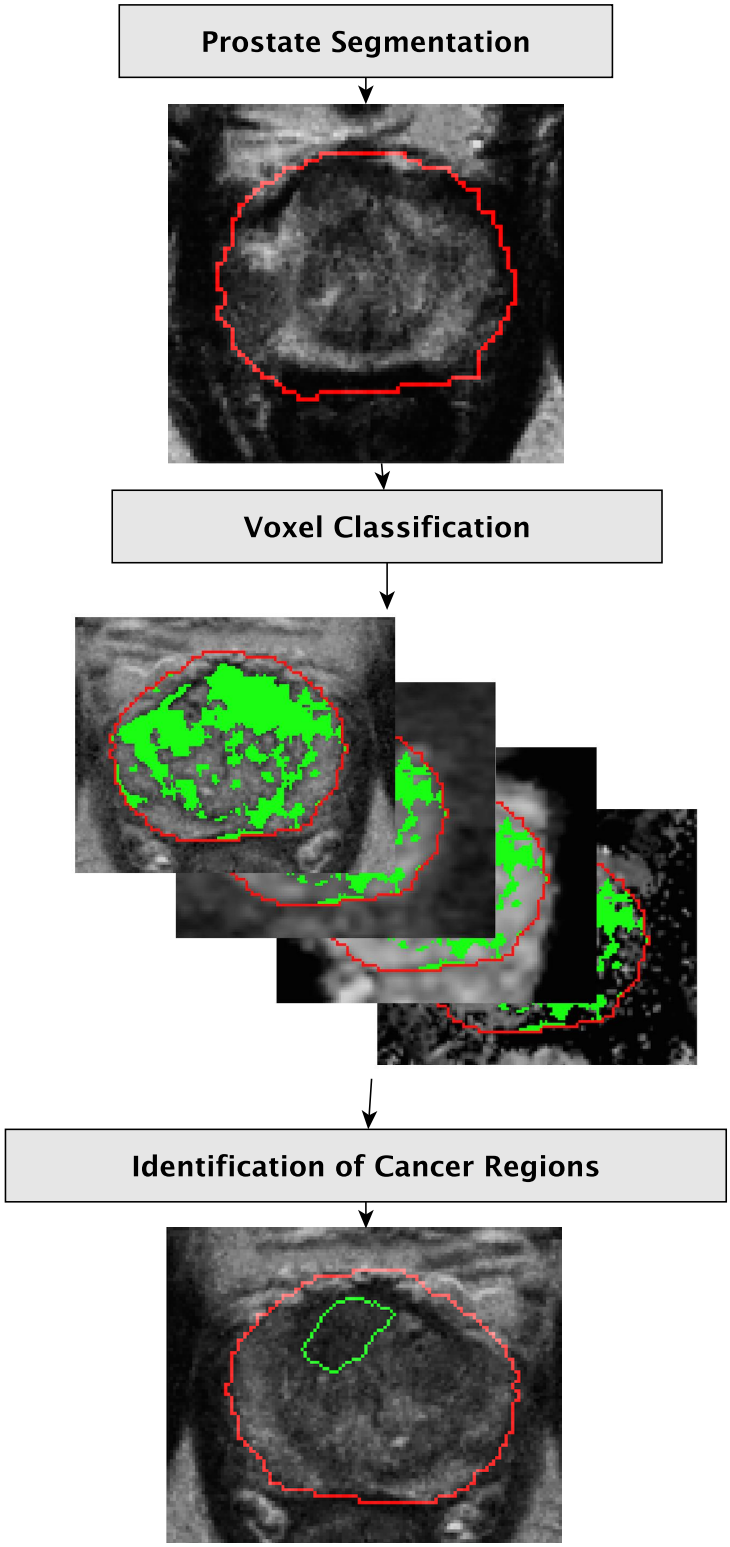

Figure 6.1: Proposed framework of automated prostate cancer localisation using multiparametric MRI. Three tasks are accomplished to localise a tumour using multiparametric MRI data. The red mask is a segmentation of the prostate, and the green masks are examples of prostate cancer localisations.

In this work, the term tumour localisation describes tumour detection as well as an indication of the tumour location. The term tumour detection describes only whether a tumour can be found in the prostate image volume for a subject, and the term tumour localisation elaborates

this by in addition stating the location of the tumour by marking it in the prostate image volume.

The composition of the framework is inspired by the clinical practice of visual inspection of multiparametric MR images. As the first step, a radiologist would identify or segment the prostate. As a second step, the radiologist would look for certain homogeneous intensity ranges within each type of MR images. This knowledge is utilised in the second step of the proposed framework, of which the purpose is a classification of prostate voxels into either cancer candidate voxels or voxels representing normal tissue based on intensity and texture information from T2W images, DW images, ADC maps, and K_{trans} maps. In order to localise prostate cancer as interconnected regions of cancer candidate voxels, the purpose of the third step is to segment the set of cancer candidate voxels into image regions and subsequently classify these regions into either cancer regions, i.e. tumours, or regions representing normal prostate tissue. Two methods are proposed for the segmentation of the set of cancer candidate voxels into image regions, a method based on Laplacian of Gaussian (LoG) edge detection and a method based on watershed transform. They, as well as the remaining methods of each of the three steps, are presented in Figure 6.2.

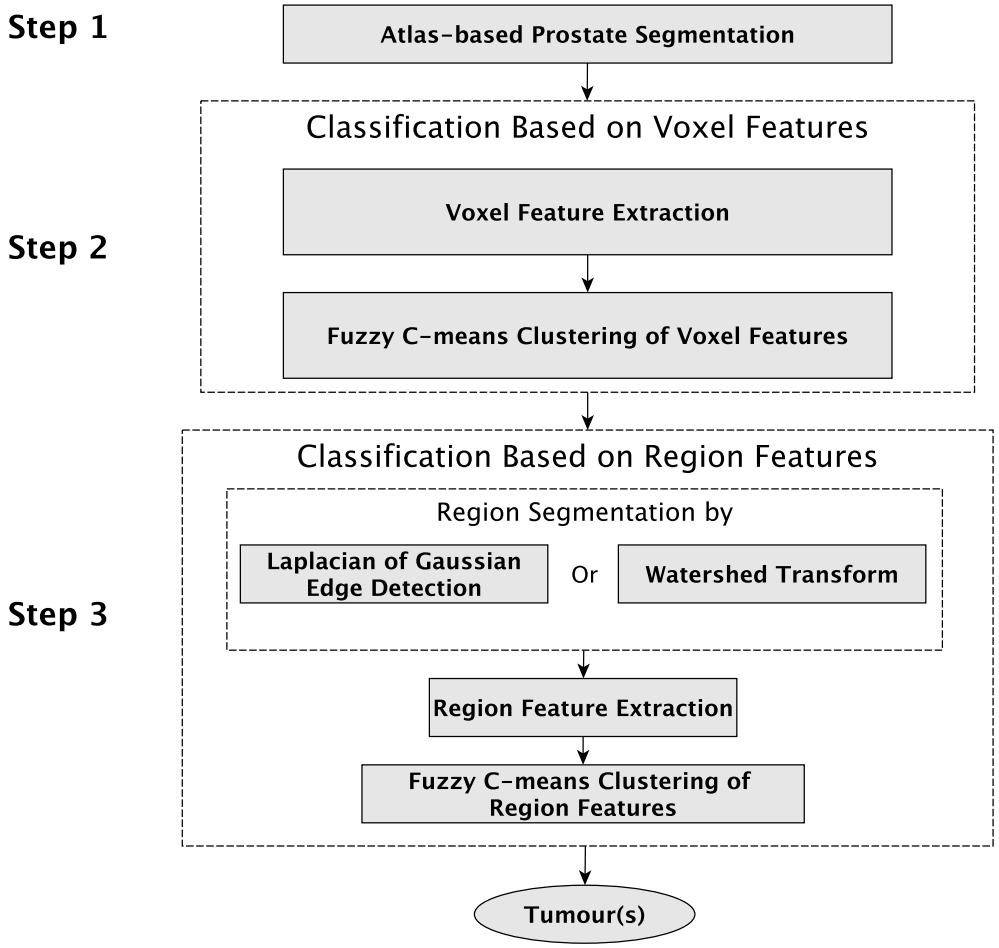

Figure 6.2: Schematic outline of the methods in the proposed two procedures of automated localisation of prostate cancer from multiparametric MRI.

The second and third steps are identical in terms of applied methodology. They both classify small image regions based on a set of features. In the second step features describing voxel

properties are extracted and used in the classification of all prostate voxels into cancer candidate voxels or voxels representing normal prostate tissue. In the third step, image regions are segmented in the set of cancer candidate voxels using either the LoG edge detection method or the watershed transform method, and from the segmented regions a region feature is extracted and used in the classification of the segmented regions into cancer regions or regions representing normal prostate tissue.

To sum up, the proposed framework for automated prostate cancer localisation using multi-parametric MRI consists of three steps. Each step is unfolded in the following chapters. The method for prostate segmentation is presented in Chapter 7, the voxel classification is presented in Chapter 8, and finally the identification of cancer regions is presented in Chapter 9.

Chapter 7

Prostate Segmentation

A segmentation of the prostate is performed to limit the search for prostate cancer to prostate tissue only. An outline of previous work on prostate segmentation is presented in Section 7.1, and the applied technique for prostate segmentation in the framework for automated prostate cancer localisation is presented in Section 7.2.

7.1 Previous Studies on Prostate Segmentation

In the literature, the segmentation of the prostate is of interest for many purposes [88]. Whether the purpose is to locate prostate boundaries for radiation treatment planning, to initialise a multi-modal registration, or as in this project to localise prostate cancer, automatic and accurate segmentation of the prostate is highly valued. In the view of the numerous disadvantages associated with manual segmentation of the prostate, including the time consumption and the risks of inter- and intra-observer variations, both semi- and fully automated methods for prostate segmentation have been researched to a great extent. Such methods are generally challenged by the presence of imaging artifacts produced by air in the intestines or inhomogeneities of the magnetic field. Moreover, inter-subject differences in bladder and rectum fillings and the large anatomical variability between subjects complicate this task. However, important to realise is that the prostate segmentation in this project is merely used for limitation of the search for prostate cancer, so whether the segmentation is absolutely accurate is of less importance.

The majority of the applied techniques for automated prostate segmentation is either model- or atlas-based. Korsager et al. have presented a model-based approach using an active appearance model [89]. In the approach, an appearance model containing shape and texture information is matched to the target image by stating a linear relationship for displacements of the model parameters between model and target, and an induced error vector [90]. The active appearance model by Korsager et al. uses a level set representation of the prostate shape in contrast to the landmark-based approach in the traditional active appearance model. Furthermore the model incorporates a priori information on model and parameter correction. The segmentation approach was validated, giving a mean and a median Dice Similarity Coefficient (DSC) of 0.84 and 0.86, respectively. A DSC of 1 indicates perfect segmentation [91].

On the other hand, Klein et al. [92] have presented an atlas-based approach. To account for the large anatomical variability between subjects etc., they propose a multi-atlas based segmentation of the prostate. The method employs a set of prelabelled atlases, each of which is non-rigidly registered to the target image. The labels of the deformed atlas are then fused to obtain a single segmentation of the target image. Prior to the label fusion, atlas selection based on image similarities is conducted to improve the segmentation result. In this way, only atlases that best match the target image are included. Klein et al. achieve a median DSC of

0.85, and similar results have been obtained in another study by Korsager et al., who achieved a mean DCS 0.86 [93]. Korsager et al. combined a spatial prior based on inter-subject atlas registration with organ-specific intensity information in a graph cut segmentation framework.

In this project, the aim is to localise possible prostate cancer, and thus for the prostate segmentation an already tested method is applied; The prostate is segmented from the T2W images using an approach of multi-atlas registration.

7.2 Multi-Atlas Segmentation of the Prostate

This section describes the details of the atlas-based prostate segmentation utilised in the work here presented. Label propagation is a fast and easy way of atlas-based segmentation [94]. After registration of the atlas to the target image, the labels are propagated from atlas to target, and in this way the structure of interest is segmented. As the use of a single atlas does not necessarily accommodate for potential anatomical variability in the atlas or the target image, the performance of this segmentation approach is particularly dependent on the registration. For this reason, the method of multi-label propagation instead employs a library of atlases, and from this library N atlases are found that best match the input image [92]. This selection of atlases is determined based on similarity metrics. Provided the N optimal atlases, the propagated labels from each of them are fused using voting rules. The following outlines the specific procedure for the prostate segmentation in this project using such multi-atlas approach.

The multi-atlas consists of a probability map created from multiple pairwise registrations of atlas images to target image. Each voxel in the probability map contains the probability that the corresponding voxel in the target image is a prostate tissue voxel. The pairwise registrations of the atlas images to the target image are performed in multi-resolution in three stages using the registration tool Elastix [95]. The registration metric is the normalised mutual information. At the first stage an initial registration is obtained from aligning the centres of mass. The second and third stages are an affine registration and a non-rigid registration. Following the three registration stages, a subject-specific probability map $p_s(f_m)$ is constructed by averaging the resultant atlas labels:

$$p_s(f_m) = \frac{1}{N} \sum_{t_j \in \tau} g_m^{t_j} \tag{7.1}$$

N denotes the number of images in the atlas set τ, g_m represents the atlas label at voxel location m of the atlas image t_j, which has been registered to the target image found by interpolation in the registered atlas image.

As earlier stated, large differences in the anatomical format of the prostate between subjects exist, hence to improve the segmentation only the set of atlases that best match the target image is used [96]. This set of atlases is selected by comparing the normalised mutual information values and include only those having a value within a threshold of 98% of the maximum normalised mutual information value between an atlas and target image. To ensure the variability that multiple atlases bring, a minimum of 10 atlases are included, and if less than 10 atlases meet the normalised mutual information threshold, then the 10 atlases with the largest similarity to the target image are included.

The main purpose of the prostate segmentation in this project is to address the localisation of prostate cancer, and for this it is of most importance to ensure that the entire prostate is within the segmented region. However, Korsager et al. [93] observed a tendency for the multi-atlas approach to under-segment the prostate. To cope with this shortcoming, the prostate mask obtained from the multi-atlas segmentation is dilated by up to 5 voxels (2.5 mm) in all directions when used in the further analysis of the prostate cancer localisation. The extent of dilation required is assessed by visual inspection of the prostate segmentation. The result from the multi-atlas prostate segmentation for one subject is shown in Figure 7.1.

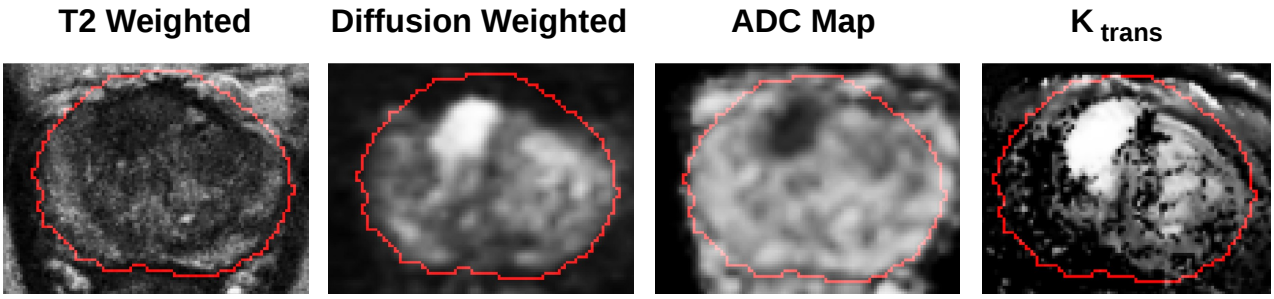

Figure 7.1: T2W image, DW image, ADC map, and K_{trans} map imposed with the segmented prostate mask (red).

Chapter 8

Voxel Classification

This chapter presents the method used in this project for classification of each voxel based on its local image properties into cancer candidate voxels, i.e. tissue possibly suspicious for cancer, or normal tissue voxels. For this classification, it is desired to have each voxel in the image volume represented by a vector of intensity and texture features. The actual classification is performed by unsupervised learning, an approach which deals with the problem of identification of hidden structures in unlabelled data. Hidden structures in terms of local properties in the images are found by applying fuzzy c-means (FCM) clustering to voxel feature vectors composed of intensity and texture features. The entire approach for the identification of cancer candidate voxels is outlined in Figure 8.1.

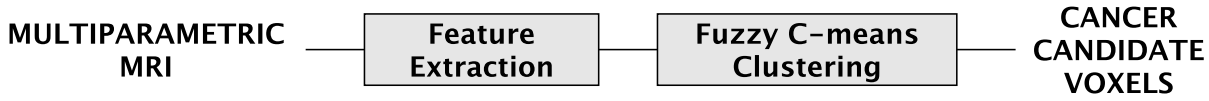

Figure 8.1: Outline of the approach for identification of cancer candidate voxels.

The extraction of intensity features from the images is described in Section 8.1, and the extraction of texture features from the images is described in Section 8.2. A presentation of the classification by FCM clustering of voxels based on the intensity and texture features is given in Section 8.3.

8.1 Intensity Analysis of Prostate Tissue

According to the clinical guidelines presented by European Society of Urogenital Radiology [25], Hoeks et al. [8], and Dickinson et al. [97], a prostate tumour can be located in multiparametric MRI data by identifying the image locations being hypointense in its T2W image and ADC map, while simultaneously appearing hyperintense in its DW image and K_{trans} map. This was summed up in Table 6.1. Intuitively, a search for voxels complying with these conditions, would be obvious cancer candidate voxels.

For each voxel location within the prostate mask, intensity information is extracted from each of the different types of images in the multiparametric MRI data, that is T2W and DW intensities and ADC and K_{trans} values.

8.2 Texture Analysis of Prostate Tissue

Cancer lesions tend to have a low variation in their image intensity distribution compared to surrounding healthy tissue in T2W images [98, 99]. This suggests that methods utilising texture information from the images could be appropriate for the differentiation of cancerous tissue from normal tissue. Texture analysis is about how mosaics of different intensities are interpreted and is a useful way of extracting information from medical images [100]. In images, texture refers to the appearance, structure, and arrangement of parts in an image. Humans easily interpret texture as being either fine or coarse, smooth or irregular, homogeneous or inhomogeneous. However, in order to translate these interpretations to a mathematical language which enables computerised analysis, the texture features need to be described by mathematical parameters computed from the fraction or distribution of pixels or voxels in the given image region [101].

More studies have succeeded in differentiating cancerous tissue from normal tissue based on texture analysis [99]. Especially in the fields of breast cancer diagnosis from mammography and characterisation of brain tumours from brain MRI, texture analysis have proved useful [102, 103, 104], but also in the field of prostate cancer diagnosis, the employment of texture analysis have obtained promising results [105]. The above studies all support the existence of texture features able to differentiate cancer tissue from normal tissue.

T2W images describe the anatomy of the prostate, and differences in textures are expected to be specially pronounced for these images [106]. Furthermore, in the field of breast cancer, Gong and Brady [107] have proposed segmentation of suspicious image areas in mammograms based on texture features extracted from DCE-MR images. In their work the image patterns in the mammograms for different types of tissue were learnt by means of a set of training data though. Nonetheless, the idea of utilising texture information from DCE-MRI in terms of K_{trans} maps could prove useful in the voxel classification of prostate voxels as well. Altogether, texture information from both T2W images and K_{trans} maps is extracted and utilised in the voxel classification.

Generally four classes of texture analysis exist, and their differences are basically found in the approach of evaluating the pixel information [100, 108]. Structural methods use well-defined primitives in the texture description. Model-based methods use a mathematical model such as fractals to describe a certain texture. Statistical methods represent the texture of an image region by analysis of the distribution and relationships of image intensities or grey-level values within this region. Finally, transform methods describe the texture of an image in a separate transformation domain or space.

Statistical methods are the most widely used approach for texture analysis of medical images [100]. Statistical parameters are subtracted from subregions of the images, and differences in these parameters are used in the differentiation of regions of different textures. Mohanty et al. [102] have subtracted statistical parameters from grey-level run-length matrices (GLRLM) for the differentiation of benign and malign breast tissue from mammography. Furthermore, they also computed grey-level co-occurrence matrices (GLCM), and from these another set of features, the so-called Haralick features, were extracted and used in the differentiation of malign and benign breast tissues. By means of the features from the GLRLMs and GLCMs, Mohanty et al. obtained a classification accuracy of 94%. The Haralick features were also utilised by Madabhushi et al. [105], who detected prostate tumours in *ex vivo* prostate MRI but mainly obtained poor results, and by Viswanath et al. [109], who computed more than

350 texture features at every spatial location and then represented these in a space of lower dimensions. They obtained a sensitivity of 92.65% and a specificity of 82.06%; however, they used 1.5 T endorectal MRI, whereas Mohanty et al. and Madabhushi et al. used a body coil and furthermore, Viswanath et al. did not have a ground truth available for all image slices. Radhakrishnan and Kuttiannan [110] have used features from GLRLMs and GLCMs both individually and together for the segmentation of prostate cancer from TRUS images. They obtained the best performance in terms of sensitivity and specificity by the combined approach.

To maximize the separability of cancer candidate voxels and voxels of normal prostate tissue, the texture analysis algorithm should result in a texture measure with two highly different values for the two types of regions. Motivated by the results obtained in the above mentioned studies, the set of texture features used in the work here presented are composed of different types of texture features extracted from both GLRLMs and GLCMs derived from T2W images and K_{trans} maps. These matrices, the features, and their deviation are described in the following sections.

8.2.1 Second Order Statistical Texture Features

First order statistics of an image provides information related to the distribution of grey-level intensities in an image, but no information about the relative positions of the various grey-level intensities within the image is provided [111, 112]. Second order statistics provides such information by measuring, among other factors, whether the high intensity voxels are positioned closely together or are spread out, intermixed with low intensity voxels.

Haralick et al. were the first to propose the use of second order texture features for the characterisation of image texture [112]. In 1975, they made the assumption that all texture information is contained in the GLCMs computed from an image, and hence the statistics computed from the GLCMs is directly related to the original image. Ever since then the use of features extracted from GLCMs has gained increasing acceptance for the task of image segmentation, and the task of cancer segmentation is no exception. As will be elaborated in the following section, the GLCM contains information of pairs of voxels, and hence the features extracted from a GLCM are second order statistics. The GLCM is defined as a $n \times n$ matrix, where n represents the number of levels in the intensity resolution of the image.

The computation of the GLCM and some features extractable from this matrix are unfolded in the following sections.

Grey-Level Co-Occurence Matrix (GLCM)

The GLCM denoted $\mathbf{P}_{\Theta,d}(I_1, I_2)$ is a matrix of relative frequencies which quantifies the occurrence of two voxels with grey-level intensities I_1 and I_2, separated by a distance d in the orientation of Θ. An account on orientations is deferred to Section 8.2.3. Figure 8.2 illustrates the computation of an example GLCM from a small example image region. As already mentioned, the dimensions of the GLCM is determined by the number n of grey-level intensities in the image. The higher number of intensity levels included in the GLCM, the higher is the

computational cost of the texture statistics, and consequently a standard procedure is to decrease the the number of levels in the intensity resolution of the image to a resolution in which just the most vital intensity information is retained. Another advantage of this decrease in intensity resolution is that the image noise can be reduced to some degree, as voxels of similar grey-level intensities are given same value in the reduced intensity resolution image.

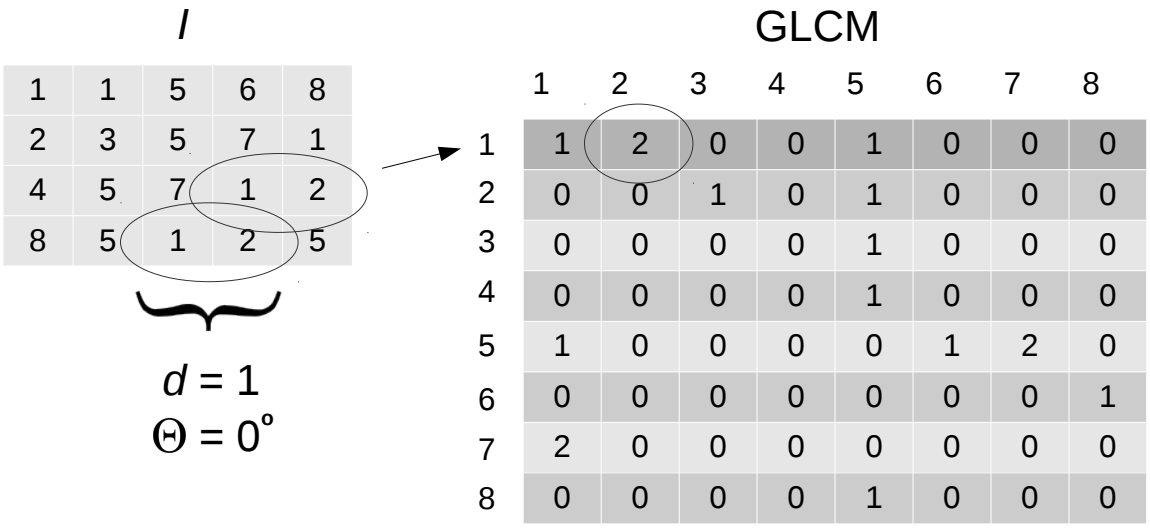

Figure 8.2: Illustration of the computation of a grey-level co-occurrence matrix (GLCM) with distance $d = 1$ and orientation $\Theta = 0°$, i.e. horisontal orientation, of the image (I). The resolution is 3 bit corresponding to 8 grey-level intensities.

Features from Grey-Level Co-Occurrence Matrices

From the GLCM potentially high discriminative features can be defined and extracted in order to obtain texture related information. The Haralick features are such examples of statistical parameters [112]. Among these are features describing respectively *Energy*, *Entropy*, *Contrast*, *Homogeneity*, *Variance*, *SumMean*, *Inertia*, *Cluster Shade*, *Cluster Tendency*, *Max Probability* and *Inverse Variance*. Together these features have been associated with a high discriminative power in the distinction of different regions in an image [111]. Descriptions of and formulas for the Haralick features can be found in Appendix A.1.

8.2.2 Higher Order Statistical Texture Features

While some studies argue that second order statistical texture features are sufficient for texture descriptions, other studies prove an improvement when including texture features of higher order [113, 114]. Where second order statistics describes the relation between intensity values of pairs of voxels, the GLRLM method is a way of extracting higher order statistical texture features [115, 116].

Grey-Level Run Length Matrices (GLRLM)

Coarse texture would often be interpreted from image parts consisting of large regions of which each is similar in intensity, whereas what is understood as fine texture is interpreted from image parts consisting solely of an intermixture of much smaller regions of similar intensity. In other words, the number of neighbouring voxels similar in intensity provides reason for a texture interpretation. This is the main idea behind the GLRLM [100, 117, 118]. A grey-level run is a set of consecutive, collinear voxels having the same grey-level intensity, and the length of the run is the number of voxels in the run. In a given orientation in the image, a search for runs of voxels of identical grey-level intensity is performed. The GLRLM then sums up the results of the search by describing the number of runs of a certain length and grey-level intensity. A coarse texture would then tend to contain more runs of larger lengths compared to a fine texture.

For a given image, the run length matrix $\mathbf{P}_\Theta$ contains the elements $P(i, j)$ representing the number of runs with voxels of grey-level intensity equal to i and length of run equal to j in a given orientation Θ [35]. The size of $\mathbf{P}_\Theta$ is given by the number of levels in the intensity resolution of the image and the maximum possible length of a run in the volume. Figure 8.3 shows an example image and the computed GLRLM for the orientation $\Theta = 0°$.

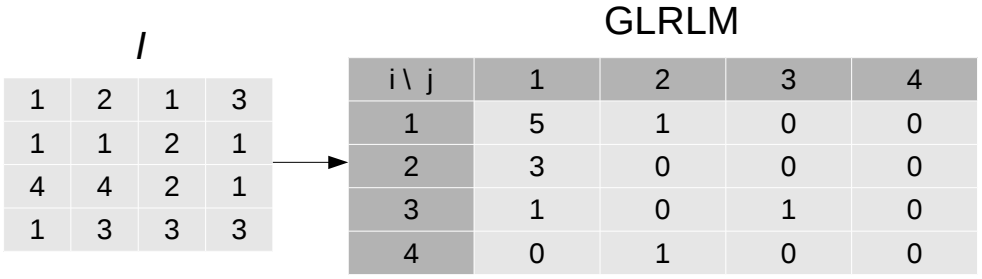

Figure 8.3: An image I and the computed grey-level run length matrix (GLRLM) for the orientation $\Theta = 0°$, , i.e. horisontal orientation.

Features from Grey-Level Run Length Matrices

To describe the texture properties of a region, several texture features can be calculated from the GLRLMs. Typically the following 11 features are extracted [35]; *Short run emphasis* (SRE), *long run emphasis* (LRE), *high grey-level run emphasis* (HGRE), *low grey-level run emphasis* (LGRE), *run-length non-uniformity* (RLNU), *grey-level non-uniformity* (GLNU), and *run percentage* (RPC), and furthermore, pair-wise combinations of the length and grey-level emphasis; *short run low grey-level emphasis* (SRLGE), *short run high grey-level emphasis* (SRHGE), *long run low grey-level emphasis* (LRLGE), *long run high grey-level emphasis* (LRHGE). These features hold information of different aspects of the image. For instance, SRE measures the occurrences of short runs in the image and is expected high for fine textures, while GLNU measures the similarity of grey-level intensities within the image and is expected large for very heterogeneous images. Descriptions of and formulas for the 11 features can be found in Appendix A.2.

8.2.3 Orientations

The statistical texture features just described can be derived from GLCMs and GLRLMs of different orientations of the image. In general, texture features can be derived from four different orientations in a 2D image, namely 0°, 45°, 90°, and 135°, as illustrated in Figure 8.4. These orientations are defined by a displacement vector $d(x, y)$, describing the displacement along the x- and y-axis. This representation can be extended to a 3D volume by letting the orientation be defined by a displacement along a third dimension as well, the z-axis. This gives a vector representation of the displacement $d(x, y, z)$ and a total of 13 possible orientations. The orientations can also be described by means of two angles, Θ describing the orientation in the x-y-plane, and Φ describing the orientation in x-z-plane, see Figure 8.4.

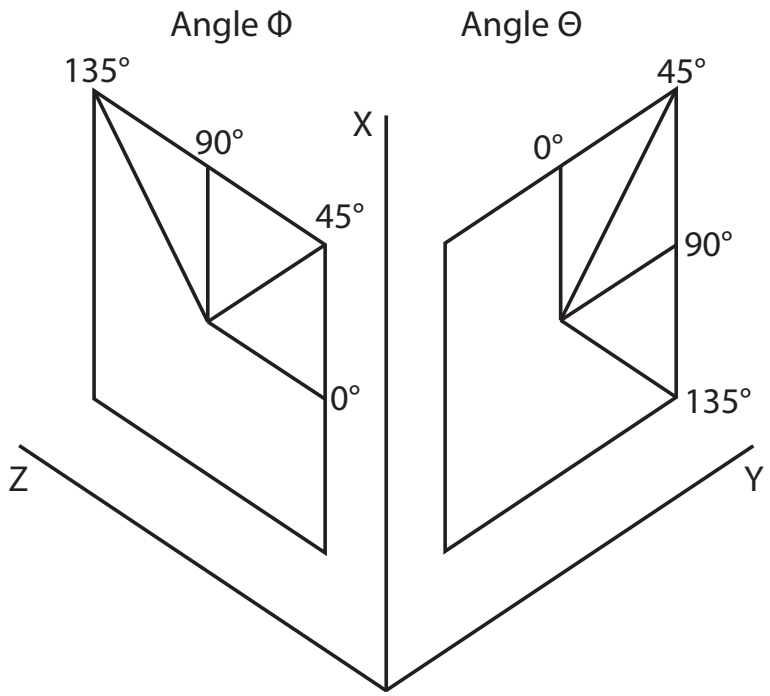

Figure 8.4: Illustration of orientations in a 2D image in the x-y-plane and in a 3D volume in the x-y-z-plane with emphasis on the angular orientation representation.

Orientations of $\Phi = 90°$ provide the orientations for a 2D image. Table 8.1 lists all 13 orientations described with angles Θ and Φ, and by the corresponding vector representation of the displacement $d(x, y, z)$.

(Θ,Φ)	$d(x, y, z)$
(0°, 90°)	(1, 0, 0)
(45°, 90°)	(1, 1, 0)
(90°, 90°)	(0, 1, 0)
(135°, 90°)	(-1, 1, 0)
(0°, 0°)	(0, 0, -1)
(0°, 45°)	(1, 0, -1)
(0°, 135°)	(1, 0, 1)
(135°, 0°)	(0,1, 1)
(45°, 0°)	(0, 1, -1)
(45°, 45°)	(1, 1, -1)
(135°, 135°)	(1, -1, 1)
(45°, 135°)	(1, 1, 1)
(135°, 45°)	(-1, 1, 1)

Table 8.1: List of orientations in a 3D volume, represented by two angles, (Θ,Φ), or by a vector representation of a displacement, $d(x, y, z)$. Freely adapted from [35].

The top nine entries in this table represent orientations along voxel edges or following diagonals on voxel sides. The bottom four entries in the table represent orientations following diagonals inside voxels. A GLCM and a GLRLM can be computed for each of the 13 orientations, resulting in 13 of each. However, it is common practice to average the matrices over all 13 orientations, resulting in a single GLCM for each distance d and a single GLRLM [101]. Subsequently, texture features can be extracted from these matrices.

8.2.4 Implementation of Texture Analysis of Prostate Tissue

In the work presented here, Haralick features extracted from GLCMs as well as features extracted from GLRLMs are utilised besides the intensity features in the voxel classification. GLCMs and GLRLMs are computed from T2W images and K_{trans} maps, and the texture features are extracted by the following procedure: From the prostate segmentations in the T2W images, GLCMs and GLRLMs are computed from kernels of $5 \times 5 \times 5$ voxels centered around each voxel in the image volume. From each of such set of matrices, the texture feature vector for corresponding center voxel in the kernel is determined.

As described in Sections 8.2.1 and 8.2.2, the size of both the GLCM and the GLRLM is dependent on the number of grey-level intensities in the image. To avoid unnecessarily large matrices, the original T2W images and K_{trans} maps were scaled to a lower intensity resolution. The resolution of the images is decreased to 4 bit (16 grey-level intensities), without loosing much information. This is illustrated in Figure 8.5 for a T2W image.

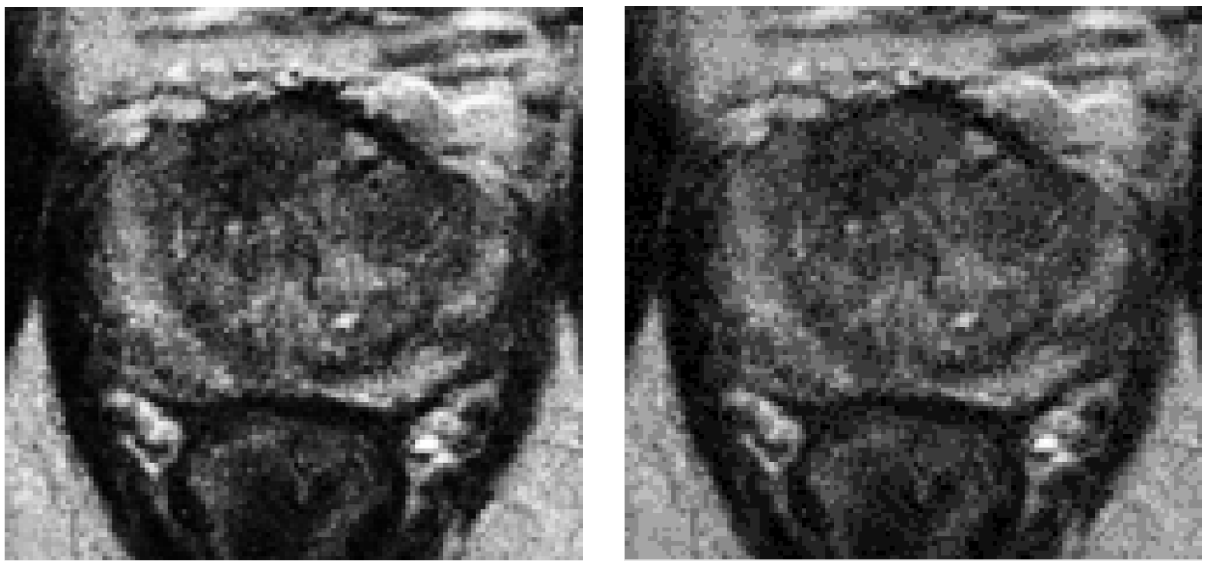

Figure 8.5: Axial T2W image of subject 1, slice 38. **Left:** Original image. **Right:** Image with intensity resolution decreased to 4 bit. Minimal loss of details is observed.

From the T2W images and K_{trans} maps both with decreased intensity resolution, GLCMs and GLRLMs were computed and the set of the 11 Haralick features and the set of the 11 features from the GLRLMs were extracted for each voxel. In order to investigate whether different distances d in the GLCM influence the classification, the features from using the four different distances d of 1-4 were tested. The results are briefly presented in the following section.

Distances in the Grey-Level Co-occurence Matrix

GLCM can be computed for both different orientations (Θ, Φ) and different distances d between the pairs of voxels. While it is common practice to use the average GLCM of all orientations, the texture features extracted from GLCMs with different distances d may differ. This is investigated in the following, where voxel classificaions using texture features extracted from GLCMs of different distances d are compared. The set of Haralick features from the following GLCMs ($\mathbf{P}_{\Theta,d}$) were extracted and compared: $\mathbf{P}_{All,1}$, $\mathbf{P}_{All,2}$, $\mathbf{P}_{All,3}$, $\mathbf{P}_{All,4}$. The subscript *All* refers to the average matrix of the 13 GLCMs with different orientations. Furthermore the collected set of Haralick features from all distances was included in the comparison as well.

For each of the sets of Haralick features, the FCM clustering using two clusters was applied, and the resulting cancer candidate voxels were compared based on a measure of the spatial overlap between the different sets. The overlap was measured by calculation of the Dice Similarity Coefficient (DSC) between the resulting sets of cancer candidate voxels. A DSC of 1 indicates a total overlap or agreement. A DSC was calculated between all the sets of Haralick features, and the mean and standard deviation of the DSC from all the DSCs was calculated to 0.9213 $\pm$ 0.0320, which indicates only small differences between the resulting sets of cancer candidate voxels.

Furthermore, the different sets of cancer candidate voxels were visually inspected. Again, only small differences between the sets of cancer candidate voxels were seen for all subjects. Figure 8.6 shows three example images from one subject.

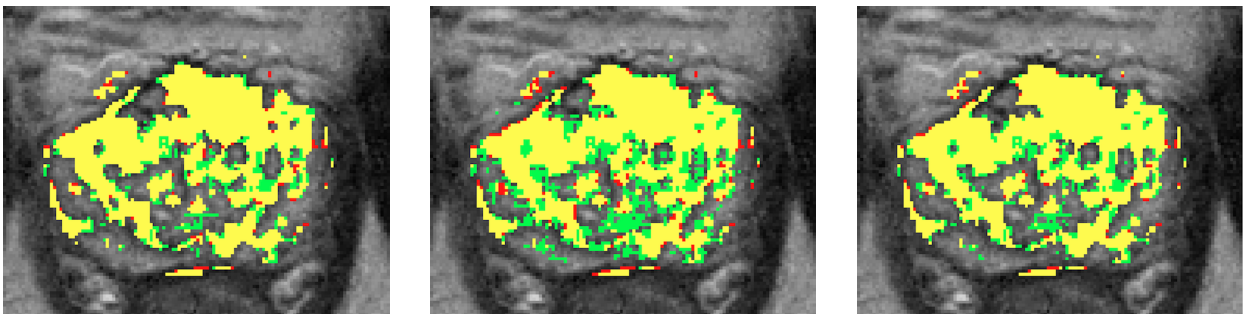

Figure 8.6: Spatial overlap between cancer candidate voxels using Haralick features extracted from GLCMs with different distances d overlaid a T2W image. Yellow indicates overlap of the sets of green and red cancer candidate voxels. **Left:** Cancer candidate voxels from classification of Haralick features using $d = 1$ (red) compared with cancer candidate voxels from classification of Haralick features using $d = 2$ (green). **Middle:** Cancer candidate voxels from classification of Haralick features using $d = 1$ (red) compared with cancer candidate voxels from classification of Haralick features using $d = 4$ (green). **Right:** Cancer candidate voxels from classification of Haralick features using $d = 1$ (red) compared with the cancer candidate voxels from classification of Haralick features using the collected set of different distances (green).

Based on both the DSCs and the visual inspection, only Haralick features extracted from the GLCM $\mathbf{P}_{All,1}$ were used together with both the intensity features as well as the set of features from the GLRLMs in the further processing.

8.3 Fuzzy C-means Clustering of Prostate Tissue

The feature vectors consist of four intensity features, including intensities in T2W images, DW images, ADC maps and K_{trans} maps, and 44 texture features, including a set of 11 Haralick features and 11 features from the GLRLM from both T2W images and K_{trans} maps. The feature vectors are used in the classification of the prostate voxels.

Chen et al. [119] separated breast tumours from normal breast tissue by means of a fuzzy c-means (FCM) clustering algorithm. This algorithm could possibly be used in the voxel classification as well. Clustering is the task of assigning data to certain classes or clusters, such that objects in the same cluster are more similar to each other than to those in other clusters according to a chosen similarity metric [120]. In hard clustering, an object belongs to exactly one cluster, whereas in fuzzy clustering, objects can belong to more than a single cluster. In fuzzy clustering certain membership grades indicate the degree to which the objects can be associated to the different clusters.

In FCM clustering, initial cluster centres are basically guessed upon, however, the algorithm iteratively updates the cluster centres and thus the membership grades for each data point are updated as well. At convergence, when the locations of the cluster centres change no more from iteration to iteration, the cluster centres will be located at the right locations within the data set. The iterations are driven by the minimisation of an objective function of the distance from any data point to the cluster centres weighted by the associated membership grades for the point:

$$J_{fuz} = \sum_{i=1}^{c}\sum_{j=1}^{n}[\hat{P}(\omega_i|\mathbf{x}_j, \hat{\Theta})]^b||\mathbf{x}_j - \mu_i||^2 \tag{8.1}$$

c and n are the number of clusters and number of data points, respectively, $\mathbf{x}_j$ is a data point, $\hat{P}(\omega_i|\mathbf{x}_j, \hat{\Theta})$ is the membership grade for data point $\mathbf{x}_j$ with respect to cluster ω_i, $\hat{\Theta}$ is a parameter vector for the membership function, μ_i is the data point at the center of cluster ω_i, and b controls the blending of the different clusters. Letting $b = 1$ produces a hard clustering, and letting $b > 1$ allows each data point to belong to multiple clusters. Thus, all data points are assigned into clusters based on minimising the distance between the data points.

A feature plot composed of the different features is constructed. The purpose of the FCM clustering is to divide the point cloud of the feature plot into appropriate clusters. The classification using FCM clustering is based on a preset number c of clusters. The Euclidean distance is used as the similarity metric, and each data point is assigned to the cluster to which it has the highest membership grade. The value of c must be chosen as a compromise of including every cancer candidate voxel into the clusters for cancer candidate voxels and excluding as many voxels not being cancer candidate voxels as possible from such clusters.

With the prostate tissue in mind cf. Table 6.1, the number of natural clusters could be two, i.e. $c = 2$ corresponding to cancerous tissue and normal tissue. Furthermore, it is of utmost importance that all voxels representing true cancer are classified as cancer candidate voxels, and the generation of false positives is of less importance, as these possibly will be discarded in the identification of cancer regions as presented in Chapter 9. Figure 8.7 shows the results of voxel classification by FCM clustering of voxels of prostate tissue on the basis of features of intensity and texture for subject 1, with the cancer candidates voxels in green overlaid a T2W image.

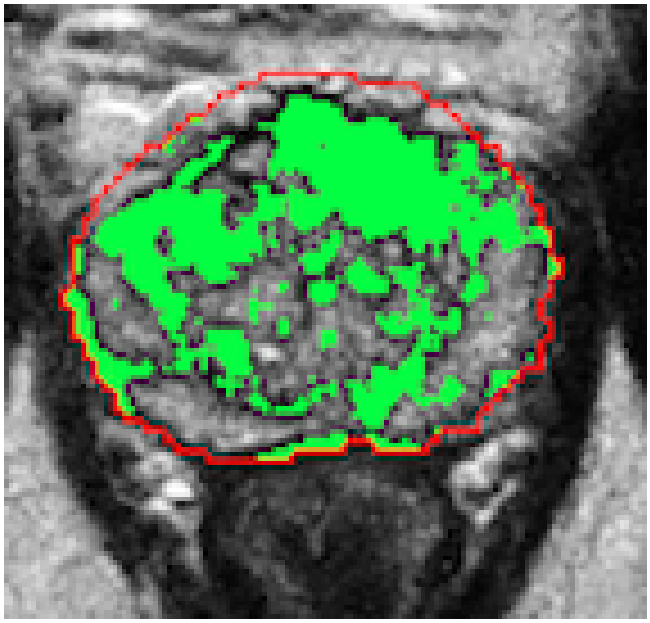

Figure 8.7: Cancer candidate voxels (green) and prostate boundary mask(red) for subject 1 overlaid T2W images, slice 38.

8.4 Summary of Voxel Classification

In the voxel classification in the framework for automated prostate cancer localisation presented here, a total of 48 features were extracted and utilised in the classification of each voxel. Each voxel represents a location in each type of MR images in the multiparametric MRI data, and the 48 features compose the grey-level intensity of a specific voxel location in the T2W image, DW image, ADC map, and K_{trans} maps, as well as 44 texture features extracted from the T2W images and K_{trans} maps, including homogeneity and grey-level non-uniformity amongst others. The prostate tissue was then classified into cancer candidate voxels and voxels representing normal prostate tissue by means of FCM clustering. The cancer candidate voxels compose the basis for the identification of cancer regions. This is described in more detail in Chapter 9.

Chapter 9

Identification of Cancer Regions

To localise a tumour within the prostate, the next step in the framework of automated prostate cancer localisation is to segment the set of cancer candidate voxels into cancer regions and regions representing normal tissue in the DW images, ADC maps, and K_{trans} maps. This is conducted in a three stage method. In the first stage regions are segmented using one of two methods, Laplacian of Gaussian (LoG) edge detection and watershed transform, and in the second stage, the segmented regions are classified into cancer regions and regions representing normal tissue by FCM clustering, as presented in Section 8.3. The FCM clustering is based on a feature extracted from each segmented region, its mean grey-level intensity. Finally, in the third stage, to ensure the localised tumour fulfils the assumptions of cancer appearance for both DW images, ADC maps, and K_{trans} maps, as stated in Table 6.1, only cancer regions identified in all three types of MR images at same image location are considered tumours.

The total procedure of identification of cancer regions from the set of cancer candidate voxels is outlined in Figure 9.1.

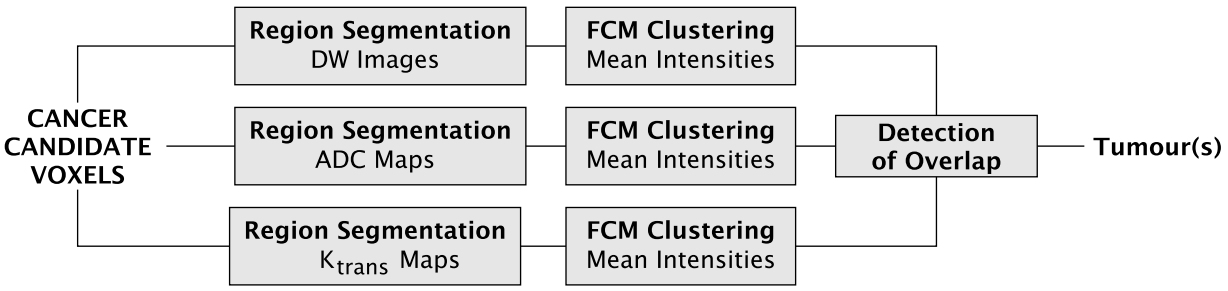

Figure 9.1: Outline of the approach for identification of cancer regions.

In Section 9.1 the two methods for region segmentation, LoG edge detection and watershed transform, are described, and in section 9.2 the classification of the segmented regions into cancer regions or regions of normal tissue is described.

9.1 Region Segmentation

Two methods, LoG edge detection and watershed transform, are proposed for the region segmentation of the set of cancer candidate voxels. LoG edge detection is presented in Section 9.1.1, and watershed transform is presented in Section 9.1.2. Both sections start with a theoretical outline of each method and end with a pretest of applying each method to image data

from three subjects.

9.1.1 Laplacian of Gaussian Edge Detection

In image analysis, edge detection is a method to find points or lines in an image at which locations there is a strong abrupt or rapid change in the image intensities. Since prostate cancer manifests in an intensity range different from that of normal prostate tissue in the DW images, ADC maps, and K_{trans} maps, edge detection can be used to distinguish possible cancer regions from non-cancer regions in these types of images. Also in the T2W images edge detection can indicate regions suspicious for cancer, since cancer also in T2W images manifests as hypointense regions, however, numerous physiological conditions can cause similar hypointense regions in these images. In addition, by studying the T2W images, the seemingly higher grey-level intensity resolution in these images challenges the task of separating regions of different intensities, while this seems easier for the images from remaining MRI techniques, as they seem to have more connected regions of either low or high grey-level intensities. This means that applying edge detection to the T2W images could result in detection of false edges separating cancerous and healthy prostate tissues leading to misclassification of image regions. Thus in this work the edge detection based method only utilises the information from DW images, ADC maps, and K_{trans} maps.

As described in Section 3.3 and summed up in Table 6.1, cancer tissue appears as high intensities in both DW images and K_{trans} maps and as low intensities in ADC maps, and therefore the removal of all the dark regions in the DW images and K_{trans} maps and all the bright regions in the ADC maps could result in an identification of cancer regions. Using an edge detector such as LoG edge detection, edges separating low intensity and high intensity regions in both the DW images, ADC maps, and K_{trans} maps can be found, segmenting the images into regions.

As a preprocessing step to many edge detection algorithms, a filtering procedure is often applied to remove noise in the image. As the name indicates, the LoG edge detection uses a Gaussian smoothing by convolution of the image with a Gaussian kernel of size n_{LoG}; that is, in the 1D case, the kernel size is n_{LoG}, in the 2D case kernel size is $n_{LoG} \times n_{LoG}$ and for the 3D case, the kernel size is $n_{LoG} \times n_{LoG} \times n_{LoG}$. In 1D, the Gaussian kernel has an impulse response, expressed with the standard deviation σ as a parameter, as:

$$g(x) = \frac{1}{\sqrt{2\pi} \cdot \sigma} \cdot e^{\frac{-x^2}{2\sigma^2}} \tag{9.1}$$

In 3D, the impulse response is simply the product of three Gaussians, corresponding to one per direction:

$$g(x, y, z) = \frac{1}{(2\pi)^{3/2}\sigma^3} \cdot e^{\frac{-(x^2+y^2+z^2)}{2\sigma^2}} \tag{9.2}$$

The standard deviation σ can be varied to give different scale-space representations of the smoothed image. In the applied implementation, σ is controlled by the kernel size n_{LoG} of the filter, such as:

$$\sigma = \frac{n_{LoG}}{4\sqrt{2\log 2}} \tag{9.3}$$

Where n_{LoG} as mentioned is the size of the Gaussian kernel, isotropic in all three directions. Increasing σ by increase in the kernel size will produce a more smooth image, which, in the end, influences the edges found. From the smoothed image the Laplacian operator ΔI is calculated, which is the divergence of the gradient of intensity values in the smoothed image. That is, ΔI is the sum of second partial derivatives of intensity values in the image with respect to each direction:

$$\Delta I = \frac{\partial^2 I}{\partial x^2} + \frac{\partial^2 I}{\partial y^2} + \frac{\partial^2 I}{\partial z^2} \tag{9.4}$$

The Laplacian operator ΔI calculated at each voxel in the smoothed image produces the final filtered image, in which dark regions will have positive values and bright regions will have negative values. From this image, edges can be found between the dark and bright regions by identifying all zero-crossings. In other words, an edge is indicated when the image signal goes from a negative to a positive value and vice versa, thus every time the signal crosses zero in a scan across the image.

Pretest of Method and Determination of Optimal Kernel Size

In order to achieve an useful region segmentation, the edge detection should result in detection of real edges in the images. Prior to the edge detection, the image is filtered using a LoG filter. The impact of this filter is controlled by the size of its kernel, n_{LoG}. If n_{LoG} is too small, the image most likely gets over-segmented, but on the other hand, if n_{LoG} is too large, important information on the actual edges within the image may disappear. Thus, the task is to choose a size n_{LoG}, well in between these conditions. Four different kernel sizes, $n_{LoG} = 3$, $n_{LoG} = 5$, $n_{LoG} = 7$, and $n_{LoG} = 9$ were tested in both DW images, ADC maps, and K_{trans} maps. The region segmentation results were evaluated qualitatively, where the success criterion was good detection and localisation of real edges in the images, meaning the edges detected should mark a good distinction between low and high intensity regions at the correct location.

The use of $n_{LoG} = 3$ giving the lowest standard deviation by Equation 9.3 and therefore producing the finest edges showed a tendency to divide the images into many small and undefined regions, resulting in an over-segmentation as seen in Figure 9.2 to the left. For $n_{LoG} = 5$, the different regions seemed more meaningfully connected and forming larger regions of low or high intensities. Use of $n_{LoG} = 7$ produced smoother edges while still providing a good distinction between low and high intensity regions. This tendency was seen for both the DW images, ADC maps, and K_{trans} maps. Finally $n_{LoG} = 9$ tended to mark the edges at locations favouring the high intensity regions, while the regions of lower intensities each contained a broader range of intensities. This could be desirable for the DW images, where lower intensity regions indicate normal tissue typically covering a range of intensity values, while unfortunate for the ADC maps, where low intensity regions indicate cancerous tissue typically rather homogeneous in intensity value; a broader range of intensity values in the low intensity regions therefore here indicates inclusion of normal tissue in the detected possibly cancerous regions. However, when using $n_{LoG} = 9$, some high intensity regions in the DW images tended to be too large, i.e.

being heterogeneous in intensities. Some of these tendencies were seen for the K_{trans} maps when using $n_{LoG} = 9$ as well.

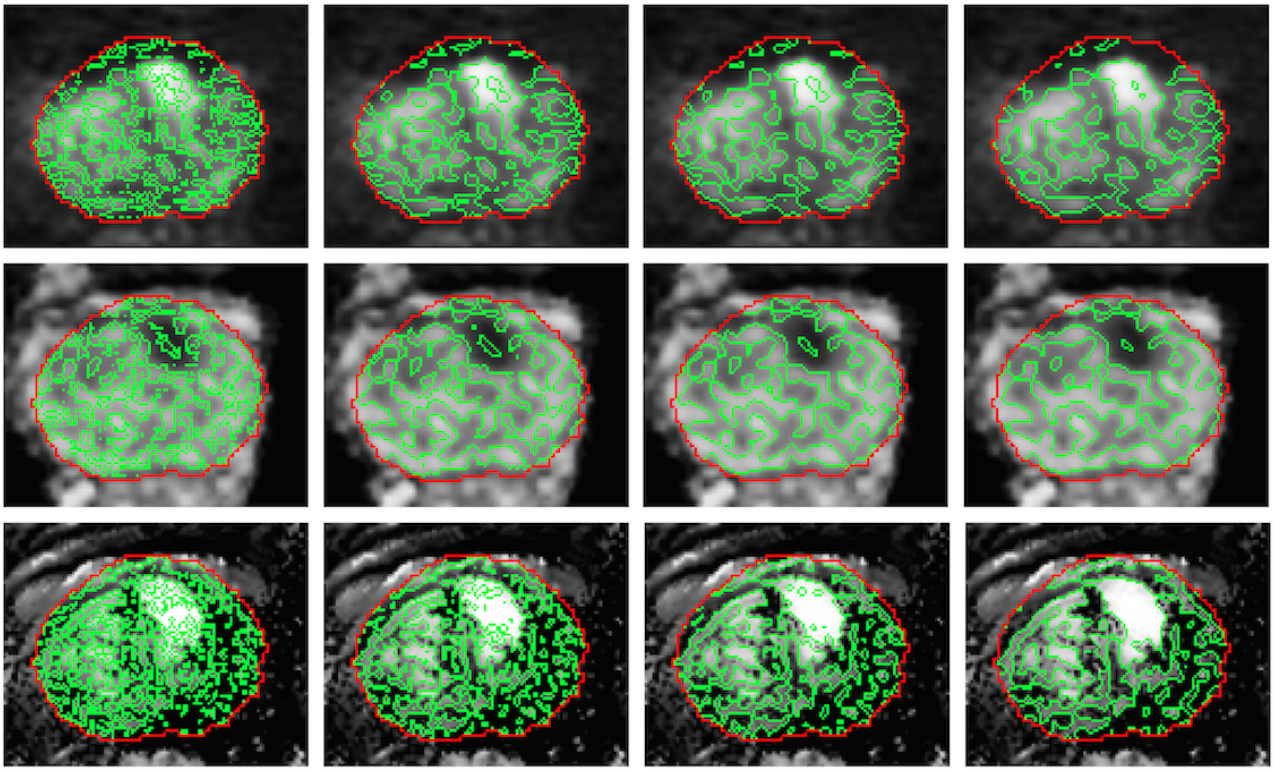

Figure 9.2: Resultant edges from the test of kernel size n_{LoG}. Prostate boundary (red) and edges (green) overlaid the original images for subject 1, slice 38. From **Left** to **Right**: n_{LoG} =3, n_{LoG} = 5, n_{LoG} =7, and n_{LoG} = 9. **Top:** Edges in DW image. **Middle:** Edges in ADC map. **Bottom:** Edges in K_{trans} map.

Based on the visual inspection, a kernel size of $n_{LoG} = 7$ was chosen for the filtering of both DW images, ADC maps, and K_{trans} maps for the application of LoG edge detection in this work.

9.1.2 Watershed Transform

The watershed transform is a region-based image segmentation method, that partitions the image into homogeneous regions. In the literature, the watershed transform has been used to segment images of tumours or lesions in other organs than the prostate. Huang and Chen [121] have used a watershed transform along with a trained classifier to find the contours of breast tumours from sonography. They achieved a precision of 81.80% and an agreement with reference of 94.66%. Cui et al. [122] also applied the watershed transform for breast tumour segmentation but in contrast-enhanced MR images. When compared to two manual segmentations, they achieved agreements of 62.6% ± 9.1% and 61% ± 11.3%. Furthermore, the agreement between the manual segmentations themselves was only 64.3% ± 10.4%, and thus the watershed-based segmentation performed almost as well. These promising results motivate the use of the watershed transform in the identification of cancer regions in this project.

The watershed transform takes advantage of the gradients of the intensity values in the images, when identifying cancer regions from the set of cancer candidate voxels. The magnitudes of the image gradients are used to compute a topographic reconstruction of the images. Large gradients now become steep climbings, and small gradients compose plateaus or flat regions. In both DW images and K_{trans} maps, local maxima will represent regions suspicious of cancer, whereas in ADC maps, local minima will represent regions suspicious of cancer. With this in mind, imagine that each regional minimum in the gradient images is punched and the topographic reconstruction is slowly flooded with water. When the rising water in one distinct catchment basin is about to merge with the water in an adjacent basin, a dam or watershed ridge is constructed to prevent this merging. This process of flooding and watershed ridge construction continues until all basins are completely filled with water. This process is termed the watershed transformation, and when imposing the watershed ridges from the gradient images onto the original images, the original images are divided into basins or regions rather homogeneous in intensities the contour of which follows the locations of locally steepest intensity changes.

Basically, the watershed transform works by classifying all image points into one of the following three classes [123]: **1**) Points belonging to a regional minimum. **2**) Points at which a drop of water if placed here would definitely flow into a single regional minimum and finally, **3**) Points at which the drop of water would be equally likely to fall into two or more of such regional minima. In this way, the gradient information is utilised to form watershed ridges which separate regions of different intensity information or regions of similar intensity information where in between a borderline exists of different intensity information in the original image.

The watershed transform can proceed as follows [123]: Firstly, let $f(x, y)$ denote a gradient image with h_{min} and h_{max} as minimum and maximum intensity values. The flooding of the topographic reconstruction can be defined as a recursion with the grey-level h increasing discretely from h_{min} to h_{max}. Using the recursion, regions around each regional minimum of f are successively expanded from initially containing just the points belonging to the minimum. Let $T[h]$ represent the set of coordinates (s, t) which has the grey-level intensity $g(s, t)$ lower than indicated by h:

$$T[h] = (s, t)|g(s, t) < h \tag{9.5}$$

Secondly, let $M_1, M_2, ..M_R$ denote sets of coordinates of points in the regional minima of $f(x, y)$, and let $C_h(M_i)$ denote the set of coordinates of points in the catchment basin associated with minimum M_i and recursion h. Now $C_h(M_i)$ can be viewed as forming a binary image with value one at points belonging to $C_h(M_i)$ and zero elsewhere, offering an insight into the procedure of the watershed transform:

$$C_h(M_i) = C(M_i) \cap T[h] \tag{9.6}$$

$C_h(M_i)$ is the final version of $C_h(M_i)$, that is when all basins are completely filled with water; $C(M_i) = C_h(M_i)$ for $h = h_{max}$. In this way, the portion of the gradient image in $T[h]$ associated with the regional minimum M_i at stage h of the recursion gets isolated. At this stage, some catchment basins will be flooded, and the union of the flooded part of those are now denoted

by $C[h]$:

$$C[h] = \bigcup_{i=1}^{R} C_h(M_i) \tag{9.7}$$

During the recursion, the number of elements in $C_h(M_i)$ and $T[h]$ either remains the same or increases from turn to turn. From this it follows that $C[h-1]$ is a subset of $C[h]$. In addition, from Equations 9.6 and 9.7, $C[h]$ is a subset of $T[h]$ and then $C[h-1]$ is also a subset of $T[h]$. This gives the property that each connected component of $C[h-1]$ is also a connected component in $T[h]$. In other words, the segmentation boundaries are connected paths.

Due to the image resolution, the grey-level intensities in the DW images, ADC maps, and K_{trans} maps can vary to a great extent, producing lots of regional minima in their gradient images. Each regional minimum, including little, insignificant minima, will form its own catchment basin, and as a consequence, the watershed transform is very likely to over-segment the images. That is, the image is divided into many small regions, and regions very similar in intensity are divided. Many strategies to prevent over-segmentation exist [124]. In this project, the gradient images are smoothed using morphological operations. In this way, the amount of little and insignificant grey-level variations is reduced. The morphological operations performed consists of an opening followed by a closing using a square structuring element of size $n_w \times n_w$. Increasing the size of n_w will give a more smooth image. Once the image is smoothed the watershed transform is applied to segment the image into dark and bright regions.

Pretest of Method and Determination of Optimal Size of Structuring Element

In order to achieve an useful region segmentation, the catchment basins and watershed ridges produced by the watershed transform result in segmentation of homogeneous regions in the images. Prior to the application of the watershed transform, the image is smoothed. The size, $n_w \times n_w$, of the structuring element, applied for this purpose, controls the degree of the smoothing. If n_w is too small, the image most likely gets over-segmented, but on the other hand, if n_w is too large, important information on the gradients might disappear. Thus, the task is to choose a size n_w, well in between these conditions. To investigate whether a smoothing of the gradient image influences the segmentation results at all, the watershed transform was first applied to images with no smoothing, i.e. $n_w = 0$. Subsequently, the watershed transform was applied to images smoothed using a structuring element with $n_w = 3$ and $n_w = 5$. The region segmentation results were evaluated qualitatively by visual inspection with the success criterion being formation of ridges providing a good division of low and high intensity regions, and furthermore that the intensity content of each catchment basin or region is homogeneous.

- $n_w = 0$, i.e. no smoothing of the gradient image the watershed transform produced, as expected, an over-segmentation. This tendency is seen in Figure 9.3 to the left both for DW images, ADC maps, and K_{trans} maps. The intensity content of the image is correctly divided into regions homogeneous in intensity, however neighbouring regions are very similar in intensity.
- $n_w = 3$ produced acceptable results with homogeneous regions distinct in intensity from neighbouring regions.
- $n_w = 5$ tended to produce larger regions with some degree of heterogeneity in the intensities within most regions, that is, some of the low intensity regions also contained voxels of higher intensity, and the opposite was seen for regions mainly high in intensity.

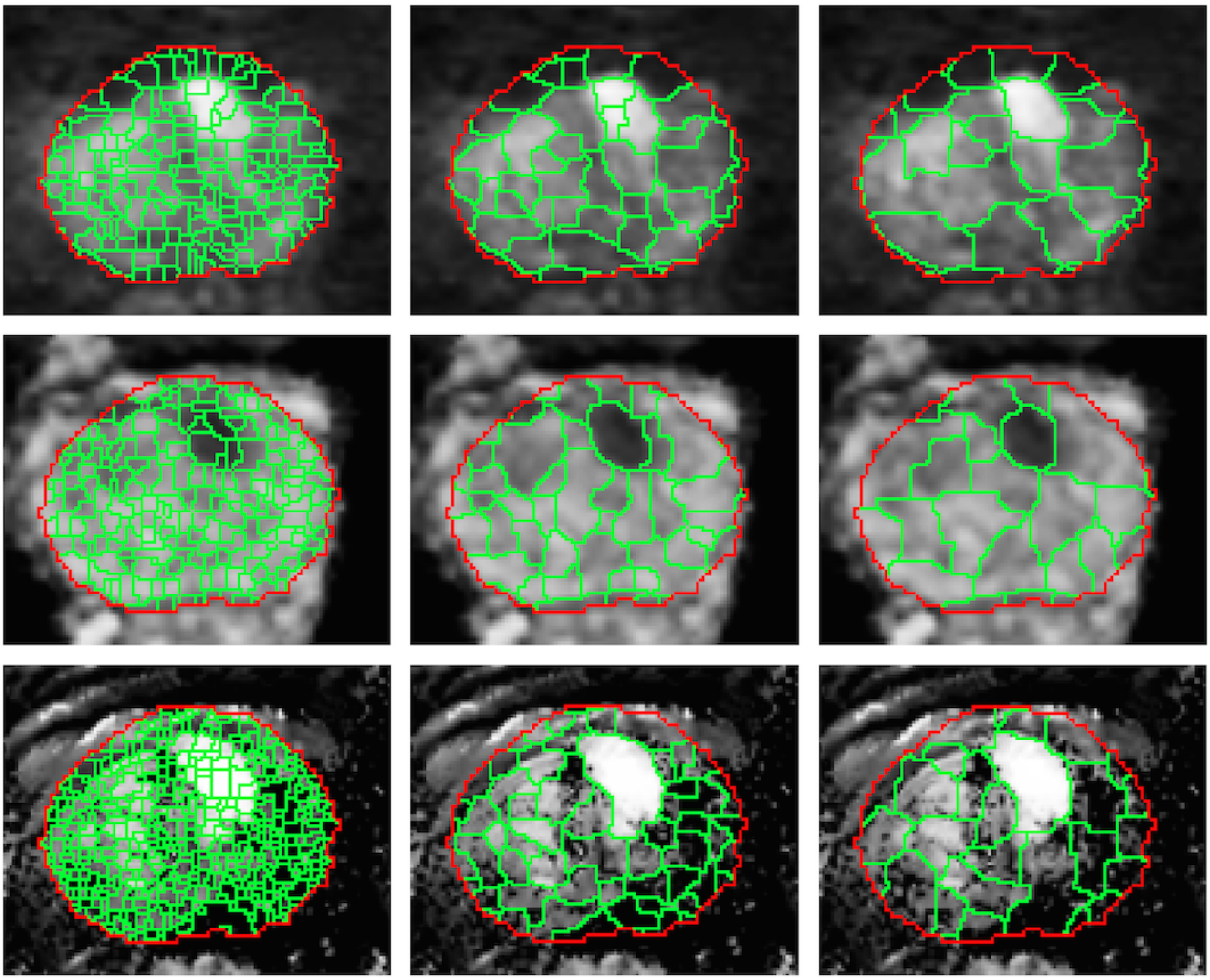

Figure 9.3: Results from applying the watershed transform to gradient images smoothed using different sizes $n_w \times n_w$ of the structuring element: Prostate boundary (red) and ridges found (green) overlaid the original images for subject 1, slice 38. From **left** to **right**: $n_w = 0$, $n_w = 3$, and $n_w = 5$. **Top:** DW image. **Middle:** ADC map. **Bottom:** K_{trans} map.

To ensure that the watershed transform produces a good distinction between low intensity and high intensity regions, both $n_w = 0$ or $n_w = 3$ could be appropriate. However, larger catchment basins will produce a better basis for the following FCM clustering step, and thus $n_w = 3$ was chosen for the smoothing of the gradient images computed from DW images, ADC maps, and K_{trans} maps prior to the application of watershed transform.

9.2 Region Classification

By means of LoG edge detection or watershed transform the set of cancer candidate voxels is segmented into image regions. In order to classify these regions into cancer regions or regions representing normal prostate tissue, the mean grey-level intensity for each region is calculated and utilised as a feature for the specific region. The actual classification of the regions is conducted by application of FCM clustering to the mean grey-level intensities for the regions

segmented. This is conducted individually for the segmented regions in the different types of MR images. The classification using FCM clustering is based on a preset number c of clusters cf. Section 8.3. To determine the optimal number of clusters c to include every region suspicious of cancer in the cluster herefore and exclude as many regions as possible not suspicious of cancer from this cluster, a test is conducted and its results are presented in Section 9.2.1.

For the DW images and K_{trans} maps, the regions from the cluster with the highest centre location corresponding to the most hyperintense regions, are classified as cancer regions. For the ADC maps, the regions from the cluster with the lowest centre location corresponding to the most hypointense regions, are classified as cancer regions. The regions classified as cancer regions are dilated to ensure that all tissue suspicious for cancer is contained, and if a cancer region appears to have a hole inside itself, this hole is filled based on the assumption that a tumour is compact. The regions classified as normal prostate tissue are discarded.

When the cancer regions have been identified individually within the DW images, ADC maps, and K_{trans} maps, the spatial agreements or overlaps of their respective cancer regions are computed and contribute to the actual tumour localisation. This principle is illustrated in Figure 9.4 in which it is shown how the cancer regions identified in the individual types of MR images contribute to the actual tumour localisation. The blue colour indicates a cancer region from either of the DW image, the ADC map, or the K_{trans} map. The green colour indicates overlap of two cancer regions, while the red colour indicates overlap of cancer regions from all three images, and only such an overlap is considered a localised tumour.

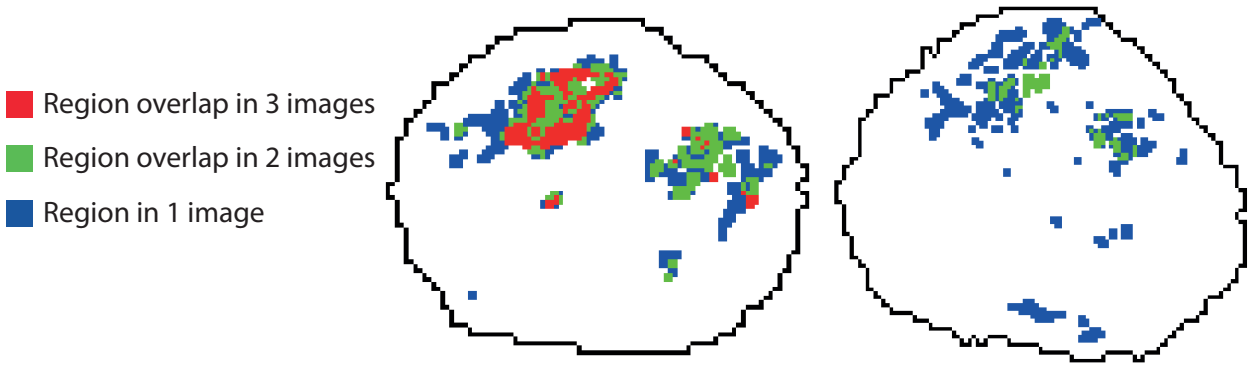

Figure 9.4: Two example overlaps of cancer regions in DW images, ADC maps, and K_{trans} maps. The prostate boundary is marked with the black mask. Red indicates total overlap, i.e. overlap of cancer regions in both DW image, ADC map, and K_{trans} map, green indicates agreement in two of the MR image types, and blue indicates a cancer region identified in just one of the images. **Left:** One example overlap. The red cancer region falls under suspicion of cancer in all three types of images and will be termed a localised tumour. **Right:** Another example overlap. Only two types of images agree, hence a substantial reduction of possibly false positives is achieved, when these are omitted.

9.2.1 Test of Numbers of Clusters in Fuzzy C-Means Clustering

Having segmented regions in each type of MR image, the next step is to keep only the cancer regions and discard all non-cancer regions. The purpose of this test is to determine the optimal number of clusters c in a FCM clustering to include every region suspicious of cancer in the

cluster herefore and exclude as many regions as possible not suspicious of cancer from this cluster.

In the test, FCM clustering was conducted in each type of MR images, DW images, ADC maps, and K_{trans} maps, and the classified cancer regions from each image type were overlaid each other cf. Figure 9.4, and only their overlap was considered a cancer region. The value for c was varied in order to achieve an acceptable classification of the regions. The test included $c = 3$, $c = 4$, $c = 5$, $c = 6$, and $c = 7$, and the results were evaluated qualitatively by visual inspection.

For each type of MR image, the number of clusters was tested for both the regions segmented using LoG edge detection (c_{LoG}) and for the regions segmented by the watershed transform (c_w). The test results are presented in the following.

Number of Clusters in Fuzzy C-Means Clustering of Results from LoG Edge Detection

- $c_{LoG} = 3$ produced under-segmentation in all images, both the DW images, ADC maps, and K_{trans} maps, for all subjects. This was seen as relatively dark regions in the DW images and K_{trans} maps and bright regions in the ADC maps were classified as cancer regions.
- $c_{LoG} = 4$ tended to include too dark regions in the DW images and K_{trans} maps, hence under-segmentation. In the ADC maps generally a good classification was produced, however, one subject tended to have too bright areas classified as cancer regions.
- $c_{LoG} = 5$ did not differ much from $c_{LoG} = 4$ for the DW images. In both the ADC maps and K_{trans} maps good classifications were produced for most subjects, however, a few possible cancer regions in the ADC maps for some some subjects were excluded.
- $c_{LoG} = 6$ tended to produce a good classification for the DW images and K_{trans} maps for most subjects. In the ADC maps too many dark and thus cancer regions were excluded.
- $c_{LoG} = 7$ produced a fine classification for one of the subjects in the DW images, however it excluded some bright and thus cancer regions suspicious for cancer in other subjects. In the K_{trans} maps no good classification was produced using $c_{LoG} = 7$.

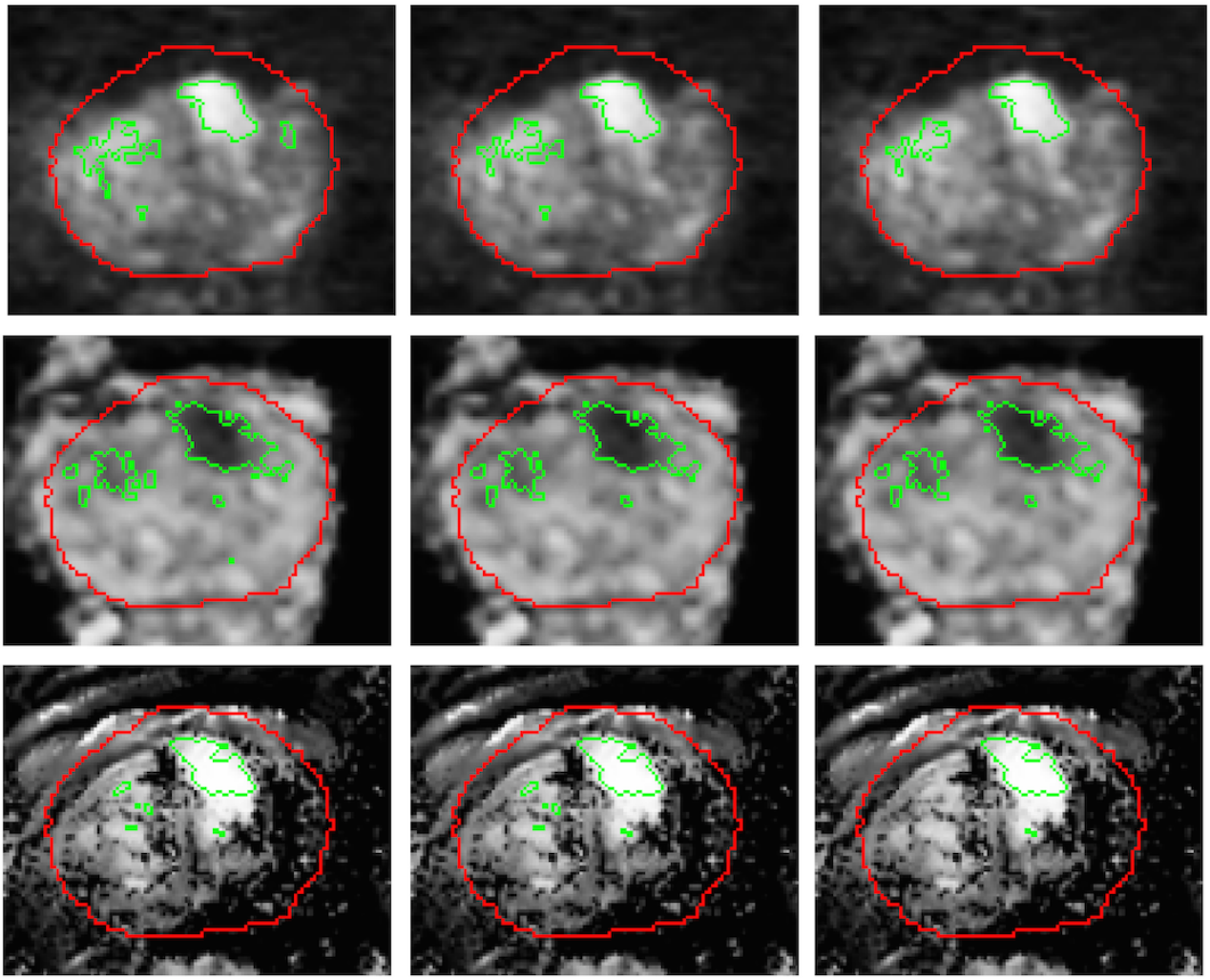

Figure 9.5: Identification of cancer regions from the set of cancer candidate voxels using LoG edge detection. From **Left** to **Right**: $c_{LoG} = 4$, $c_{LoG} = 5$, and $c_{LoG} = 6$. Subject 1, slice 38. Prostate boundary (red) and boundary of cancer regions (green). **Top:** Cancer regions overlaid DW image. **Middle:** Cancer regions overlaid ADC map. **Bottom:** Cancer regions overlaid K_{trans} map.

Number of Clusters in Fuzzy C-Means Clustering of Results from Watershed Transform

- $c_w = 3$ tended to produce under-segmentations in all images for all subjects.
- $c_w = 4$ as well tended to produce under-segmentations in the DW images and ADC maps for all subjects and in the K_{trans} maps for two of the subjects, however less pronounced.
- $c_w = 5$ kept only the very dark regions in the ADC maps for most subjects, while under-segmentation was still seen in the DW images and K_{trans} maps for most subjects.
- $c_w = 6$ tended to exclude too many bright regions in the ADC maps for all three subjects. In the DW images and K_{trans} maps only the very bright regions were retained.
- $c_w = 7$ tended to exclude regions suspicious for cancer in all images for most subjects.

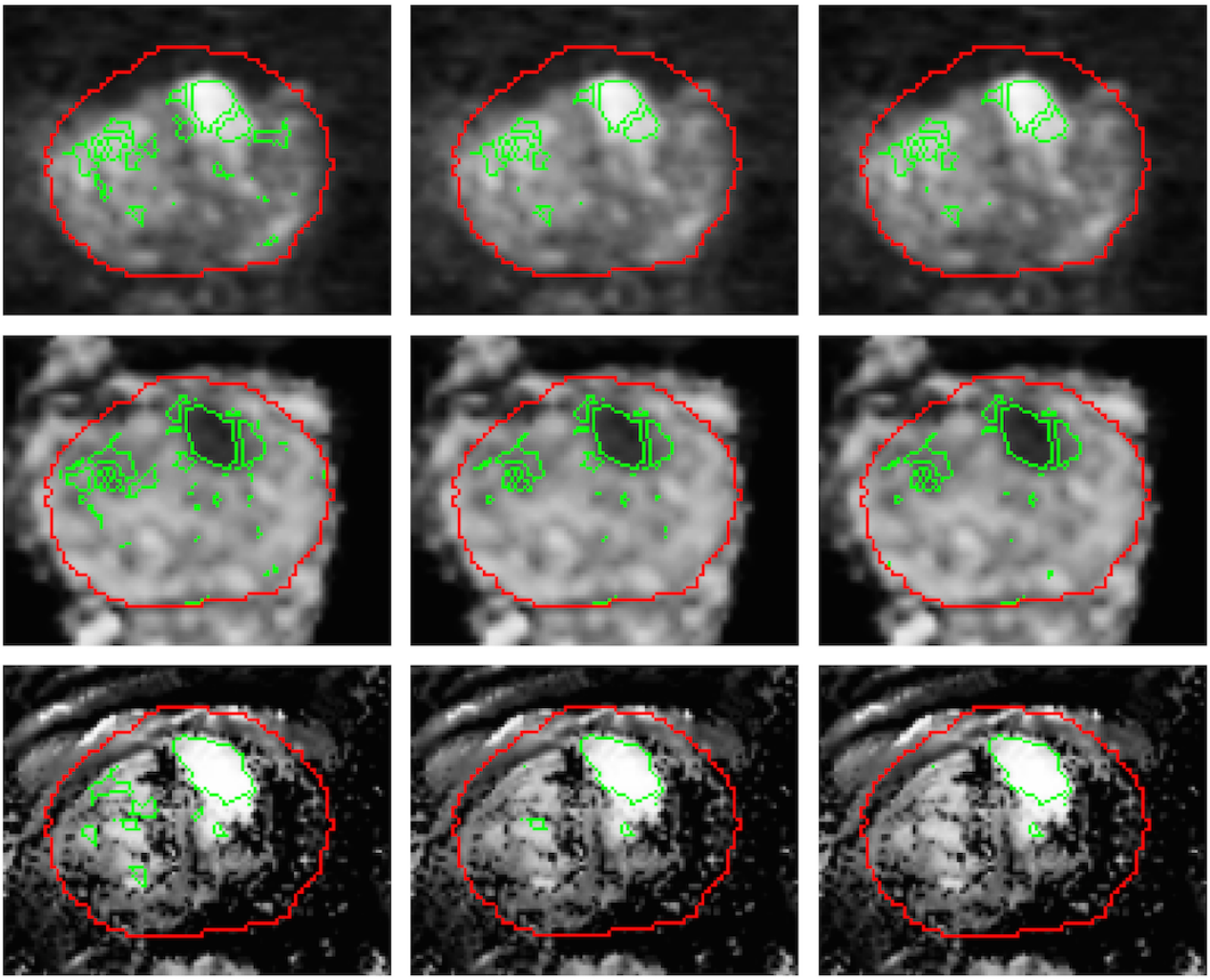

Figure 9.6: Identification of cancer regions from the set of cancer candidate voxels using watershed transform. From **Left** to **Right**: $c_w = 4$, $c_w = 5$, and $c_w = 6$. Subject 1, slice 38. Prostate boundary (red) and boundary of cancer regions (green).**Top:** Cancer regions overlaid DW image. **Middle:** Cancer regions overlaid ADC map. **Bottom:** Cancer regions overlaid K_{trans} map.

Some extent of what was believed as false positives was observed in each type of MR images for both the segmentation results from the LoG edge detection and watershed transform, however, this was reduced when only the overlaps of the cancer regions in all types of MR images were considered as tumours. Given the above observations and to ensure that all cancer regions are included when classifying the segmentations, the number of clusters in the FCM clustering in each MRI technique in the work here presented is set to $c_{LoG} = 6$ and $c_w = 6$ for the DW images, $c_{LoG} = 4$ and $c_w = 5$ for the ADC maps, and finally $c_{LoG} = 5$ and $c_w = 6$ for the K_{trans} maps.

9.3 Summary of Methods for Identification of Prostate Cancer Regions

Two methods of identification of cancer regions from the set of cancer candidate voxels have been presented. Both methods utilise prior knowledge of the appearance of cancer in the different types of MR images. The parameter configurations of the two methods are summed up in Table 9.1.

Method	Parameter
LoG edge detection	$n_{LoG} = 7$ $c_{LoG} = 6$ for DW images $c_{LoG} = 4$ for ADC maps $c_{LoG} = 5$ for K_{trans} maps
Watershed Transform	$n_w = 3$ $c_w = 6$ for DW images $c_w = 5$ for ADC maps $c_w = 6$ for K_{trans} maps

Table 9.1: Overview of the parameters of the two proposed methods for identification of cancer regions.

In total, the proposed framework for automated prostate cancer localisation consists of three processing steps, segmentation of the prostate, voxel classification, and identification of cancer regions based on either LoG edge detection or watershed transform. In order to investigate how the proposed framework performs, the localisation performance of the framework using LoG edge detection and the localisation performance of the framework using watershed transform are tested and validated against a ground truth established by expert statements of true tumour location. The validation procedure is presented in Chapter 10.

Chapter 10

Validation

The validation of the proposed framework for automated localisation of prostate cancer using multiparametric MRI investigates whether the cancer localisation results agree with the actual state of the subjects, and is important to gain knowledge of the performance of the methods as well as to assess whether the framework is clinically applicable.

Among the previous studies on automated prostate cancer detection or segmentation mentioned in Section 6.1, clear tendencies in the procedures for evaluation of these methods are seen. First of all, the majority of the studies have utilised histopathological specimens as ground truth [65, 79, 80, 82, 83, 84], i.e. post-radical prostatectomy whole mount sections of prostates have been available on which the presence and localisation of prostate cancer have been annotated by experienced radiologist. Next *ex vivo* imaging of the whole mount sections allows registration with the previously obtained *in vivo* multiparametric MRI for evaluation. Otherwise the evaluations have been based on manual segmentations of the prostate cancers by experts [85, 87]. Secondly, the majority of the studies utilise the same evaluation metrics. These are the area under the ROC curve (AUC) [64, 65, 82, 86, 87], and specificity and sensitivity [79, 80, 83, 84]. In addition some studies have utilised similarity measures such as the Dice similarity coefficient [79, 80, 84] or Jaccard index [83], while a single study lists the rates of true and false positives and true and false negatives [85].

10.1 Validation Procedure

The validation of the work presented in this project is divided into two parts. The first part seeks to investigate the performance of the voxel classification presented in Chapter 8, and the second part seeks to investigate the performance of the identification of cancer regions presented in Chapter 9. Input to the first part is all prostate voxels and output is cancer candidate voxels. Input to the second part is the cancer candidate voxels and output is localised tumour(s). In the second part, tumour localisation results produced by the LoG edge detection method and the watershed transform method cf. Section 9.1 are validated and compared.

Furthermore, many studies suggest an improved prostate cancer localisation performance when as much image information as possible is utilised [8]. At present, most work in the field of prostate cancer detection or localisation has been conducted in T2W images and ADC maps, or in T2W images, DW images and ADC maps. To test the alleged benefit from inclusion of K_{trans} maps, both the first and second parts of the validation procedure are validated using two different sets of multiparametric MRI data, including a set composed of T2W images, DW images, and ADC maps, and a set composed of T2W images, DW images, as well as both ADC maps and K_{trans} maps. The results produced by the use of the two sets of data are then compared. Figure 10.1 provides an overview of the validation procedure.

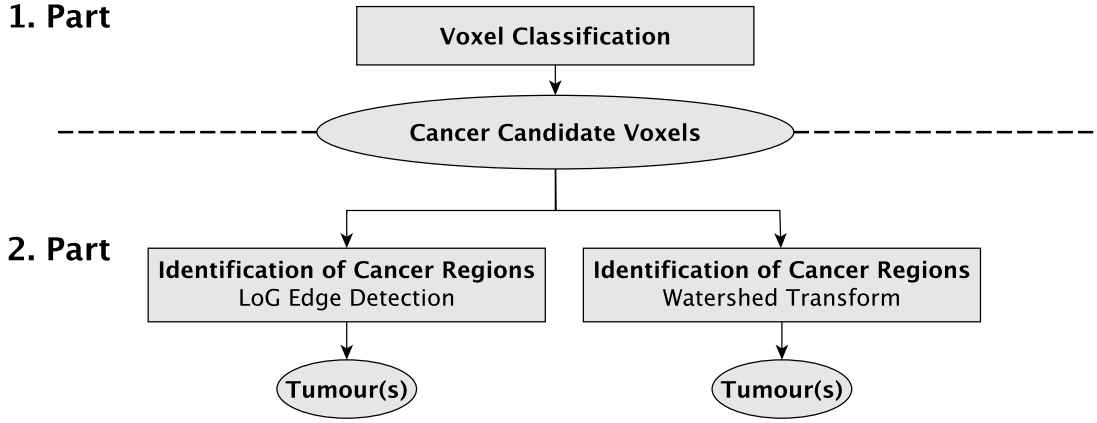

Figure 10.1: The validation procedure is divided into two parts, one part concerning the performance of the voxel classification, and one part concerning the performance of the identification of cancer regions. In this way, the entire proposed framework for automated prostate cancer localisation is validated. Both parts are applied to two sets of multiparametric MRI data; a set of T2W images, DW images, and ADC maps, and a second set of T2W images, DW images, ADC maps, as well as K_{trans} maps.

Both parts of the validation are based on comparison of the results with a ground truth on the basis of a set of performance metrics. The applied ground truth is described in Section 10.1.1 and the computed performance metrics are presented in Section 10.1.2.

10.1.1 Ground Truth

A ground truth is established by statements of true tumour regions from an expert. The statements are indicated by arrows in so-called key images. These are single T2W images with clear reference to the true tumour region(s). An example of a key image is given in Figure 10.2. After the expert made the true tumour statements for all subjects, the tissue areas stated have been confirmed cancer-positive by biopsy: In the biopsy procedure, specimens were sampled at the prostate locations indicated by the expert statements. Subsequently, the presence of cancer was evaluated and staged, if present, using the Gleason score as presented in Section 2.3.

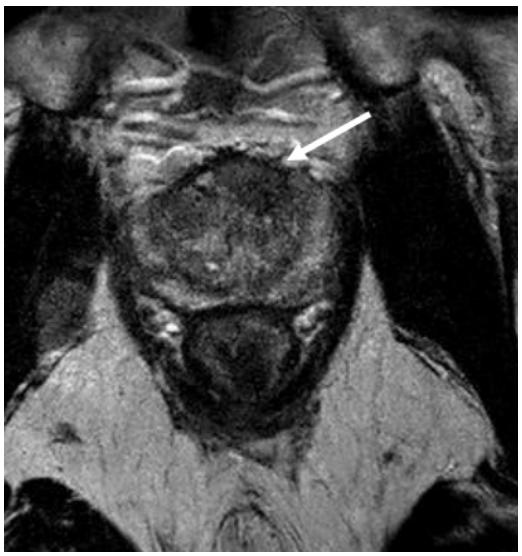

Figure 10.2: An example key image for a subject with expert statement: A true tumour region is indicated by the arrow. Subsequently, this region has been confirmed positive for cancer by biopsy. The Gleason score was evaluated to 6.

The key image for each true tumour originates from the original image volume and shows the middle most slice in which the true tumour appears, i.e. the true tumour may appear in slices on either side of the key image. In the work here presented, the basis for the framework applied is the isotropic image volume with a voxelsize of $0.5 \times 0.5 \times 0.5$ mm, cf. Section 5.3. As a consequence, one image slice in the original image volume is represented as 7 slices in the isotropic image volume. Thus, the true tumour may extend to many slices in the isotropic image volumes, despite only being apparent in a one or a few slices in the original image volume.

As shown in Figure 10.2, the true tumour region stated by the expert is diffuse and not well outlined. As a consequence, a tumour localised by the proposed framework is said to be correctly localised, if the localised tumour is a subregion of the expert annotated image region of the true tumour, or if the localised tumour includes the expert annotated region. Furthermore, as listed in Table 5.4, each subject maximum has two true tumours, and thus a maximum of two tumour localisations are expected for these subjects, whereas for the subjects with only one true tumour stated by the expert, only one tumour localisation is expected.

The biopsy results are used to conclude on the extent or size of a true tumour in order to decide if an image region marked as tumour by the proposed framework could be a subregion of the true tumour.

10.1.2 Performance Measures

The performance metrics applied in the validation of the voxel classification and in the validation of the identification of cancer candidates are presented in the following sections.

Validation of Voxel Classification

As the further processing step is applied only to the cancer candidate voxels, it is important to ensure that some of these voxels are included in the true tumour location indicated by the expert statement in the key image. Therefore, for each subject, it was investigated by visual inspection whether some of the cancer candidate voxels were located at the true tumour location indicated by the expert statement in the key image.

Validation of Identification of Cancer Regions

To validate the tumour localisation results produced by identification of cancer regions, four measures were put up seeking to answer the following questions:

1. Does the proposed framework localise a tumour at the location indicated by the expert statement?
    - If yes, what is the size of the correctly localised true tumour?
2. Does the proposed framework localise tumours at other locations?
    - If yes, what is the total size of the falsely localised tumours?

The first measure is *true tumour localisation* (TTL), the second measure is *false tumour localisation* (FTL), the third measure is *volume of correctly localised true tumour* (vTT), and finally the fourth measure is *volume of falsely localised tumours* (vFT).

TTL is basically measure of **YES** or **NO**, does the proposed framework mark a tumour region within the area stated as true tumour by the expert in the key image? From the TTL, an estimate of the true tumour detection rate can be determined, i.e. a measure of how well a specific method detects a true tumour at the correct location. Hence TTL becomes a measure of correct localisation rate. FTL, on the other hand, is a count measure, describing the number of image regions the proposed framework erroneously marks as tumours, false positive tumours, i.e. all tumour regions not located at areas indicated as true tumour by the expert statements in the key images. To enable a comparison of the tumours localised using the LoG edge detection method and the localised tumours using the watershed transform method, vTT and vFT are computed. These measures states the volumes in terms of number of voxels of the correctly and falsely localised tumours. Hence vTT and vFT provide an inter-method comparable measure of the correctly and falsely localised tumours.

The performance measures TTL, FTL, vTT, and vFT were determined for each subject. TTL was estimated based on the localisation results in the isotropic image corresponding to the key image. vTT was calculated as the number of voxels of the cancer region localised in the isotropic image corresponding to the key image with expert annotation and its connected cancer regions in adjacent slices. FTL and vFT were estimated from the falsely localised tumours within the entire image volume.

Determination of Performance Measures
In each isotropic image corresponding to a key image, it is first visually inspected whether the proposed framework has localised a tumour at the location marked by the arrow in the key image. Three possible outcomes of the TTL can result from the inspection of the isotropic image corresponding to the key image:

- TTL = **YES**, if the automated procedure has localised a tumour at the location marked by the arrow in the key image.
    - All voxels within the localised tumour volume is calculated as vTT.

- TTL = **NO***, if the automated procedure has not localised a tumour in the image exactly corresponding to the key image, but tumour(s) have been localised at a location otherwise corresponding to the expert annotated image region in one or more of the four adjacent images on either side in the isotropic image volume.
- TTL = **NO**, if the automated procedure has not localised a tumour neither in the isotropic image exactly corresponding to the key image nor in the four adjacent images on either side in the isotropic image volume.

Subsequently, if any tumours at locations different from the true tumour location stated in the key image have been localised, then these are considered falsely localised tumours and will add up in the measure of FTL. When the entire image volume has been investigated for falsely localised tumours, vFT is calculated.

Figure 10.3 shows an example of this approach. In the image to the left, the expert annotated key image from subject 9 is shown. In the image to the right, the corresponding image in the isotropic image volume is shown with correct localisation of true tumour marked in green and falsely localised tumour marked in yellow. The falsely localised tumour was not stated by the expert in the key image.

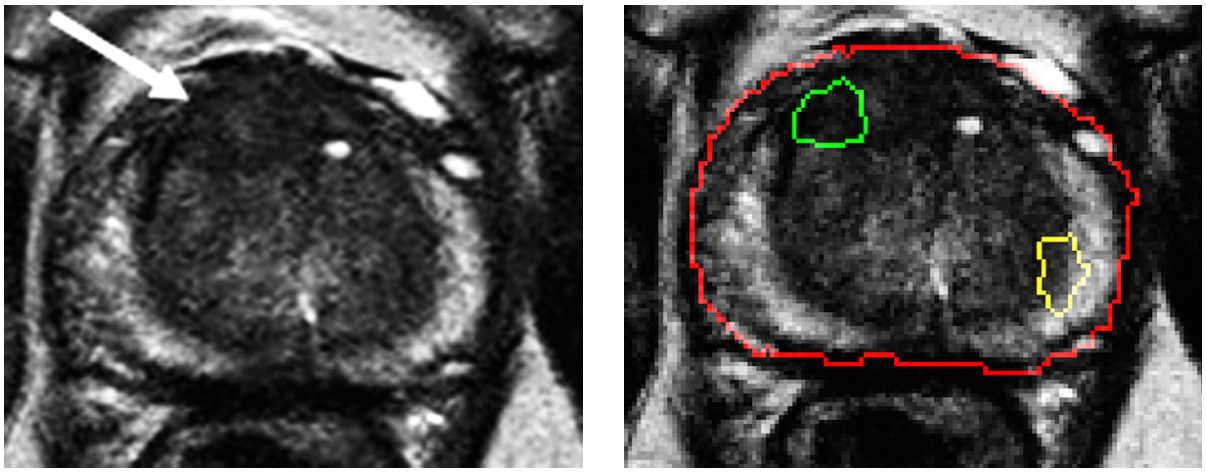

Figure 10.3: Illustration of true tumour localisation and false tumour localisation. **Left:** Key image from original image volume from subject 9 with expert statement of true tumour location indicated by arrow. **Left:** Corresponding image with boundary of prostate mask (red), boundary of a correctly localised true tumour (green), and boundary of a falsely localised tumour (yellow).

Chapter 11

Results

The validation of the proposed framework for automated prostate cancer localisation using multiparametric MRI was divided into two parts, including one part concerning the validation of the voxel classification and one part concerning the validation of the identification of cancer regions. For both parts, results from using two different sets of multiparametric MRI data were produced. The first set of multiparametric MRI data was composed of T2W images, DW images, and ADC maps, while the other multiparametric MRI data set was composed of T2W and DW images, ADC maps, and K_{trans} maps as well. The results produced by use of the different sets of multiparametric MRI data are compared to assess the proved benefit of integration of as much image information as possible. The results from the first part of the validation are presented in Section 11.1, and the results from the second part of the validation are presented in Section 11.2.

11.1 Performance of Voxel Classification

In Sections 11.1.1 and 11.1.2, the results from the voxel classification are presented. The voxel classification was conducted in all prostate voxels, i.e. all voxels contained in the results from the prostate segmentation presented in Chapter 7, and the voxel classification results are the cancer candidate voxels. The performance of the voxel classification was assessed using two different sets of multiparametric MRI data, a set composed of T2W images, DW images, and ADC maps and another set composed of T2W images, DW images, ADC maps, and K_{trans} maps as well.

11.1.1 Results of Voxel Classification Using T2W Images, DW Images, and ADC Maps

By visual inspection and comparison with ground truth is was seen that the voxel classification was able to classify cancer candidate voxels at the locations indicated by the expert statements for each of the 11 true tumours. Figure 11.1 provides two examples. Key images and images corresponding to the key images with cancer candidate voxels marked in green for subject 2 and 6 are shown. It is clearly seen that the arrows in the key images point at corresponding image areas with cancer candidate voxels.

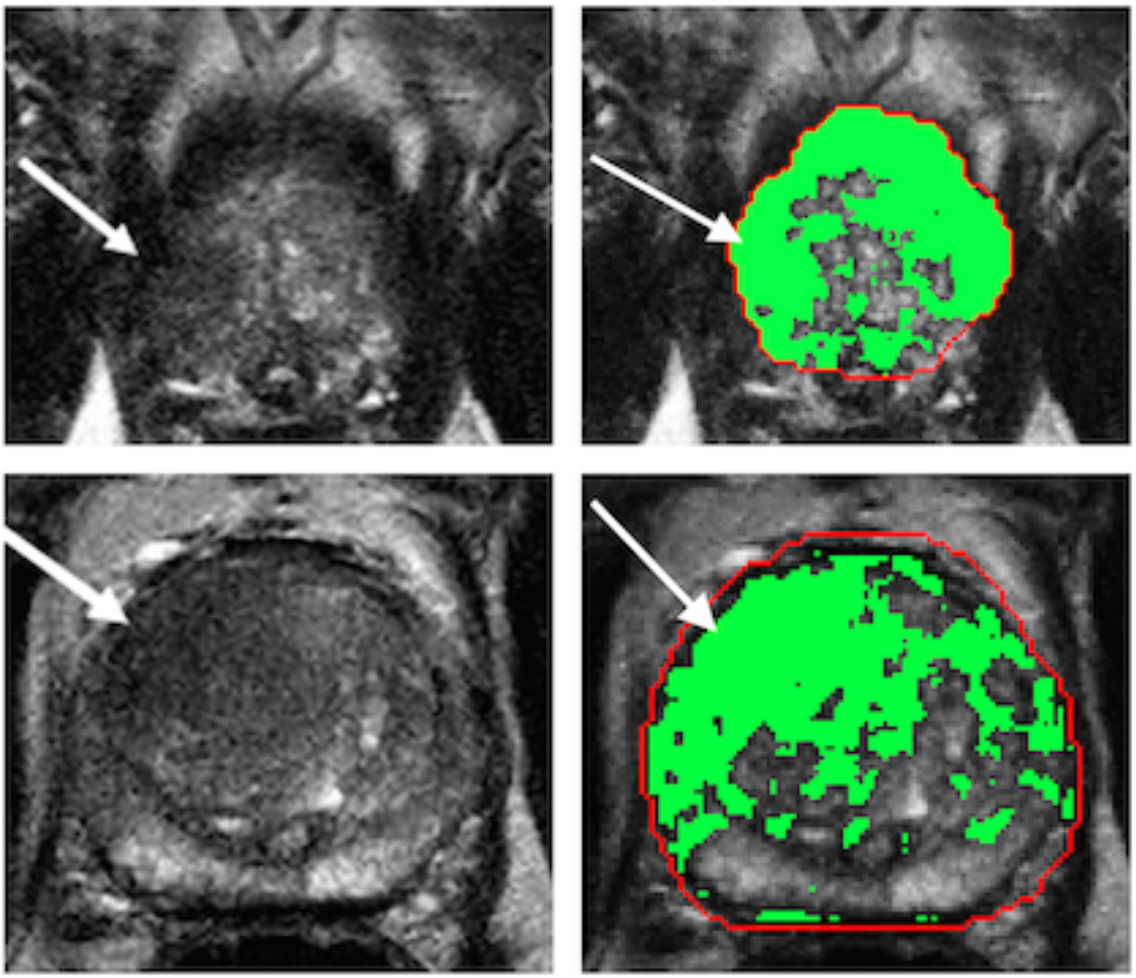

Figure 11.1: Cancer candidate voxels classified by use of T2W images, DW images, and ADC maps. **Top:** Axial T2W images for subject 2, slice 18. **Bottom:** Axial T2W images for subject 6, slice 39. **Left:** Key images with expert statement of cancer area indicated by arrows. **Right:** Corresponding images with boundary of prostate mask (red) and cancer candidate voxels (green). The arrow corresponds to the arrow in the key image.

11.1.2 Results of Voxel Classification Using T2W Images, DW Images, ADC Maps, and K_{trans} Maps

By visual inspection and comparison with ground truth it was seen that the voxel classification was able to classify cancer candidate voxels at the locations indicated by the expert statements for each of the 11 true tumours. Figure 11.2 provides two examples. Key images and images corresponding to the key images with cancer candidate voxels marked in green for subject 2 and 6 are shown. Again, it is clearly seen that the arrows in the key images point at corresponding image areas with cancer candidate voxels.

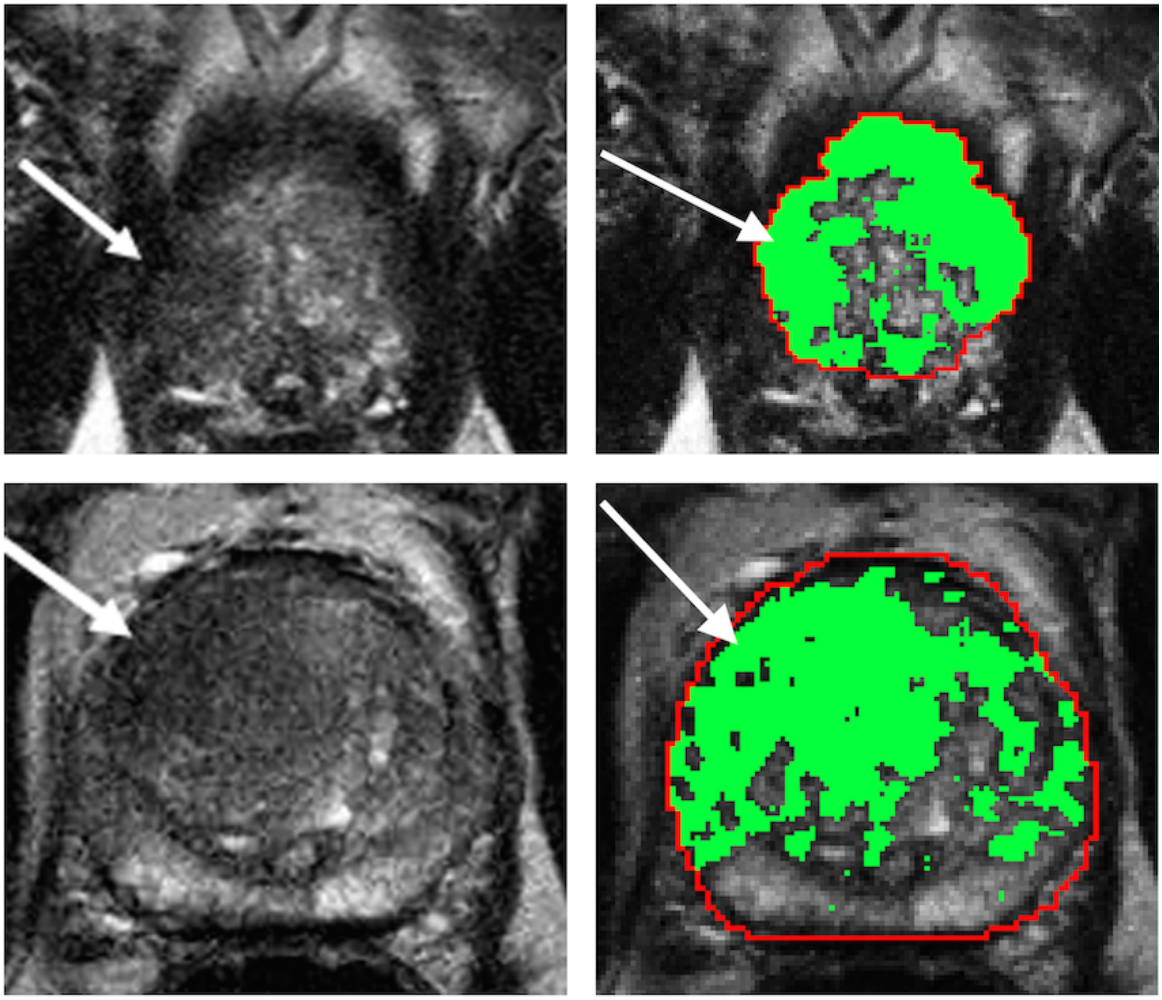

Figure 11.2: Cancer candidate voxels classified by use of T2W images, DW images, ADC maps, as well as K_{trans} maps. **Top:** Axial T2W images for subject 2, slice 18. **Bottom:** Axial T2W images for subject 6, slice 39. **Left:** Key images with expert statement of cancer area indicated by arrows. **Right:** Corresponding images with boundary of prostate mask (red) and cancer candidate voxels (green). The arrow corresponds to the arrow in the key image.

A comparison of the set of cancer candidate voxels classified using T2W images, DW images, and ADC maps, with the set of cancer candidate voxels classified using T2W images, DW images, ADC maps, and K_{trans} maps as well was made. By visual comparison of the two sets of cancer candidate voxels for each subject, only minimal differences were seen, as also noted when comparing the images in Figure 11.1 with the images in Figure 11.2. In terms of numbers of voxels in the two sets, overall, the sets of cancer candidate voxels classified using T2W images, DW images, and ADC maps were slightly larger than the sets of cancer candidate voxels classified using T2W images, DW images, ADC maps, and K_{trans} maps.

11.2 Performance of Identification of Cancer Regions

The performance of each of the two methods for identification of cancer regions based on either LoG edge detection or watershed transform has been assessed by evaluation of the results from the method against ground truth. Each method was applied on the two sets of cancer candidate

voxels resulting from voxel classification applied to the two different sets of multiparametric MRI, respectively. For the tumour localisation results presented in Section 11.2.1, the cancer candidate voxels classified by use of the multiparametric data set composed of T2W images, DW images, and ADC maps, are used as input for the LoG edge detection method and watershed transform method, which proceeded using information from the corresponding multiparametric data set. For the tumour localisation results presented in Section 11.2.2, the cancer candidate voxels classified using the multiparametric data set composed of T2W images, DW images, ADC maps, and K_{trans} maps, are used as input for the LoG edge detection method and watershed transform method, which proceeded using information from the corresponding multiparametric data set.

11.2.1 Results of Identification of Cancer Regions Using T2W Images, DW Images, and ADC Maps

For all nine subjects, TTL, vTT, FTL, and vFT cf. Section 10.1.2 were determined by visual inspection of the tumour localisation results. In the determination of TTL only the image corresponding to the key image with expert statement of true tumour and the four adjacent slices on either side in the image volume were inspected, whereas in the estimation of the FTL the entire image volume was inspected. The validation results are presented in Table 11.1 and are elaborated in the following sections. The asterisk in the table indicates that the method in this case was unable to localise a tumour region in the image exactly corresponding to the key image, however, in a nearby image a tumour was localised at the location otherwise corresponding to the expert annotated true tumour in the key image.

	LoG Edge Detection				Watershed Transform			
Subject	TTL	vTT	FTL	vFT	TTL	vTT	FTL	vFT
1	YES	9025	3	4199	YES	9187	3	4450
2	NO*	0	20	33662	NO*	0	17	16697
3	YES YES	4410 763	1	910	YES YES	3154 722	1	268
4	YES YES	15247	7	2092	YES YES	7574 3571	2	273
5	YES	620	5	4802	NO*	0	3	699
6	YES	24669	1	235	YES	33630	1	2188
7	YES	720	5	2508	YES	74	2	138
8	YES	2380	0	0	YES	2457	0	0
9	YES	8934	5	2782	YES	163	3	1653

Table 11.1: Validation results for automated localisation of prostate cancer using the multiparametric MRI data without K_{trans} maps. * A region suspicious for cancer was localised at the location of the expert annotated tumour but in a nearby image.

In general, the localisation results for both the LoG edge detection method and watershed transform method were promising for most subjects. The LoG edge detection method was able to correctly localise 10 of 11 true tumours. For one subject no false tumours were localised, and for most subjects the number of false positive tumours ranged from 0-7, however, 20 false positive tumours were localised for subject 2. Furthermore, for a single subject no tumour was correctly localised in the image exactly corresponding to the key image with expert annotation, however, possibly a true tumour was localised in an image located adjacent to the image corresponding to the key image. The watershed transform method was able to correctly localise 9 of 11 true tumours. For most subjects the number of false positive tumours ranged from 0-3, however, 17 false positive tumours were localised for subject 2. The watershed transform was unable to localise the true tumours in the images exactly corresponding to the key images for two subjects, however, possibly true tumours were localised in images located adjacent to the image corresponding to the key image. This is an indication that the watershed transform method actually localised a true tumour for these subjects as well. Examples of correct localisations of the second true tumour for subject 3 for both methods are shown in Figure 11.3.

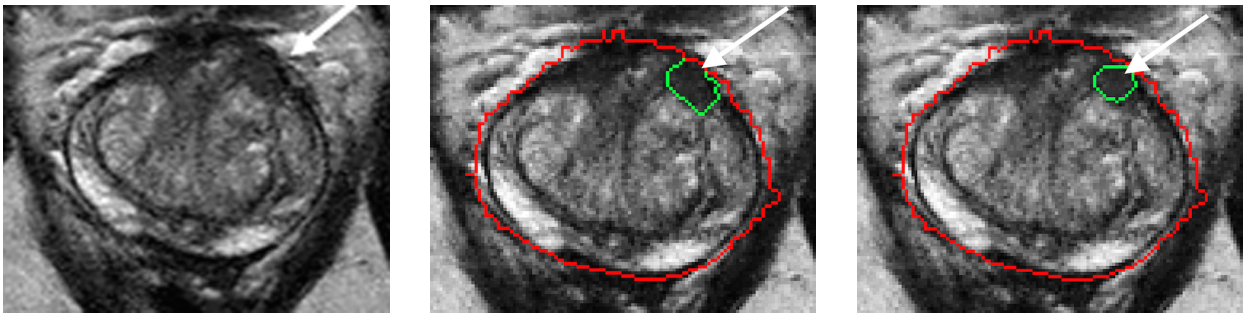

Figure 11.3: Axial T2W images for subject 3, slice 55. **Left:** Key image with expert statement of cancer area indicated by arrow. **Middle:** Corresponding image with tumour localisation results by use of the LoG edge detection method. **Right:** Corresponding image with tumour localisation results by use of the watershed transform method. Boundary of prostate mask (red) and boundaries of the correctly localised tumour (green). The arrow corresponds to the arrow in the key image.

Both methods were able to correctly localise both true tumours for both subject 3 and subject 4. For subject 3, both methods localised two tumours as the two true tumours, and for subject 4 the watershed transform method localised two tumours as the two true tumours as well, while the LoG edge detection method localised a single tumour region containing both true tumours. This is illustrated in Figure 11.4, in which the key images for the two tumours, different image slices, are shown in the first column, and the localisation results in the corresponding images are shown in the second column. In these images, it seems that the two tumours are not connected, however, in the images in between, it is apparent that they are connected. From the ground truth it cannot be stated whether the two true tumours actually are connected as one large true tumour. In fact, the only certainty is that cancer cells have been sampled from the regions indicated by the arrows. Of the regions marked in green in the top right image, a region is correctly marked for the first tumour, i.e. the true tumour indicated in the top key image, at the true location to the left, while the region marked a tumour to the right in this top image could possible be the beginning of what has been stated as the second true tumour, indicated in the key image at the bottom. The remaining regions, marked in yellow, are false positive tumours localised. Considering the location of the second tumour in the top key image and correspondingly, considering the location of the first tumour in the bottom key image, the appearances of both tumours in both images might be correct.

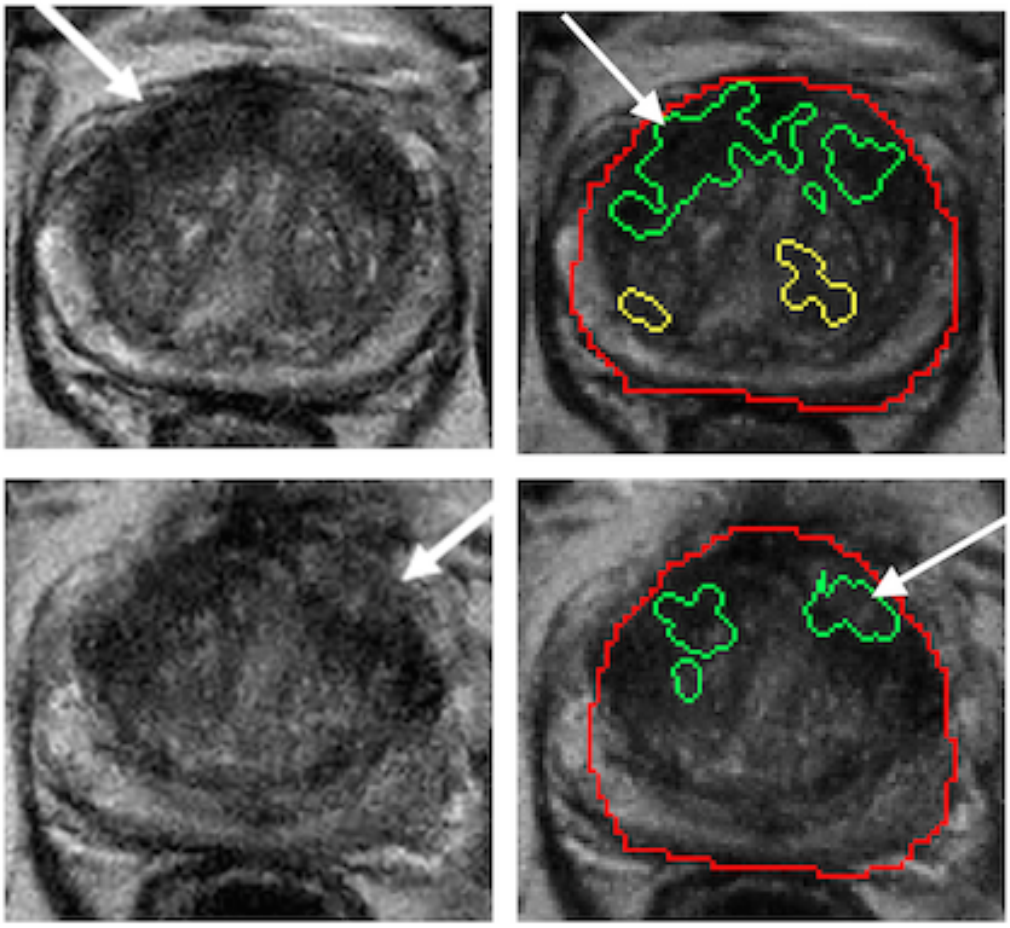

Figure 11.4: Top: Axial T2W images for subject 4, slice 51. **Left:** Key image with expert statement of cancer area indicated by arrow. **Right:** Corresponding image with boundary of prostate mask (red), boundaries of true tumours localised (green), and boundaries of falsely localised tumours (yellow). **Bottom:** Axial T2W images for subject 4, slice 65. **Left:** Key image with expert statement of cancer area indicated by arrow. **Right:** Corresponding image with boundary of prostate (red) and boundaries of true tumours localised (green). The arrows in the images to the right correspond to the arrows in the key images to the left.

The LoG edge detection method was able to correctly localise a true tumour for subject 5 which the watershed transform method was unable to localise. However, the watershed transform method localised a tumour in an adjacent image to the key image, at a location corresponding to the true tumour location stated by the expert. This is illustrated in Figure 11.5.

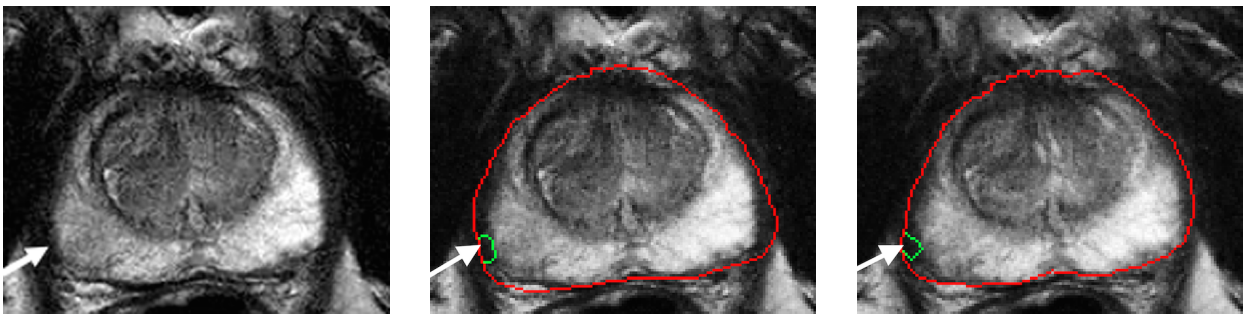

Figure 11.5: Axial T2W images for subject 5. **Left:** Key image with expert statement of cancer area indicated by arrow. **Middle:** Corresponding image, slice 41, with tumour localisation results by use of the LoG edge detection method. **Right:** Nearby image, slice 39, with tumour localisation results by use of the watershed transform method. Boundary of prostate mask (red) and boundaries of the correctly localised tumour (green). The arrow corresponds to the arrow in the key image.

The watershed transform method was able to correctly localise less true tumours than the LoG edge detection method, however, the watershed transform also localised less false positive tumours. This is illustrated in Figure 11.6 for subject 7.

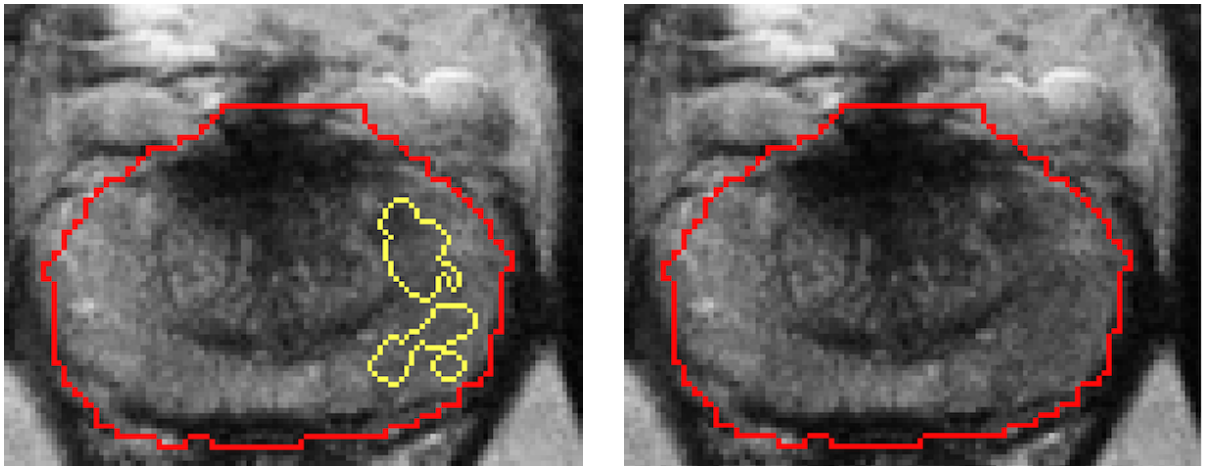

Figure 11.6: Axial T2W images for subject 7, slice 41. Boundary of prostate mask (red) and boundaries of a falsely localised tumour (yellow). **Left:** Tumour localisation results by use of the LoG edge detection method: A falsely localised tumour. **Right:** Tumour localisation results by use of the watershed transform method: No falsely localisation of tumour.

By visual inspection of the correctly localised true tumours for all subjects in the DW images and ADC maps, it was seen that they varied in terms of homogeneity and clear boundaries between dark and bright regions. This was observed in the localisation results from the LoG edge detection method and in the localisation results from the watershed transform method as well. Some of the correctly localised tumours were well-defined as clear bright regions in the DW images and clear dark regions in the ADC maps with their boundaries seemingly correctly placed at rapid changes of grey-level intensities. Other localised tumours were more inhomogeneous in grey-level intensity and did not have a well-defined and clear boundary. Furthermore, a localised tumour with a clear boundary in the DW image did not necessarily have a corresponding clear boundary in ADC map, and vice versa. An example of a well-defined tumour in a DW image and ADC map was seen for subject 8 and is shown in Figure 11.7.

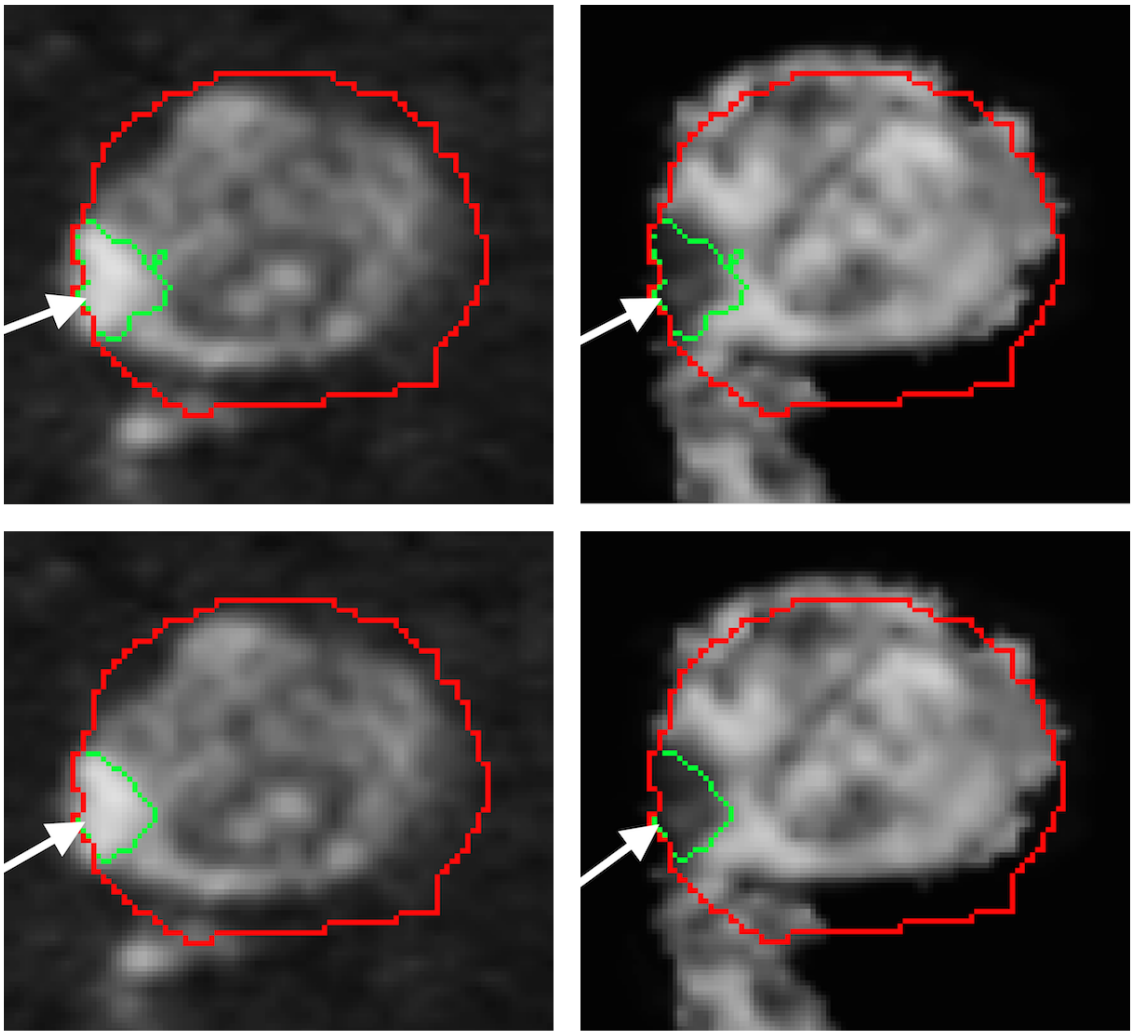

Figure 11.7: Subject 8, slice 28. Boundary of prostate mask (red), boundaries of the correctly localised tumour (green). The arrows indicates the expert statement of cancer area. **Top:** Tumour localisation results by use of the LoG edge detection method. **Bottom:** Tumour localisation results by use of the watershed transform method. **Left:** Axial DW image. **Right:** Axial ADC map.

11.2.2 Results of Identification of Cancer Regions Using T2W Images, DW Images, ADC Maps, and K_{trans} Maps

For all nine subjects, TTL, vTT, FTL, and vFT cf. Section 10.1.2 were determined by visual inspection of the tumour localisation results. In the determination of TTL only the image corresponding to the key image with expert statement of true tumour and the four adjacent slices on either side in the image volume were inspected, whereas in the estimation of the FTL the entire image volume was inspected. The validation results are presented in Table 11.2 and are elaborated in the following sections. The asterisk in the table indicates that the method in this case was unable to localise a tumour region in the image exactly corresponding to the key image, however, in a nearby image a tumour was localised at the location otherwise corresponding to the expert annotated true tumour in the key image.

	LoG Edge Detection				Watershed Transform			
Subject	TTL	vTT	FTL	vFT	TTL	vTT	FTL	vFT
1	YES	8042	2	913	YES	8621	1	373
2	NO*	0	12	17041	NO	0	10	10378
3	YES YES	3814 367	1	436	YES NO	3217 0	0	0
4	YES YES	3103 4571	3	867	YES YES	3740 3413	0	0
5	NO	0	0	0	NO	0	0	0
6	YES	14413	1	912	YES	26264	0	0
7	YES	7026	1	107	YES	108	0	0
8	YES	667	0	0	YES	512	0	0
9	YES	3768	5	2782	YES	50	2	213

Table 11.2: Validation results for automated localisation of prostate cancer using the multiparametric MRI data with the K_{trans} maps. * A region suspicious for cancer was localised at the location of the expert annotated tumour but in a nearby image.

With the inclusion of information from K_{trans} maps, a deterioration in localisation performance was seen for both the LoG edge detection method and the watershed transform method.

The LoG edge detection method was able to correctly localise 9 of 11 true tumours. For a single subject, no tumour was localised at all, while for another subject no tumour was correctly localised in the image exactly corresponding to the key image with expert annotation, however, possibly a true tumour was localised in an image located adjacent to the image corresponding to the key image. Comparison of the results for the LoG edge detection method in Table 11.1 with the corresponding results in Table 11.2 proves that the performance of the proposed framework slightly deteriorates in terms of correct localisation of true tumours with the inclusion of K_{trans} maps in the multiparametric MRI data set, however, the number of falsely localised tumours decreases.

Comparison of the results for the watershed transform method in Table 11.1 with the corresponding results in Table 11.2 proves that the performance of the watershed transform method also deteriorates with the inclusion of K_{trans} maps in the multiparametric MRI data set. Only 8 of 11 true tumours were correctly localised, however, a large decrease in the number of falsely localised tumours was seen for all subjects.

Examples of correct localisations of the true tumour by use of LoG edge detection method and watershed transform method for subject 1 are shown in Figure 11.8.

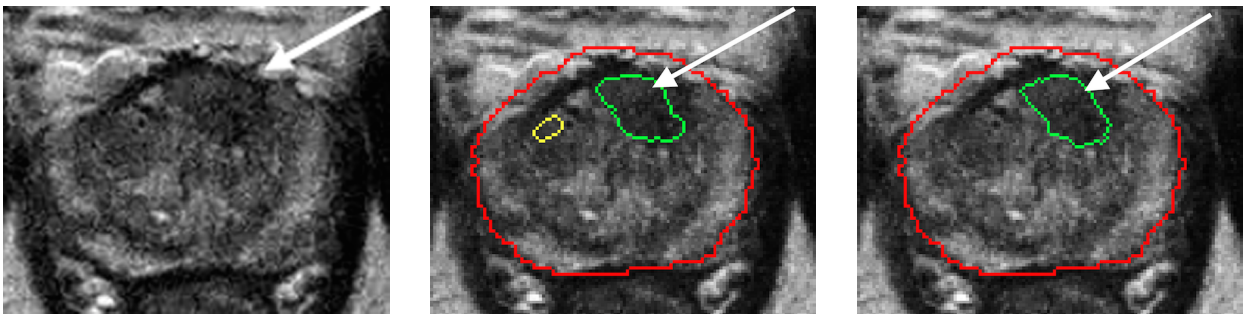

Figure 11.8: Axial T2W images for subject 1, slice 37. Boundary of prostate mask (red), boundary of the correctly localised tumour (green), and boundary of falsely localised tumour (yellow). The arrow corresponds to the arrow in the key image. **Left:** Key image with expert statement of cancer area indicated by arrow. **Middle:** Corresponding image with tumour localisation results by use of the LoG edge detection method. Notice the falsely localised tumour. **Right:** Corresponding image with tumour localisation results by use of the watershed transform method.

For most subjects the true tumours localised by the two methods, LoG edge detection and watershed transform, using the multiparametric data set including K_{trans} maps seem to be smaller than those found when applying the same methods to the multiparametric MRI data set composed of only T2W images, DW images, and ADC maps. The volumes of the correctly localised true tumours, vTT, decreased for most subjects, when information from K_{trans} maps was included in the multiparametric MRI data set. Comparison of these now smaller true tumours with the true tumours correctly localised when information from K_{trans} maps was omitted, seemingly the true tumours found without K_{trans} information are better defined in terms of homogeneous bright or dark regions. This was especially seen for the ADC maps. An example of this is shown in Figure 11.9, in which the top images show the true tumours localised by use of the watershed transform method without K_{trans} information and the bottom images show the true tumours localised by use of the watershed transform method with inclusion of K_{trans} information. The tumour in the top images has a well-defined boundary in the ADC map. From the ground truth, it cannot be established whether the tumour boundaries in the top row are more correct than the tumour boundaries in the bottom row. However, important to notice is that a false positive tumour was localised in the omission of K_{trans} information. The same observations were seen for the localisation results by use of the LoG edge detection for most subjects.

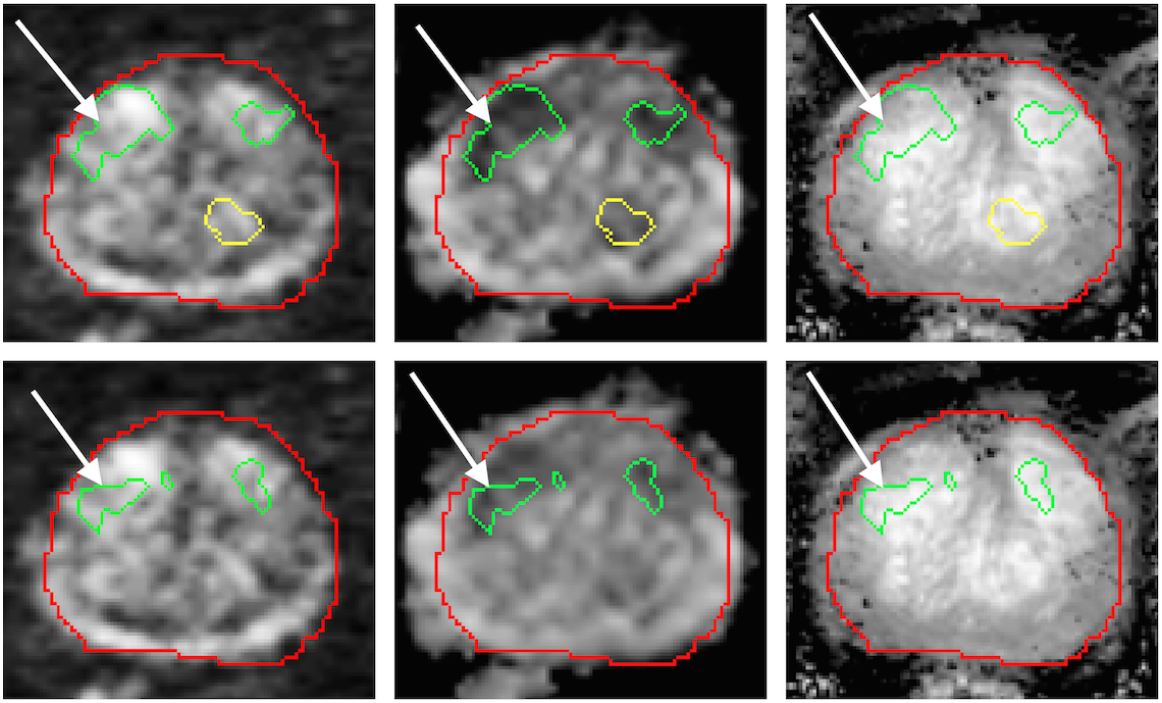

Figure 11.9: Axial DW images, ADC maps, and K_{trans} maps for subject 4, slice 51. Boundary of prostate mask (red), boundary of correctly localised true tumours (green) and falsely localised tumour (yellow). The arrows correspond to the arrow in the associated key image. **Top:** True tumours localised by use of the watershed transform method without inclusion of K_{trans} information. The region of the localised true tumour appears as a well-defined homogeneous region, especially pronounced in the ADC map, however, a false positive tumour was localised in addition. **Bottom:** True tumours localised by use of the watershed transform method with inclusion of K_{trans} information. The region of the localised true tumour regions is not as well-defined.

The watershed transform method was unable to localise a total of three true tumours. Among these, the LoG edge detection method was able to correctly localise the second true tumour of subject 3. Furthermore, without inclusion of information from K_{trans} maps, the LoG edge detection method was finely able to localise the true tumour for subject 5. However, with inclusion of information from K_{trans} maps, the methods was suddenly unable to localise the true tumour. This can possibly be explained by a closer look into the image content in the specific K_{trans} map, as illustrated in Figure 11.10.

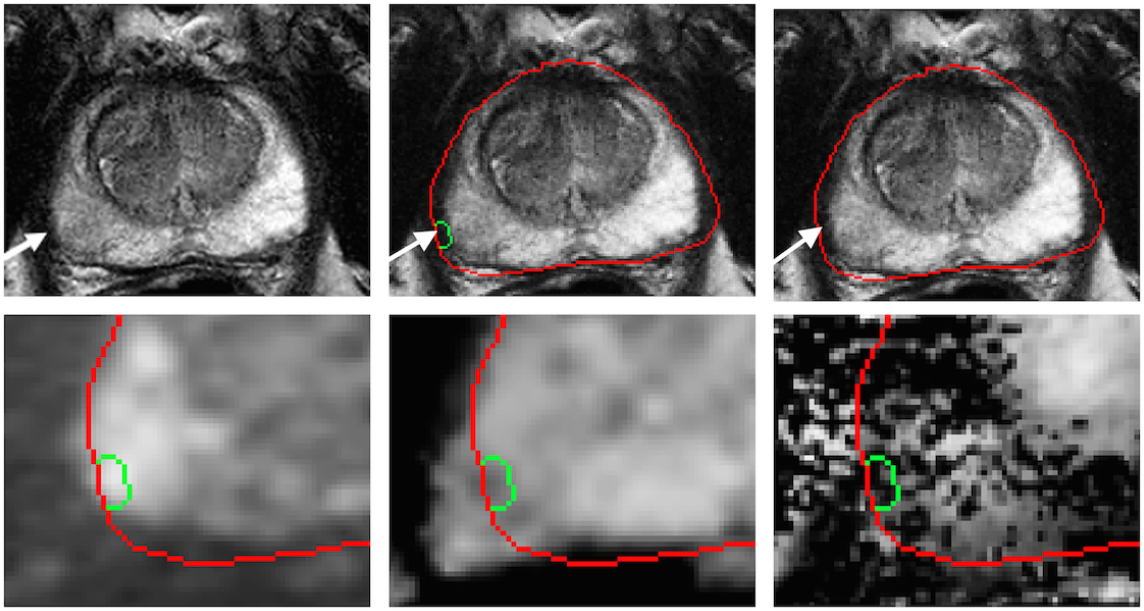

Figure 11.10: Axial images of subject 5. **Top Left:** Key image with expert statement of cancer area indicated by arrow. **Top Middle:** Corresponding image with prostate boundary mask (red) and tumour localisation results (green) by use of the LoG edge detection method without inclusion of K_{trans} information. The true tumour is correctly localised. **Top Right:** Corresponding image with prostate boundary mask (red), tumour localisation results with inclusion of K_{trans} information. No tumour was localised. **Bottom:** Enlarged view of the correctly localised tumour (green) in the omission of K_{trans} information overlaid **Left:** DW image, **Middle:** ADC map, and **Right:** K_{trans} map. Notice the lack of distinctiveness between the tumour region and surrounding tissue in the K_{trans} map.

11.3 Summary of Validation Results

The validation consisted of two parts, each of which was tested using two different sets of multiparametric data, one set including T2W images, DW images, and ADC maps only, and another set including T2W images, DW images, ADC maps, K_{trans} maps as well. Through the two parts, the performance of the entire proposed framework for automated prostate cancer localisation was assessed.

The performance of the voxel classification was validated in the first part. The voxel classification succeeded in correctly classifying the voxels corresponding to the true tumour regions indicated by the expert annotations in the set of cancer candidate voxels. However, generally abundantly many voxels were included in the set of cancer candidate voxels. Minimal differences between the sets of cancer candidate voxels resulting from the different sets of multiparametric MRI data were observed.

In the second part of the validation, the performance of the identification of cancer regions was tested. The cancer candidate voxels were segmented into regions which were classified into cancer regions or region representing normal prostate tissue. The segmentation was conducted by either the LoG edge detection or the watershed transform. An overview of the localisation results produced by the use LoG edge detection and watershed transform in the step for identifying cancer regions is presented in Table 11.3.

The first column specifies which of the two methods, LoG edge detection or watershed transform, was used for the identification of cancer regions in the framework for automated prostate cancer localisation. The second column contains the fraction of true tumours correctly localised to all true tumours for that specific method. The third column contains the mean FTL for that method, calculated as the mean FTL for all subjects.

T2W images, DW images, and ADC maps		
Method	Fraction of TTL	Mean of FTL
LoG Edge Detection	10/11	5.22
Watershed Transform	9/11	3.56
T2W images, DW images, ADC maps, and K_{trans} maps		
Method	Fraction of TTL	Mean of FTL
LoG Edge Detection	9/11	2.78
Watershed Transform	8/11	1.44

Table 11.3: Overview of the results from the framework for automated prostate cancer localisation using either LoG edge detection or watershed transform in the step for identifying cancer regions.

Both methods were unable to detect any true tumours for subject 2 and subject 5, with inclusion of information from K_{trans} maps. However, when information from K_{trans} maps was omitted, the LoG edge detection correctly localised the true tumour for subject 5, and was able to localise the possibly true tumour for subject 2 in an image located adjacent to the image corresponding to the key image. Similarly, the watershed transform method was able to localise possible true tumours for both subject 2 and 5 in images located adjacent to the images corresponding to the key images.

Generally, the LoG edge detection method localised more false positive tumours than the watershed transform method, but for both methods a halving in these rates was seen, when information from K_{trans} maps was included in the applied set of multiparametric MRI data.

From comparison of the vTT for the tumour localisation results for the LoG edge detection method and the watershed transform method for each subject, it is seen that the size of the localised true tumour varies between the two methods, and the LoG edge detection tended to localise the largest tumours. The same results were seen by comparison of the vFT for the two methods for each subject. The LoG edge detection method tended to produce the largest vFT. However, whether the larger vFT is due to localisation of more false positive tumours, which generally was seen for the LoG edge detection method, or if the size of the falsely localised tumours actually is larger for the LoG edge detection method is not clear.

Chapter 12

Discussion

This chapter focuses on discussion of questions raised during the validation of the proposed solution for automated prostate cancer localisation, including advantages and limitations of the ground truth available, the voxel classification, and the identification of cancer regions. The validation results in terms of true and false tumour localisations are discussed, and suggestions for improvement and future work are presented.

12.1 Ground Truth

The ground truth available for this project comprises tumour key images, one key image per true tumour, with statements of the true tumour localisations indicated by an expert. This facilitates the validation of whether the proposed solution localises the true tumours correctly, and whether the proposed solution is prone to localise false positive tumours. However, the proposed framework does more than simply mark areas of prostate cancer. It marks the boundaries of tumours as well.

The proposed framework for automated prostate cancer localisation exploits the assumptions of typical prostate cancer appearance in the different types of MR images cf. Section 3.3. With these assumptions in mind during visual inspection of the localisation results, the boundaries of the correctly localised true tumours seemingly mark what potentially could be the true tumour boundaries for most subjects. A correct localisation of the tumour could aid in targeting biopsy procedures and save the patient from unnecessary repeat biopsies. Yet another highly sought-after property is a solution able to correctly outline the tumour boundary. Such a solution could enable focused radiotherapy during treatment, an approach associated with beneficial outcome in local prostate cancer [125]. Unfortunately the ground truth available does not enable detailed quantitative validation of the accuracy of the correctly localised true tumour's boundary. Furthermore, from the validation results it is assessed that the tumours localised by use of LoG edge detection for the step of identification of cancer regions generally have larger volumes than the tumours localised by use of watershed transform. However, by the ground truth available, it can not be stated which of the methods produces tumour boundaries most in accordance with the true tumour boundaries.

Last but not least, more studies have pointed out a significant inter and intra-observer variability for human readers of multiparametric MRI [80, 81, 83, 84, 106]. Having expert statements available from a single expert only, it might give cause to doubt the quality of the ground truth in this project. However, this doubt is accommodated for as all the true tumours have been confirmed positive for cancer by biopsy.

12.2 Voxel Classification

The reasoning behind the application of a combined intensity and texture analysis in the classification of cancer candidate voxels in this project is based on a study by Hoeks et al. [8] suggesting prostate cancer can be differentiated from benign conditions in the prostate based on measures of intensity and homogeneity.

The available ground truth does not enable a detailed quantitative validation of the voxel classification. Though, from the validation results it can be seen that the entire proposed solution for automated prostate cancer localisation, i.e. voxel classification followed by identification of cancer regions, is able to localise most of the true tumours correctly. This indicates a sufficient performance of the framework and as such the voxel classification is verified indirectly.

From the validation results it is not possible to directly assess whether the voxel classification step aids in the localisation performance, e.g. by reducing the number of false positive localised tumours. However, in order to achieve a more targeted tumour localisation already from the voxel classification, a few proposals for improvement are briefly described in the following.

An obvious proposal for improving the voxel classification is to select the most discriminative features for the classification of prostate voxels into cancer candidate voxels and voxels of normal tissue. In the work here presented, the features are selected on the basis of experience obtained in other studies of classification into cancer and normal tissue. Most preferably the set of features should be highly correlated to the classification but uncorrelated with each other. However, it is expected that some of the texture features used here in the voxel classification will be correlated to some extent. For instance, the homogeneity feature, which describes the homogeneity in grey-level intensities in the image, is expected to be correlated with the energy feature, which describes the uniformity in the texture. It would be interesting to investigate how correlated the features are, and only select the most discriminative features for the FCM clustering. Access to training data could enable a learning phase in which the optimal set of features could be determined for the best discrimination of cancer voxels from normal tissue voxels.

Another proposal to improve the performance of the voxel classification and thus the performance of the proposed framework could be integration of anatomical information in the automated prostate cancer localisation. It is well known that up to 70% of cancer appears in the peripheral zone (PZ) cf. Section 2.1. Moreover, the appearance of normal prostate tissue alters according to the different anatomic zones of the prostate, cf. Section 3.3. This alteration is especially pronounced in the T2W images, and possibly affects the distinction between cancer tissue and normal tissue throughout the prostate. Addition of the anatomical localisation of each voxel in the prostate, i.e. whether the voxel is a PZ voxel or a CG (central gland) voxel, to the feature vector might potentially bring an improved tumour localisation performance. Information on the prostate zones may be determined from MRI. More studies have shown promising results in segmentation of the prostate zones, or more specifically, in division of the prostate into PZ and CG from MRI. Chi et al. [126] have segmented the PZ and CG in multiparametric MRI consisting of T2W images and ADC maps by means of probabilistic atlases of the prostate zones, together with a trained classifier. They were able to segment the zones in the prostate and achieved a DSC of 0.52 ± 0.09 for the PZ and a DSC of 0.83 ± 0.04 for the CG. Another approach has been taken by Litjens et al. [127], who have proposed a segmentation of the prostate zones based on voxel classification. They have suggested a set of

positional, intensity, and texture features representing the difference between the two prostate zones, the PZ and the CG. By means of training data and a linear discriminant classifier, the characteristics of the two prostate zones are learnt. The performance of the proposed voxel classification segmentation was superior when compared to a multi-atlas segmentation in this study - and also when compared to the results from Chi et al. - with a DSC of 0.75 $\pm$ 0.07 versus 0.57 $\pm$ 0.19 for the PZ and a DSC of 0.89 $\pm$ 0.03 versus 0.80 $\pm$ 0.013 for the CG. As the framework for automated prostate cancer segmentation in the work here presented already utilises a voxel-based classification in the classification of cancer candidate voxels, the addition of features describing the anatomical location of a voxel could be implemented without major complications and possibly improve the prostate cancer localisation performance.

12.3 Identification of Cancer Regions

In the proposed framework for automated prostate cancer localisation, cancer regions are identified in the set of cancer candidate voxels in order to finally localise tumours. Two different methods for the region segmentation are proposed, the Laplacian of Gaussian (LoG) edge detection method and the watershed transform method. By comparison of the results of identified cancer regions for the two methods, a clear difference in the performances of the methods is observed. Applied to the multiparametric MRI data set composed of T2W images, DW images, and ADC maps, the LoG edge detection method was able to localise correctly 10 of 11 true tumours, while the watershed transform method was able to localise correctly 9 of 11 true tumours, and in fact, both methods were unable to localise the true tumour for subject 2. However, the size of the correctly localised true tumours from the two methods varied to a large extent. The best tumour localisation in terms of correct localisation of true tumours with minimum falsely localised tumours was achieved for the use of watershed transform for the step of identification of cancer regions.

Furthermore, applied to the multiparametric MRI data set composed of T2W images, DW images, ADC maps, and K_{trans} maps, the LoG edge detection method was again slightly superior to the watershed transform method, as it was able to localise a true tumour which the watershed transform method was unable to localise. This indicates an improved performance of the proposed framework when LoG edge detection method is used for the region segmentation in the step for identification of cancer regions from the cancer candidate voxels. On the other hand, in general, by use of watershed transform instead, less false positive tumours were localised.

The difference in performance of the tumour localisation using either LoG edge detection or watershed transform can be explained by how the two methods segments the regions. The LoG edge detection method finds image edges as the zero-crossings in the Laplacian filtered image. This causes detection of all image edges, weak image edges as well as strong image edges, while the watershed transform is applied to a smoothed gradient image and locates its watershed ridges or image edges where the gradients are strongest. Therefore, the edges detected and thus the regions segmented using the two methods differ.

By visual inspection of the region segmentation results from the two methods it is seen that both methods correctly segment all images for all subjects. In other words, both methods determine regions corresponding to the regions of the true tumours. However, likewise the number of segmented regions as well as their sizes differ for the two methods, the mean grey-level intensities of the regions differ as well, as the mean grey-level intensity of a region is highly

dependent on the voxels it contains. This causes the FCM clustering to assign the different regions to different clusters and thus different classification results are produced. For example, a region containing the true tumour in the ADC map could be erroneously classified into being a non-cancer region, if the region is too large or contains a too wide range of grey-level intensities because the mean grey-level intensity of the region would not be within the lowest range of the mean grey-level intensities of all regions in the ADC map, which is the criterion for classification as a cancer region.

The number of clusters set up for the FCM clustering was determined in a pretest in which the LoG edge detection and watershed transform were applied to images from three subjects, randomly chosen. Subsequently the FCM clustering was applied to the different sets of segmented regions and repeated with different numbers of clusters set up in order to determine the optimal number of clusters. This number was determined based on visual inspection of the classification results individually within the DW images, ADC maps, and K_{trans} maps. From the pretest it was concluded that optimal number of clusters varied in between the two methods and in between the different types of MR images as well. This could explain the different localisation results produced by the two methods. Moreover, as the pretest could be sensitive to the subjects used, i.e. the choice of other subjects in the pretest could result in determination of other optimal numbers of clusters, and no clear success criterion was set up for the pretest, it is unclear whether other numbers of clusters in the FCM clustering could improve the localisation performance of the two methods.

Prospectively, two ways to overcome the sensitivity with respect to the region segmentations could be a decrease in the number of clusters set up for the FCM clustering or a merge of two clusters, such that for the case of an otherwise erroneously classified region in an ADC map, regions belonging to the cluster with the lowest mean grey-level intensities and regions belonging to the cluster with the second lowest grey-level intensities would both be classified as cancer regions. Both ways would probably result in production of more false positive tumours, though.

Yet another solution could be to take advantage of the membership grades of each region. The membership grades indicate the degree to which the regions are associated to the different clusters. This information can be utilised in various ways. For now, only regions having their highest membership grade to the cluster corresponding to cancer regions are classified as cancer regions, and moreover, cancer regions within each type of image, DW image, ADC map, and K_{trans} map, must be located at same image positions, i.e. overlap, before a tumour is said to be localised. To elaborate, if a cancer region identified in the ADC map overlaps only with a cancer region identified in one of the other image types, e.g. the K_{trans} map but has no overlap with a cancer region in the DW image, no tumour is said to be localised. It may seem radically to completely discard a tumour localisation, when cancer regions in two image types overlap, and the membership grades of the corresponding region in the third image type to the various clusters should probably be taken into consideration before completely discarding the tumour localisation. For example, if the corresponding region in the DW image has a membership grade above a certain threshold for belonging to the cluster corresponding to the cancer regions, the probability for a tumour localisation might be increased, instead of simply discarding the tumour localisation.

Lastly, results for identification of cancer regions for both methods, LoG edge detection and watershed transform, could be utilised in a computation of a region-based tumour localisation probability map, in which an overlap of cancer regions resulting from both methods in all three image types, i.e. an overlap of six cancer regions, would induce tumour localisation with the

highest degree or highest probability, whereas region overlap of fewer cancer regions would induce tumour localisations of correspondingly lower degrees or probabilities. This approach could possibly be extended to take into account also the different membership grades of the different cancer regions to the cancer region cluster(s).

12.4 Implication of K_{trans}

The use of DCE-MRI in a multiparametric MRI scheme for the localisation of prostate cancer has been proved to increase the localisation sensitivity and specificity [8], for which reason the information from the K_{trans} maps computed from DCE-MRI is used in the multiparametric MRI scheme for the proposed framework for automated prostate cancer localisation.

However, from the validation results presented in Sections 11.1 and 11.2 for multiparametric MRI data with and without inclusion of K_{trans} maps, respectively, it is evident that the findings here do not correspond to the findings in the literature with regard to increased sensitivity. When adding K_{trans} information to the multiparametric MRI data in the prostate cancer localisation here performed, the number of falsely localised tumours was reduced. Taking this number as an estimate of the specificity of the solution, this indicates that the implication of inclusion of K_{trans} maps is an increased specificity, as found in the literature. But the number of correctly localised true tumours was also reduced. Taking this number as an estimate of the sensitivity of the solution, this indicates that the implication of inclusion of K_{trans} maps is a decrease in sensitivity, on the contrary to the literature.

The LoG edge detection method and the watershed transform method were both unable to correctly localise the same two specific tumours, when the multiparametric MRI data consisted of T2W images, DW images as well as both ADC and K_{trans} maps. However, when the K_{trans} information was omitted, both methods localised 9 of 11 true tumours, with the remaining two true tumours possibly localised at locations in slices adjacent to the image exactly corresponding to the key image with expert annotated image regions. This could indicate that when the K_{trans} information is omitted, both methods are able to localise all true tumours.

The image regions corresponding to these two tumours have no prominent characteristics for cancer in the K_{trans} maps, i.e. the image regions are not hyperintense as otherwise expected for cancer tissue. As a consequence these image regions are not classified cancer regions in the K_{trans} map and hence, no overlap between cancer regions identified in the DW images, ADC maps, and K_{trans} maps exists, and thus no tumour will be determined localised. Since the FCM clustering only classifies the most hyperintense regions in K_{trans} maps as cancer regions, such cases makes the differentiation of cancer regions from normal tissue regions a cumbersome task.

To recapitulate, for each true tumour a hyperintense region in the DW image and a hypointense region in the ADC map is expected to exist at a location corresponding to the location of the true tumour. The implication of the information in the K_{trans} map at this location is ambivalent. For some true tumours a corresponding hyperintense region in the K_{trans} map exists, while for other true tumours, the K_{trans} maps provide contradictory information of cancer presence. This fact should be accounted for, for instance in a region-based probability map as proposed in the end of Section 12.3. Additionally, during the voxel classification, each voxel was assigned a membership grade describing the degree of membership to each of the two

classes of prostate voxels, cancer candidate voxels or normal tissue voxels. Each membership grade provides information on the certainty of a voxel to represent the respective kind of tissue. This information could be integrated in a probability map and visualised as a voxel-by-voxel scaling of a colour according to the membership grade, thus giving a more detailed probability map.

12.5 Integration of Tumour Shape Information in the Identification of Cancer Regions

At present, no shape information is utilised in the identification of cancer regions in the proposed framework for automated prostate cancer localisation. A prostate tumour will often be a round region cf. Section 3.3, and thus it may be described as a structure resembling a blob. Vos et al. [128] have proposed a method for detection of prostate cancer which utilises shape information. For each voxel in an ADC map, a so-called blob-likeliness parameter is calculated by means of a blob detector. Other studies have proposed similar approaches in the detection of blob-like tumours for instance in the brain [129] or in breasts [130]. Common to these studies is the use of a multi-scale Hessian blob detector, able to detect blob-like structures of different sizes. The Hessian blob detector can be constructed by computation of the second derivatives of the image along each of the three dimensional directions by convolution of the image with derivatives of the Gaussian kernel. Then the Hessian matrix can be computed for each voxel enabling extraction of shape features such as the blob-likeliness which exactly can be computed from the eigenvalues and eigenvectors of the Hessian matrix.

Since the LoG filter is already applied in the proposed solution for automated prostate cancer localisation when utilising the LoG edge detection method for the identification of cancer regions, a Hessian blob detection could be implemented without major complications in order to calculate for instance the blob-likeliness of the segmented regions in the DW images, ADC maps, and K_{trans} maps.

Han et al. [131] have utilised shape information in their work of prostate cancer detection. They attempt to detect cancer tissue in transrectal ultrasound (TRUS) images with the purpose to improve the guidance during needle biopsy and suggest the use of so-called clinical knowledge-based features in addition to features of intensity and texture for the discrimination of cancer tissue and non-cancer tissue. They use such two clinical features, a location feature and a shape feature. The location feature is basically an assignment of a high cancer probability to the voxels in the area corresponding to the PZ of the prostate. In TRUS images, this is a relatively easy task, as the PZ will always be located in the lower part of the images. The shape feature is relatively simple as well. Based on an assumption that a segmented region shaped like an ellipse has a higher probability of cancer, and correspondingly that a region of irregular shape has a lower probability of cancer, they integrate the areas span by the difference between a best-fit ellipse and the actual boundary shape of a segmented region. Regions producing small integrations are very ellipse-shaped and then suspicious for cancer. Han et al. trained a support vector machine and were able to achieve a sensitivity of 96% and a specificity of 92% in the discrimination of cancer tissue and non-cancer tissue in TRUS images.

The localisation performance of the framework for automated prostate cancer localisation in the work here presented in terms of correct localisation of true tumours and decrease in the

number of false positive tumours localised could possible improve from the use of shape features of each region in addition to the already utilised region feature of mean grey-level intensity in the FCM clustering used to classify segmented regions into cancer regions and regions of normal prostate tissue.

12.6 Automated Prostate Tumour Staging Based on MRI

At present, a definite diagnosis of prostate cancer can only be confirmed by biopsies of the prostate tissue cf. Section 2.3. The localisation results of the work here presented could be useful in that procedure, guiding the biopsy needle towards regions highly suspicious for cancer.

The next step in the diagnosis procedure is to stage to tumour, i.e. to assess the tumour aggressiveness and the extent to which a cancer has developed by spreading. This is important to obtain a prognostic classification of the patient to ensure the optimal choice of treatment. At present, this prognostic classification is often based on physical examination, imaging studies, and blood tests, as outlined in Section 2.3. The tumour aggressiveness is expressed by the Gleason score, which is determined by microscopic examination of the biopsy specimens. From this, pretreatment parameters such as PSA density, number of positive needle biopsies etc. are determined and used in the prognostic classification of the patient. However, besides the sampling error associated with the systematic sampling of the prostate biopsies [27], the tumour staging based on biopsy results is complicated and erroneous as well. In a study by Noguchi et al. [132] the tumour grade estimated from biopsy results have been compared with the tumour grade estimated from prostatectomy specimens. Noguchi et al. found agreements in only 36% of the cases. This means that in the remaining 64% of the cases, the biopsy specimens caused an under- or overestimation of the Gleason score, possible resulting in an under- or overtreatment of the cancer [133]. Furthermore, Noguchi et al. found only a weak correlation among the pathological features normally used for tumour staging based on biopsy results. This indicates that the biopsy results compose a weak basis for the prostate cancer treatment planning. For a more accurate tumour staging, MRI of the prostate may prove a useful tool.

Tumour aggressiveness has been associated with signal intensity changes and detection rates in T2W images. Wang et al. [134] have found that while low-grade cancers were detected at a rate of 43%, high-grade cancers were detected at a rate of 79%. Furthermore, they were able to associate a lower muscle-to-tumour signal intensity ratio to a higher Gleason score. Important knowledge of tumour aggresiveness can thus be deduced from T2WI. ADC maps have also provided promising results as a possible marker of tumour aggressiveness. Verma and Rajesh [74] have found a negative correlation between mean ADC and Gleason score, while Hambrock et al. [73] have correlated median values of ADC with Gleason grades and were able to differentiate low-grade tumours from high-grade tumours with an AUC of 0.90.

These points all support the use of MRI in not only the detection and localisation of prostate cancer as proposed in this project at hand, but also in the procedure of tumour staging as well. Incorporation of automated tumour staging based on MRI in the clinical routine of prostate cancer management may exclude the need for biopsies at all. However, the first step should be to use the information of tumour aggressiveness to guide the biopsy needle to the most aggressive part of the tumour. In this way, an optimal basis for prognostic classification of the patient is ensured, and the right choice of treatment can thus be carried out.

Chapter 13

Conclusion

Motivated by a need for non-invasive, reproducible, and accurate localisation of prostate cancer, this project proposes a framework for automated prostate cancer localisation using multiparametric MRI as an alternative to TRUS-guided biopsies for prostate cancer diagnosis. Prostate multiparametric MRI comprises a set of both anatomical and physiological MR images representing the same prostate tissue but corresponding to different acquisition conditions, thereby reflecting or enhancing different tissue characteristics. With an increasing amount of included MRI data, the more certain or reliable the cancer localisation is expected to be. In this work, the multiparametric MRI data consists of T2W images, DW images, ADC maps, and K_{trans} maps.

The proposed framework utilises clinical knowledge of the appearance of cancer tissue in each type of MR image and consists of three steps. In a first step, the prostate is segmented from T2W images. The prostate segmentation results is transferred to the other MR image types. Then in a second step, the voxel classification, each prostate voxel is classified into being either a cancer candidate voxel or a voxel representing normal prostate tissue using a set of voxel intensity and texture features from each image type within the set of multiparametric MRI data. In a third and final step, the identification of cancer regions, the set of found cancer candidate voxels is segmented into regions by means of one of two segmentation methods, LoG edge detection and watershed transform, and based on a subsequently extracted region feature, each region is classified as a cancer region or a region most probably representing normal prostate tissue. This third step is conducted individually for each type of MR images. An image area identified as a cancer region in all types of MR images is considered a localised tumour. The two stage classification, step two and three, seeks to elevate the certainty of the localised cancer regions.

The performance of the proposed framework was validated against ground truth established by expert statements of true tumour locations. Through a two stage validation procedure, it was firstly seen that the voxel classification functions as intended. Cancer candidate voxels are found seemingly without exclusion of any true tumour voxels. Secondly, the performance of the identification of cancer regions in the set of cancer candidate voxels and thus the performance of the entire proposed framework was judged to give satisfactory tumour localisation results for most subjects.

The entire two stage validation procedure was repeated for the use of both LoG edge detection and watershed transform each applied to two different sets of multiparametric MRI data, one set composed of T2W images, DW images, and ADC maps, and another set composed of T2W images, DW images, ADC maps, and K_{trans} maps as well. The best tumour localisation in terms of correct localisation of true tumours with minimum falsely localised tumours was achieved for the use of LoG edge detection for the step of identification of cancer regions, applied to the multiparametric MRI data set composed of T2W images, DW images, ADC maps, and K_{trans} maps.

Different ways to further improve the proposed framework for automated prostate cancer localisation have been put forth. Among these is addition of features of tumour shape and anatomical position to the identification of cancer regions. Lastly, the probability or certainty of tumour localisation could be further differentiated by taking into account the information on membership grades for each cancer candidate voxel and each cancer region, respectively, for belonging to the set or cluster of cancer voxels or regions, together with the number of overlaps for cancer regions identified by the LoG edge detection method and the watershed transform method when applied to different types of MR images.

The proposed framework for automated prostate cancer localisation using multiparametric MRI is a promising tool in the management of prostate cancer. First of all it could readily help reduce the disadvantages of manual readings of the multiparametric MRI data and aid in targeting biopsy procedures. In the long term, after a few minor refinements and more research, diagnosis based on prostate cancer localisation using multiparametric MRI could possibly replace the diagnosis based on TRUS-guided biopsies.

Appendix A

Texture Features

A.1 Haralick Features

Referring to a grey-level co-ocurrence matrix (GLCM) as $P_{\Theta,d}(I_1, I_2)$, its elements denote the relative frequencies of two voxels with grey-level intensities I_1 and I_2, separated by a distance d in the direction of Θ. The number of grey-level in the image is denoted by n. In this project, the following set of texture features were extracted from the GLCMs:

Feature	Formula	A measure of the ...
Energy	$\sum_{I_1=0}^{n-1}\sum_{I_2=0}^{n-1} P(I_1,I_2)^2$	uniformity of the texture.
Entropy	$\sum_{I_1=0}^{n-1}\sum_{I_2=0}^{n-1} P(I_1,I_2)\cdot\log(P(I_1,I_2))$	randomness of the elements of $P_{\Theta,d}$.
Contrast	$\sum_{I_1=0}^{n-1}\sum_{I_2=0}^{n-1} P(I_1,I_2)\cdot n$	local intensity variation.
Homogeneity	$\sum_{I_1=0}^{n-1}\sum_{I_2=0}^{n-1} \frac{P(I_1,I_2)}{1+\text{abs}(1-I_2)}$	intensity homogeneity.
Variance	$\sum_{I_1=0}^{n-1}\sum_{I_2=0}^{n-1}((I_1-\mu_{I1})^2)\cdot P(I_1,I_2)+$ $((I_2-\mu_{I2})^2)\cdot P(I_1,I_2)$	deviations from the mean value of $P(I_1,I_2)$.
Sum Mean	$\sum_{I_1=0}^{n-1}\sum_{I_2=0}^{n-1}(I_1-I_2)+P(I_1,I_2)$	mean intensity value of pairs of voxels.
Inertia	$\sum_{I_1=0}^{n-1}\sum_{I_2=0}^{n-1}(I_1-I_2)^2\cdot P(I_1,I_2)$	how far high values of $P_{\Theta,d}$ are from the diagonal.
Cluster Shade	$\sum_{I_1=0}^{n-1}\sum_{I_2=0}^{n-1}(I_1+I_2-\mu_1-\mu_2)^3\cdot P(I_1,I_2)$	skewness of $P_{\Theta,d}$.
Cluster Tendency	$\sum_{I_1=0}^{n-1}\sum_{I_2=0}^{n-1}(I_1+I_2-\mu_1-\mu_2)^4\cdot P(I_1,I_2)$	skewness of $P_{\Theta,d}$.
Max Probability	$\max P(I_1,I_2)$	maximum value of $P_{\Theta,d}$.
Inverse Variance	$\sum_{I_1=0}^{n-1}\sum_{I_2=0}^{n-1}\frac{P(I_1,I_2)}{(I_1-I_2)^2}$	intensity homogeneity.

Table A.1: The set of Haralick features extracted from the grey-level co-ocurrence matrices in this project.

A.2 Features from Grey-Level Run Length Matrices

For a given volume, the grey-level run length matrix (GLRLM) $\mathbf{P}$ contains the elements $P(i,j)$ representing the number of runs with voxels of grey-level intensity equal to i and length of run j along a given direction Θ [35]. From $\mathbf{P}$ many features can be extracted. Among the GLRLM features in Table A.2, Galloway [118] derived the first five features, Chu et al. [135] suggested the following features which unlike the features suggested by Galloway also incorporate intensity

information. Finally, Dasarathy and Holder [136] suggested the last four features, which all are joint statistical measures of run length and grey-level intensity.

M is the number of grey-levels in the image, N denotes the maximum run length, n_r is the total number of runs and n_p is the number of pixels in the image. The grey-level run-number vector is $p_g(i) = \sum_{j=1}^{N} p(i,j)$, and finally the run-length run-number vector is $p_r(j) = \sum_{i=1}^{M} p(i,j)$.

Feature	Formula	A measure of the ..
Short Run Emphasis	$\frac{1}{n_r}\sum_{j=1}^{N}\frac{p_r(j)}{j^2}$	distribution of short runs and is expected large for fine textures.
Long Run Emphasis	$\frac{1}{n_r}\sum_{j=1}^{N} p_r(j)\cdot j^2$	distribution of short runs and is expected large for coarse textures.
Grey-Level Non-Uniformity	$\frac{1}{n_r}\sum_{i=1}^{M} p_g(i)^2$	similarity of grey-level values in the image and is expected small for homogeneous images.
Run Length Non-Uniformity	$\frac{1}{n_r}\sum_{j=1}^{N} p_r^2$	similarity of the length of runs in the image and is expected small if the run lengths are alike in the image.
Run Percentage	$\frac{n_r}{n_p}$	homogeneity and the distribution of runs of an image in a specific direction.
Low Grey-Level Run Emphasis	$\frac{1}{n_r}\sum_{i=1}^{M}\frac{p_g(i)}{i^2}$	distribution of grey-level values and is expected large for images with low grey-level values.
High Grey-Level Run Emphasis	$\frac{1}{n_r}\sum_{i=1}^{M} p_g(i)\cdot i^2$	distribution of grey-level values and is expected large for images with high grey-level values.
Short Run Low Grey-Level Emphasis	$\frac{1}{n_r}\sum_{i=1}^{M}\sum_{j=1}^{N}\frac{p(i,j)}{i^2\cdot j^2}$	joint distribution of short runs and low grey-level values.
Short Run High Grey-Level Emphasis	$\frac{1}{n_r}\sum_{i=1}^{M}\sum_{j=1}^{N}\frac{p(i,j)\cdot i^2}{j^2}$	joint distribution of short runs and high grey-level values.
Long Run Low Grey-Level Emphasis	$\frac{1}{n_r}\sum_{i=1}^{M}\sum_{j=1}^{N}\frac{p(i,j)\cdot j^2}{i^2}$	joint distribution of long runs and low grey-level values.
Long Run High Grey-Level Emphasis	$\frac{1}{n_r}\sum_{i=1}^{M}\sum_{j=1}^{N} p(i,j)\cdot j^2\cdot i^2$	joint distribution of long runs and high grey-level values.

Table A.2: The set of GLRLM features applied in this project.

Bibliography

[1] M. Richards, "The size of the prize for earlier diagnosis of cancer in england," *British Journal of Cancer*, vol. 101, pp. 125–129, 2009.

[2] H. Jensen, A. Nissen, and P. Vedsted, "Quality deviations in cancer diagnosis: prevalence and time to diagnosis in general practice," *British Journal of General Practice*, vol. 64, February 2014.

[3] S. F. Shariat and C. G. Roehrborn, "Using biopsy to detect prostate cancer," *Reviews in Urology*, vol. 10, no. 4, pp. 262–280, 2008.

[4] J. C. Presti, "Prostate biopsy: Current status and limitations," *Reviews in Urology*, vol. 9, no. 3, pp. 93–98, 2007.

[5] J. Feinmann, "This machine can defer prostate surgery for years. yet worryingly few british men have access to one," May 2012. Accessed: 2014-03-20.

[6] H. Huisman, P. Vos, G. Litjens, T. Hambrock, and J. Barentsz, "Computer aided detection of prostate cancer using T2, DWI and DCE MRI: Methods and clinical applications," in *Prostate Cancer Imaging*, pp. 4–14, 2010.

[7] S. W. T. P. Heijmink, J. J. Fütterer, S. S. Strum, W. J. G. Oyen, F. Frauscher, J. A. Witjes, and J. O. Barentsz, "State-of-the-art uroradiologic imaging in the diagnosis of prostate cancer," *Acta Oncologica*, vol. 50, no. 1, pp. 25–38, 2011.

[8] C. M. Hoeks, J. O. Barentsz, T. Hambrock, D. Yakar, D. M. Somford, S. W. Heijmink, T. W. Scheenen, P. C. Vos, H. Huisman, I. M. van Oort, J. A. Witjes, A. Heerschap, and J. J. Fütterer, "Prostate cancer: Multiparametric MR imaging for detection, localization, and staging," *Radiology*, vol. 261, no. 1, pp. 46–66, 2011.

[9] M. Seitz, A. Shukla-Dave, A. Bjartell, K. Touijer, A. Sciarra, P. J. Bastian, C. Stief, H. Hricak, and A. Graser, "Functional magnetic resonance imaging in prostate cancer," *European Urology*, vol. 55, no. 4, pp. 801–814, 2009.

[10] R. T. Gupta, C. R. Kauffman, T. J. Polascik, S. S. Taneja, and A. B. Rosenkrantz, "The state of prostate MRI in 2013," *Oncology*, vol. 27, no. 4, pp. 262–270, 2013.

[11] J. Dineley, "MRI enhances radiation treatment," *Public Service Review: European Science & Technology*, pp. 17–19, December 2013.

[12] G. Engholm, J. Ferlay, N. Christensen, T. Johannesen, S. Khan, J. Køtlum, M. Milter, E., E. Pukkala, and H. Storm, "NORDCAN: cancer incidence, mortality, prevalence and survival in the nordic countries." `http://www.ancr.nu`, April 2013.

[13] "Treatment choices for men with early-stage prostate cancer." `http://www.cancer.gov/cancertopics/treatment/prostate/understanding-prostate-cancer-treatment/page3`. Accessed: 2014-05-08.

[14] O. W. Petersen, M. E. Matthiessen, and K. Poulsen, *Human Anatomi: Hoved og hals*. Copenhagen N, Denmark: F.A.D.L., 1 ed., 2001.

[15] American Cancer Society, "Prostate cancer," March 2014. Accessed: 2014-04-20.

[16] M. Amin, A. Khalid, N. Tazeen, and M. Yasoob, "Zonal anatomy of prostate," *Annals of Internal Medicine*, vol. 16, no. 3, pp. 138–141, 2010.

[17] Canadian Cancer Society, "Anatomy and physiology of the prostate." `http://www.cancer.ca/en/cancer-information/cancer-type/prostate/anatomy-and-physiology/?region=on`. Accessed: 2014-02-19.

[18] Urology Match, "Basic principles: Prostate anatomy." `http://www.urologymatch.com/ProstateAnatomy.htm`. Accessed: 2014-02-21.

[19] J. E. McNeal, E. A. Redwine, F. S. Freiha, and T. A. Stamey, "Zonal distribution of prostatic adenocarcinoma: Correlation with histologic pattern and direction of spread," in *The American Journal of Surgical Pathology*, vol. 12, pp. 897–906, December 1988.

[20] J. Nordling, M. Rørth, G. Hansen-Nord, and F. Klamer, "Prostatakræft," in *Lægehåndbogen*, 2013.

[21] P. Lichtenstein, N. V. Holm, P. K. Verkasalo, A. Iliadou, J. Kaprio, M. Koskenvuo, E. Pukkala, A. Skytthe, and K. Hemminki, "Environmental and heritable factors in the causation of cancer - analyses of cohorts of twins from sweden, denmark, and finland," *The New England Journal of Medicine*, vol. 343, no. 2, pp. 79–84, 2000.

[22] S. Verma, B. Turkbey, N. Muradyan, A. Rajesh, F. Cornud, M. A. Haider, P. L. Choyke, and M. Harisinghani, "Overview of dynamic constrast-enhanced MRI in prostate cancer diagnosis and management," *American Journal of Roentgenology*, vol. 198, no. 6, pp. 1277–1288, 2012.

[23] American Cancer Society, "How is prostate cancer staged?," March 2014.

[24] National Cancer Institute, "Cancer staging." `http://www.cancer.gov/cancertopics/factsheet/Detection/staging`. Accessed: 2014-05-13.

[25] J. O. Barentsz, J. Richenberg, R. Clements, P. Choyke, S. Verma, G. Villeirs, O. Rouviere, V. Logager, and J. J. Futterer, "ESUR prostate MR guidelines 2012," *European Radiology*, vol. 22, no. 4, pp. 746–757, 2012.

[26] A. El-Hakim and S. Moussa, "CUA guidelines on prostate biopsy methodology," *Canadian Urological Association Journal*, vol. 4, pp. 89–94, April 2010.

[27] E. C. Serefoglu, S. Altinova, N. S. Ugras, E. Akincioglu, E. Asil, and D. Balbay, "How reliable is 12-core prostate biopsy procedure in the detection of prostate cancer?," *Canadian Urological Association Journal*, vol. 7, pp. 293–298, May 2013.

[28] Weiss Memorial Hospital, "Prostate biopsy." `http://www.weisshospital.com/medical-services/clinical-programs/robotic-prostate-surgery/prostate-biopsy.aspx`. Accessed: 2014-04-12.

[29] R. K. Nam, R. Saskin, Y. Lee, Y. Liu, C. Law, L. H. Klotz, D. A. Loblaw, J. Trachtenberg, A. Stanimirovic, A. E. Simor, A. Seth, D. R. Urbach, and S. A. Narodt, "Increasing hospital admission rates for urological complications after transrectal ultrasound guided prostate biopsy," *The Journal of Urology*, vol. 183, pp. 963–969, March 2010.

[30] E. Özden abd Yakup Bostanci, K. Y. Yakupoglu, E. Akdeniz, A. F. Yilmaz, N. Tulek, and S. Sankaya, "Incidence of acute prostatitis caused by extended-spectrum β-lactamase-producing escherichia coli after transrectal prostate biopsy," *The Journal of Urology*, vol. 74, pp. 119–123, July 2009.

[31] R. Raaijkmakers, W. J. Kirkels, M. J. Roobol, M. F. Wildhagen, and F. H. Schröder, "Complication rates and risk factors of 5802 transrectal ultrasound-guided sextant biopsies of the prostate within a population-based screening program," *Urology*, vol. 60, pp. 826–830, November 2002.

[32] N. Fleshner and L. Klotz, "Role of 'saturation biopsy' in the detection of prostate cancer among difficult diagnosic cases," *Urology*, vol. 60, no. 1, pp. 93–97, 2002.

[33] T. Penzkofer and C. M. Tempany-Afdhal, "Prostate cancer detection and diagnosis: The role of MR and its comparison with other diagnostic modalities - a radiologist's perspective," *NMR in Biomedicine*, vol. 27, no. 1, pp. 3–15, 2014.

[34] R. Clements, "Ultrasound of prostate cancer," *European Radiology*, vol. 11, pp. 2119–2125, 2001.

[35] D.-H. Xu, A. S. Kurani, J. D. Furst, and D. S. Raicu, "Run-length encoding for volumetric texture," tech. rep., Intelligent Multimedia Processing Laboratory, School of Computer Science, Telecommunications, and Information Systems, DePaul University, Chicago, Illinois.

[36] S. Kadoury, P. Yan, S. Xu, N. Glossop, P. Choyke, B. Turkbey, P. Pinto, B. J. Wood, and J. Kruecker, "Realtime TRUS/MRI fusion targeted-biopsy for prostate cancer: A clinical demonstration of increased positive biopsy rates," *Lecture Notes in Computer Science*, vol. 6367, pp. 52–62, 2010.

[37] F. Cornud, L. Brolis, N. B. Delongchamps, D. Portalez, B. Malavaud, R. Renard-Penna, and P. Mozer, "TRUS-MRI image registration: a paradigm shift in the diagnosis of significant prostate cancer," *Abdominal Imaging*, vol. 38, pp. 1447–1463, July 2013.

[38] Y. Mazaheri, A. Shukla-Dave, A. Muellner, and H. Hricak, "MRI of the prostate: Clinical relevance and emerging applications," *Journal of Magnetic Resonance Imaging*, vol. 33, no. 2, pp. 258–274, 2011.

[39] G. A. Sonn, S. Natarajan, D. J. A. Margolis, M. MacAiran, P. Lieu, J. Huang, F. J. Dorey, and L. S. Marks, "Targeted biopsy in the detection of prostate cancer using an office based magnetic resonance ultrasound fusion device," *The Journal of Urology*, vol. 189, no. 1, pp. 86–92, 2013.

[40] B. K. Park, J. W. Park, S. Y. Park, C. K. Kim, H. M. Lee, S. S. Jeon, S. I. Seo, B. C. Jeong, and H. Y. Choi, "Prospective evaluation of 3-T MRI performed before initial transrectal ultrasound-guided prostate biopsy in patients with high prostate-specific antigen and no previous biopsy," *Genitourinary Imaging*, vol. 197, pp. 876–881, November 2011.

[41] R. R. Carlton and A. M. Adler, *Principles of Radiographic Imaging: An Art and a Science*. New York, USA: Delmar, 4 ed., 2006.

[42] J. T. Bushberg, J. A. Seibert, E. M. L. Jr., and J. M. Boone, *The Essential Physics of Medical Imaging*. Philadelphia, PA, USA: Lippincott Williams & Wilkins, 2 ed., 2002.

[43] "Basic nuclear magnetic resonance." `http://www.simplyphysics.com/page2_1.html`. Accessed: 2014-05-08.

[44] D. W. McRobbie, E. A. Moore, M. J. Graves, and M. R. Prince, *MRI From Picture to Proton*. New York, USA: Cambridge University Press, 2 ed., 2006.

[45] D. Hoa, "Spin echo, TR, TE." `http://www.imaios.com/en/e-Courses/e-MRI/MRI-signal-contrast/Spin-echo-TR-TE`. Accessed: 2014-05-10.

[46] R. H. Hashemi, W. G. B. Jr, and C. J. Lisanti, *MRI: The Basics*. Philadelphia, USA: Lippincott Williams & Wilkins, 3 ed., 2010.

[47] "Relaxation (NMR)." `http://en.wikipedia.org/wiki/T2*`. Accessed: 2014-05-21.

[48] E. M. Charles-Edwards and N. M. deSouza, "Diffusion-weighted magnetic resonance imaging and its application to cancer," *Cancer Imaging*, vol. 6, no. 1, pp. 135–143, 2006.

[49] D.-M. Koh, T. Takahara, Y. Imai, and D. J. Collins, "Practical aspects of assessing tumors using clinical diffusion-weighted imaging in the body," *Magnetic Resonance in Medical Science*, vol. 6, no. 4, pp. 211–224, 2007.

[50] D.-M. Koh and D. J. Collins, "Diffusion-weighted MRI in the body: Applications and challenges in oncology," *American Journal of Roentgenology*, vol. 188, no. 6, pp. 1622–1635, 2007.

[51] A. R. Padhani, G. Liu, D. Mu-Koh, T. L. Chenevert, H. C. Thoeny, T. Takahara, A. Dzik-Jurasz, B. D. Ross, M. V. Cauteren, D. Collins, D. A. Hammoud, G. J. Rustin, B. Taouli, and P. L. Choyke, "Diffusion-weighted magnetic resonance imaging as a cancer biomarker: Consensus and recommendations," *Neoplasia*, vol. 11, pp. 102–125, February 2009.

[52] T. Tamada, T. Sone, Y. Jo, A. Yamamoto, and K. Ito, "Diffusion-weighted MRI and its role in prostate cancer," *NMR in Biomedicine*, vol. 27, no. 1, pp. 25–38, 2014.

[53] J. G. Korporaal, "Dynamic contrast-enhanced (DCE) imaging for tumor delineation in prostate cancer," September 2011.

[54] J. Jones and J. R. Ballinger, "Diamagnetism." `http://radiopaedia.org/articles/diamagnetism`. Accessed: 2014-05-09.

[55] J. Jones and J. R. Ballinger, "Paramagnetism." `http://radiopaedia.org/articles/paramagnetism`. Accessed: 2014-05-09.

[56] P. S. Tofts, G. Brix, D. L. Buckley, J. L. Evelhoch, E. Henderson, M. V. Knopp, H. B. Larsson, T.-Y. Lee, N. A. Mayr, G. J. Parker, R. E. Port, J. Taylor, and R. M. Weisskoff, "Estimating kinetic parameters from dynamic contrast-enhanced T1-weighted MRI of a diffusable tracer: Standardized quantities and symbols," *Journal of Magnetic Resonance Imaging*, vol. 10, no. 3, pp. 223–232, 1999.

[57] P. S. Tofts, "T1-weighted DCE imaging concepts: Modelling, acquisition and analysis," *MAGNETOM Flash*, vol. 3, pp. 30–39, 2010.

[58] J. Scheidler, H. Hricak, D. B. Vigneron, K. K. Yu, D. L. Sokolov, L. R. Huang, C. J. Zaloudek, S. J. Nelson, P. R. Carroll, and J. Kurhanewicz, "Prostate cancer: Localization with three-dimensional proton MR spectroscopic imaging - clinicopathologic study," *Radiology*, vol. 213, pp. 473–480, November 1999.

[59] C. Tempany and F. Franco, "Prostate MRI: Update and current roles," *Applied Radiology*, vol. 41, pp. 17–22, March 2012.

[60] K. Coyne, "MRI: a guided tour." http://www.magnet.fsu.edu/education/tutorials/magnetacademy/mri/fullarticle.html. Accessed: 2014-05-10.

[61] M. E. T. O. M. D. Exhibition., "Matrix MRI coil." http://www.medicalexpo.com/prod/toshiba-medical-systems/matrix-mri-coils-thorax-abdomen-70354-428397.html. Accessed: 2014-05-11.

[62] W. K. OH, M. Hurwitz, A. V. D'Amico, J. P. Richie, and P. W. Kantoff, "Neoplasms of the prostate," in *Holland-Frei Cancer Medicine*, (Hamilton, Ontario, Canada), 2000.

[63] K. Yoshimitsu, K. Kiyoshima, H. Irie, T. Tajima, Y. Asayama, M. Hirakawa, K. Ishigami, S. Naito, and H. Honda, "Usefulness of apparent diffusion coefficient map in diagnosing prostate carcinoma: Correlation with stepwise histopathology," *Journal of Magnetic Resonance Imaging*, vol. 27, no. 1, 2008.

[64] K. Kitajima, Y. Kaji, Y. Fukabori, K. ichiro Yoshida, N. Suganuma, and K. Sugimura, "Prostate cancer detection with 3 T MRI: Comparison of diffusion-weighted imaging and dynamic contrast-enhanced MRI in combination with T2-weighted imaging," *Journal of Magnetic Resonance Imaging*, vol. 31, no. 3, pp. 625–631, 2010.

[65] D. L. Langer, T. H. van der Kwast, A. J. Evans, J. Trachtenberg, B. C. Wilson, and M. A. Haider, "Prostate cancer detection with multi-parametric MRI: Logistic regression analysis of quantitative T2, diffusion-weighted imaging, and dynamic contrast-enhanced MRI," *Journal of Magnetic Resonance Imaging*, vol. 30, no. 2, pp. 327–334, 2009.

[66] Y. Mazaheri, A. Shukla-Dave, H. Hricak, S. W. Fine, J. Zhang, G. Inurrigarro, C. S. Moskowitz, N. M. Ishill, V. E. Reuter, K. Touijer, K. L. Zakian, and J. A. Koutcher, "Prostate cancer: Identification with combined diffusion-weighted MR imaging and 3D 1H MR spectroscopic imaging-correlation with pathologic findings," *Radiology*, vol. 246, no. 2, pp. 480–488, 2008.

[67] G. Jager, E. Ruijter, C. van de Kaa, J. de la Rosette, G. Oosterhof, J. Thornbury, S. Ruijs, and J. Barentsz, "Dynamic turboflash subtraction technique for contrast-enhanced MR imaging of the prostate: correlation with histopathologic results," *Radiology*, vol. 203, no. 3, pp. 645–52, 1997.

[68] C. Kim, B. Park, and B. Kim, "Localization of prostate cancer using 3T MRI: comparison of T2-weighted and dynamic contrast-enhanced imaging," *Journal of Computer Assisted Tomography*, vol. 30, no. 1, pp. 7–11, 2006.

[69] K. Ogura, S. Maekawa, K. Okubo, Y. Aoki, T. Okada, K. Oda, Y. Watanabe, C. Tsukayama, and Y. Arai, "Dynamic endorectal magnetic resonance imaging for local staging and detection of neurovascular bundle involvement of prostate cancer: correlation with histopathologic results," *Urology*, vol. 57, no. 4, pp. 721–726, 2006.

[70] N. B. Delongchamps, M. Rouanne, T. Flam, F. Beuvon, M. Liberatore, M. Zerbib, and F. Cornud, "Multiparametric magnetic resonance imaging for the detection and localization of prostate cancer: combination of T2-weighted, dynamic contrast-enhanced and diffusion-weighted imaging," *BJU International*, vol. 107, pp. 1411–1418, May 2010.

[71] T. Yoshizako, A. Wada, T. Hayashi, K. Uchida, M. Sumura, N. Uchida, H. Kitagaki, and M. Igawa, "Usefulness of diffusion-weighted imaging and dynamic contrast-enhanced magnetic resonance imaging in the diagnosis of prostate transition-zone cancer," *Acta Radiologica*, vol. 49, no. 10, pp. 1207–1213, 2008.

[72] H. Hricak, G. C. Dooms, J. E. McNeal, A. S. Mark, M. Marotti, A. Avallone, M. Pelzer, E. C. Proctor, and E. A. Tanagho, "MR imaging of the prostate gland: Normal anatomy," *American Journal of Roentgenology*, vol. 148, no. 1, pp. 51–58, 1987.

[73] T. Hambrock, D. M. Somford, H. J. Huisman, I. M. van Oort, J. A. Witjens, C. A. H. van de Kaa, T. Scheenen, and J. O. Barentsz, "Relationship between apparent diffusion coefficients at 3.0-T MR imaging and gleason grade in peripheral zone prostate cancer," *Radiology*, vol. 259, no. 2, pp. 453–461, 2011.

[74] S. Verma and A. Rajesh, "A clinically relevant approach to imaging prostate cancer: Review," *American Journal of Roentgenology*, vol. 196, no. 3, pp. S1–S10, 2011.

[75] D. M. McDonald and P. L. Choyke, "Imaging of angiogenesis: from microscope to clinic," *Nature Medicine*, vol. 9, pp. 713–725, June 2003.

[76] L. Boesen, N. NÃ¸rgaard, E. Chabanova, V. LÃ¸gager, I. Balslev, K. Mikines, and H. Thomsen, "Early experience with multiparametric MRI-targeted biopsies under visual TRUS guidance in patients suspicious of prostate cancer undergoing repeated biopsy," *Scandinavian Journal of Urology and Nephrology*.

[77] MINC Tool Kit, *version 1.0.01*. Montreal Neurological Institute, 3801 University St., Montreal, Quebec, Canada.: McConnell Brain Imaging Center, 2014.

[78] A. M. Tahmasebi, R. Sharifi, H. K. Agarwal, B. Turkbey, M. Bernardo, P. Choyke, P. Pinto, B. Wood, and J. Kruecker, "A statistical model-based technique for accounting for prostate gland deformation in endorectal coil-based MR imaging," in *34th Annual International Conference of the IEEE EMBS*, (San Diego, California USA), pp. 5412–5415, 2012.

[79] L. C. Carbo, M. A. Haider, and I. S. Yetik, "Supervised prostate cancer segmentation with multispectral MRI incorporating location information," in *2011 IEEE International Symposium on Biomedical Imaging: From Nano to Macro*, (Chigago, IL, USA), pp. 1496–1499, 2011.

[80] Y. Artan, M. A. Haider, D. L. Langer, T. H. van der Kwast, A. J. Evans, and Y. Yang, "Prostate cancer localization with multispectral MRI using cost-sensitive support vector machines and conditional random fields," *IEEE Transactions on Image Processing*, vol. 19, no. 9, pp. 2444–2455, 2010.

[81] S. Ozer, D. L. Langer, X. Liu, M. A. Haider, T. H. van der Kwast, A. J. Evans, Y. Yang, M. N. Wernick, and I. S. Yetik, "Supervised and unsupervised methods for prostate cancer segmentation with multispectral MRI," *Medical Physics*, vol. 37, no. 4, pp. 1873–1883, 2010.

[82] E. Niaf, O. Rouvière, F. Mège-Lechevallier, F. Bratan, and C. Lartizien, "Computer-aided diagnosis of prostate cancer in the peripheral zone using multiparametric MRI," *Physics in Medicine and Biology*, vol. 57, no. 12, pp. 3833–3851, 2012.

[83] Y. Artan, M. A. Haider, and I. S. Yetik, "Prostate cancer segmentation using multispectral random walks," in *Prostate Cancer Imaging 2010*, (New York), 2010.

[84] X. Liu, M. A. Haider, and I. S. Yetik, "Automated prostate cancer segmentation with MRI without the need of manually extracted peripheral zone," in *2011 IEEE International Symposium on Biomedical Imaging: From Nano to Macro*, pp. 2099–2102.

[85] S. Ruan, S. Lebonvallet, A. Merabet, and J.-M. Constans, "Tumor segmentation from a multispectral MRI images by using support vectors machine classification," in *4th IEEE International Symposium on Biomedical Imaging: From Nano to Macro*, pp. 1236–1239, 2007.

[86] G. Litjens, O. Debats, J. Barentsz, N. Karssemeijer, and H. Huisman, "Computer-aided detection of prostate cancer in MRI," *IEEE Transactions on Medical Imaging*, vol. 35, no. 5, pp. 1083–1092, 2014.

[87] G. Litjens, P. Vosa, J. Barentsza, N. Karssemeijer, and H. Huisman, "Automatic computer aided detection of abnormalities in multi-parametric prostate MRI," in *Medical Imaging 2011: Computer-Aided Diagnosis* (R. M. Summers and B. van Ginneken, eds.), 2011.

[88] G. Litjens, R. Toth, W. van de Ven, C. Hoeks, S. Kerkstra, B. van Ginneken, G. Vincent, G. Guillard, N. Birbeck, J. Zhang, R. Strand, F. Malmberg, Y. Ou, C. Davatzikos, M. Kirschner, F. Jung, J. Yuan, W. Qiu, Q. Gao, P. E. Edwards, B. Maan, F. van der Heijden, S. Ghose, J. Mitra, J. Dowling, D. Barratt, H. Huisman, and A. Madabhushi, "Evaluation of prostate segmentation algorithms for MRI: The PROMISE12 challenge," *Medical Image Analysis*, vol. 18, no. 2, pp. 359–373, 2014.

[89] A. S. Korsager, U. L. Stephansen, J. Carl, and L. R. Østergaard, "The use of an active appearance model for automated prostate segmentation in magnetic resonance," *Acta Oncologica*, vol. 52, no. 7, pp. 1374–1377, 2013.

[90] T. F. Cootes, G. J. Edwards, and C. J. Taylor, "Active appearance models," in *IEEE Transactions on Pattern Analysis and Machine Intelligence*, pp. 484–498, Springer, 1998.

[91] L. R. Dice, "Measures of the amount of ecologic association between species," *Ecology*, vol. 26, no. 3, pp. 297–302, 1945.

[92] S. Klein, U. A. van der Heide, I. M. Lips, M. van Vulpen, M. Staring, and J. P. W. Pluim, "Automatic segmentation of the prostate in 3D MR images by atlas matching using localized mutual information," *The American Association of Physicists in Medicine*, vol. 35, no. 4, pp. 1407–1417, 2008.

[93] A. S. Korsager, V. Fortunati, F. van der Lijn, J. Carl, W. Niessen, L. R. Østergaard, and T. van Walsum, "The use of atlas registration and graph cuts for prostate segmentation in magnetic resonance images," *Submitted Manuscript*, 2014.

[94] M. Cabezas, A. Oliver, X. Llado, J. Freixenet, and M. B. Cuadra, "A review of atlas-based segmentation for magnetic resonance brain images," *Computer Methods and Programs in Biomedicine*, vol. 104, no. 3, pp. 158–177, 2011.

[95] S. Kleiny, M. Staringy, K. Murphy, M. A. Viergever, and J. P. W. Pluim, "elastix: A toolbox for intensity-based medical image registration," *IEEE Transactions on Medical Imaging*, vol. 29, no. 1, pp. 196–205, 2010.

[96] P. Aljabar, R. Heckemann, A. Hammers, J. Hajnal, and D. Rueckert, "Multi-atlas based segmentation of brain images: Atlas selection and its effect on accuracy," *NeuroImage*, vol. 46, no. 3, pp. 726–738, 2009.

[97] L. Dickinson, H. U. Ahmed, C. Allen, J. O. Barentsz, B. Carey, J. J. Futterer, S. W. Heijmink, P. J. Hoskin, A. Kirkham, A. R. Padhani, R. Persad, P. Puech, S. Punwani, A. S. Sohaib, B. Tombal, A. Villers, J. van der Meulen, and M. Emberton, "Magnetic

resonance imaging for the detection, localisation, and characterisation of prostate cancer: Recommendations from a european consensus meeting," *European Urology*, vol. 59, pp. 477–494, April 2011.

[98] E. Outwater, M. Schiebler, J. Tomaszewski, M. Schnall, and H. Kressel, "Mucinous carcinomas involving the prostate: atypical findings at MR imaging," *Journal of Magnetic Resonance Imaging*, vol. 2, no. 5, pp. 597–600, 1992.

[99] D. Lv, X. Guo, X. Wang, J. Zhang, and J. Fang, "Computerized characterization of prostate cancer by fractal analysis in MR images," *Journal of Magnetic Resonance*, vol. 30, no. 1, pp. 161–168, 2009.

[100] G. Castellano, L. Bonilha, L. Li, and F. Cendes, "Texture analysis of medical images," *Clinical Radiology*, vol. 59, no. 12, pp. 1061–1069, 2004.

[101] L. Tesar, D. Smutek, A. Shimizu, and H. Kobatake, "3d extension of haralick texture features for medical image analysis," in *Proceedings of the Fourth IASTED International Conference on Signal Processing, Pattern Recognition, and Applications*, pp. 350–355, 2007.

[102] A. K. Mohanty, S. Beberta, and S. K. Lenka, "Classifying benign and malignant mass using GLCM and GLRLM based texture features from mammogram," *International Journal of Engineering Research and Applications*, vol. 1, no. 3, pp. 687–693, 2011.

[103] J. Loose, M. T. Harza, H. Laue, T. Twellmann, U. Bick, M. Rominger, H. K. Hahn, and H.-O. Peitgen, "Assessment of texture analysis on DCE-MRI data for the differentiation of breast tumor lesions," in *Medical Imaging 2009: Computer-Aided Diagnosis*, vol. 7260, 2009.

[104] A. Kassner and R. Thornhill, "Texture analysis: A review of neurologic MR imaging applications," *American Journal of Neuroradiology*, vol. 31, no. 5, pp. 809–816, 2010.

[105] A. Madabhushi, M. D. Feldman, D. N. Metaxas, J. Tomaszeweski, and D. Chute, "Automated detection of prostatic adenocarcinoma from high-resolution ex vivo MRI," *IEEE Transactions on Medical Imaging*, vol. 24, no. 12, pp. 1611–1625, 2005.

[106] D. Duda, M. Kretowski, R. Mathieu, R. de Crevoisier, and J. Bezy-Wendling, "Multi-image texture analysis in classification of prostatic tissues from MRI. preliminary results," in *Information Technologies in Biomedicine* (E. Piętka, J. Kawa, and W. Wieclawek, eds.), Springerlink, 2014.

[107] Y. C. Gong and M. Brady, "Texture based segmentation of breast DCE-MRI," in *Digital Mammography* (E. A. Krupinski, ed.), Springerlink, 2008.

[108] M. Pietikäinen, A. Hadid, G. Zhao, and T. Ahonen, *Computer Vision Using Local Binary Patterns*. New York: Springer, 2011.

[109] S. E. Viswanath, M. Rosen, and A. Madabhushi, "A consensus embedding approach for segmentation of high resolution in vivo prostate magnetic resonance imagery," in *SPIE Medical Imaging*, vol. 6915, (San Diego, CA), 2008.

[110] M. Radhakrishnan and T. Kuttiannan, "Comparative analysis of feature extraction methods for the classification of prostate cancer from TRUS medical images," *International Journal of Computer Science Issues*, vol. 9, no. 2, pp. 171–179, 2012.

[111] N. Aggarwal and R. Agrawal, "First and second order statistics features for classification of magnetic resonance brain images," *Journal of Signal and Information Processing*, vol. 3, no. 2, pp. 146–153, 2012.

[112] R. M. Haralick, K. Shanmugam, and I. Dinstein, "Textural features for image classification," *IEEE Transactions on Systems, Man, and Cybernetics*, vol. 3, pp. 610–621, November 1973.

[113] T. Ojala, M. Pietikainen, and D. Harwood, "A comparative study of texture measures with classification based on featured distributions," *Pattern Recognition*, vol. 29, no. 1, pp. 51–59, 1996.

[114] X. Tang, "Texture information in run-length matrices," *IEEE Transactions on Image Processing*, vol. 7, no. 11, pp. 1602–1609, 1998.

[115] W. Xinli, F. Albregtsen, and B. Foyn, "Texture features from gray level gap length matrix," in *MVA IAPR Workshop on Machine Vision Applications*, pp. 375–378.

[116] H. Wibawanto, A. Susanto, T. S. Widodo, and S. M. Tjokronegoro, "Discriminating cystic and non cystic mass using GLCM and GLRLM-based texture features," *International Journal of Electronic Engineering Research*, vol. 2, no. 4, pp. 569–580, 2010.

[117] J. S. Weszka, C. R. Dyer, and A. Rosenfeld, "A comparative study of texture measures for terrain classification," *IEEE Transactions on Systems, Man, and Cybernetics*, vol. SMC-6, no. 4, pp. 269–285, 1976.

[118] M. M. Galloway, "Texture analysis using gray level run lengths," *Computer Graphics and Image Processing*, vol. 4, no. 2, pp. 172–179, 1975.

[119] W. Chen, M. L. Giger, and U. Bick, "A fuzzy c-means (FCM)-based approach for computerized segmentation of breast lesions in dynamic contrast-enhanced MR images," *Academic Radiology*, vol. 13, no. 1, pp. 63–72, 2006.

[120] R. O. Duda, P. E. Hart, and D. G. Stork, *Pattern Classification.* New York: John Wiley and Sons, 2 ed., 2001.

[121] Y.-L. Huang and D.-R. Chen, "Watershed segmentation for breast tumor in 2-D sonography," *Ultrasound in Medicine & Biology*, vol. 30, pp. 625–632, May 2004.

[122] Y. Cui, Y. Tan, B. Zhao, L. Liberman, R. Parbhu, J. Kaplan, M. Theodoulou, C. Hudis, and L. H. Schwartz, "Malignant lesion segmentation in contrast-enhanced breast MR images based in the marker-controlled watershed," *Medical Physics*, vol. 36, pp. 4359–4369, October 2009.

[123] R. C. Gonzalez and R. E. Woods, *Digital Image Processing.* New Jersey: Prentice Hall, 2 ed., 2001.

[124] W. Bieniecki, "Oversegmentation avoidance in watershed-based algorithms for color images," in *Proceedings of the International Conference on Modern Problems of Radio Engineering, Telecommunications and Computer Science*, IEEE.

[125] I. M. Lips, U. A. van der Heide, K. Haustermans, E. N. van Lin, F. Pos, S. P. Franken, A. N. Kotte, C. H. van Gils, and M. van Vulpen, "Single blind randomized phase III trial to investigate the benefit of a focal lesion ablative microboost in prostate cancer (FLAME-trial): study protocol for a randomized controlled trial," *Trials*, vol. 12, no. 255, 2011.

[126] Y. Chi, H. Ho, Y. M. Law, Q. Tian, H. J. Chen, K. J. Tay, and J. Liu, "A compact method for prostate zonal segmentation on multi-parametric MRIs," in *Medical Imaging 2014: Image-Guided Procedures, Robotic Interventions, and Modeling* (Z. R. Yaniv and D. R. Holmes, eds.), 2014.

[127] G. Litjens, O. Debats, W. van de Ven, N. Karssemeijer, and H. Huisman, "A pattern recognition approach to zonal segmentation of the prostate on MRI," in *Medical Image Computing and Computer-Assisted Intervention - MICCAI 2012*, vol. 7511 of *Lecture Notes in Computer Science*, pp. 413–420, 2012.

[128] P. C. Vos, J. O. Barentsz, N. Karssemeijer, and H. J. Huisman, "Automatic computer-aided detection of prostate cancer based on multiparametric magnetic resonance image analysis," *Physics in Medicine and Biology*, vol. 56, pp. 1527–1542, March 2012.

[129] C.-P. Yu, G. Ruppert, R. Collins, D. Nguyen, A. Falcao, and Y. Liu, "3D blob based brain tumor detection and segmentation in MR images," in *IEEE Internation Symposium on Biomedical Imaging (ISBI)*, (Beijing, China), 2014.

[130] W. K. Moon, Y.-W. Shen, M. S. Bae, C.-S. Huang, J.-H. Chen, and R.-F. Chang, "Computer-aided tumor detection based on multi-scale blob detection algorithm on automated breast ultrasound images," in *IEEE Transactions on Medical Imaging*, vol. 32, pp. 1191–1200, July 2013.

[131] S. M. Han, H. J. Lee, and J. Y. Cho, "Computer-aided prostate cancer detection using texture features and clinical features in ultrasound image," *Journal of Digital Imaging*, vol. 21, no. 1, pp. 121–133, 2008.

[132] M. Noguchi, T. A. Stamey, J. E. McNeal, and C. M., "Relationship between systematic biopsies and histological features of 222 radical prostatectomy specimens: Lack of prediction of tumor significance for men with nonpalpable prostate cancer," *Journal of Urology*, vol. 166, no. 1, pp. 104–110, 2001.

[133] E. Ruijter, G. van Leenders, G. Miller, F. Debruyne, and C. van de Kaa, "Errors in histological grading by prostatic needle biopsy specimens: frequency and predisposing factors," *Journal of Pathology*, vol. 192, pp. 229–233, 2000.

[134] L. Wang, Y. Mazaheri, J. Zhang, N. M. Ishill, K. Kuroiwa, and H. Hricak, "Assessment of biologic aggressiveness of prostate cancer: Correlation of MR signal intensity with gleason grade after radical prostatectomy," *Radiology*, vol. 246, no. 1, pp. 168–176, 2008.

[135] A. Chu, C. Sehgal, and J. Greenleaf, "Use of gray value distribution of run lengths for texture analysis," *Pattern Recognition Letters*, vol. 11, no. 6, pp. 415–419, 1990.

[136] B. V. Dasarathy and E. B. Holder, "Image characterizations based on joint gray level-run length distributions," *Pattern Recognition Letters*, vol. 12, no. 8, pp. 497–502, 1991.